SOLAR ENERGY COLLECTION IN COMPLEX RADIATION FIELDS: IMPLICATIONS FOR LARGE AND INFRASTRUCTURE-CONSTRAINED PANEL ARRAYS

By

JENNIFER LYNN KAFKA

A dissertation submitted to the

School of Graduate Studies

Rutgers, The State University of New Jersey

In partial fulfillment of the requirements

For the degree of

Doctor of Philosophy

Graduate Program in Atmospheric Science

Written under the direction of

Mark A. Miller

And approved by

____

____

____

____

New Brunswick, New Jersey

January, 2020

ABSTRACT OF THE DISSERTATION

Solar Energy Collection in Complex Radiation Fields: Implications for Large and Infrastructure-Constrained Panel Arrays

By JENNIFER LYNN KAFKA

Dissertation Director:

Mark A. Miller

Solar energy as a viable renewable energy source has been gaining traction over the past decade, with solar energy claiming the title of fastest growing renewable energy for the past three consecutive years. The significant increase in new installed photovoltaic (PV) capacity can be attributed to plummeting costs of PV modules along with government tax incentive programs. Meanwhile, the cost of land, on which most solar arrays are constructed, has been rising. Thus, careful consideration must be taken when designing large solar panel arrays, both in terms of land use and panel-incident solar energy, so that the array is best tuned to the local radiation field and can harvest the highest amount of incoming solar radiation per unit area.

This dissertation first investigates the complex radiation field across the United States by evaluating data from the National Solar Radiation Database (NSRDB), which is a spatially dense modeled radiation dataset intended to accurately represent long-term statistics. The spatial and temporal characteristics of the direct-beam and diffuse radiation

fields across the United States (US) were analyzed. A high proportion of diffuse radiation across the Eastern US and Pacific Northwest underlined the importance of harvesting procedures being better tuned to account for the diffuse field and partly cloudy climates.

Next, an alternative approach of organizing large solar panel arrays is suggested which considers the co-optimization problem of maximizing per-panel incident energy and minimizing the amount of land required. This approach introduces a new dual-angle technique, called the dual-angle solar harvest (DASH) method, in which a solar array is composed of two tilt angles. Results from the DASH method are explored nationwide and for two climatically different locations of Akron, OH and Barstow, CA. For a 10% gain in array-wide plane-of-array incident solar energy when keeping one angle constrained at the single optimum tilt angle, only 35% of panel rows would need to be adjusted in Akron, compared to 70% of rows in Barstow. Thus, it is shown that the DASH method performs best in cloudier locations, such as the Pacific Northwest and the Great Lakes region.

Finally, observed inverter-level energy output data from two solar carport canopies with the same tilt but different azimuth angles on Livingston Campus at Rutgers University are evaluated. The differences in time-of-day energy output are investigated with respect to cloud cover and diurnal variations in the diffuse field, as New Jersey is a partly cloudy climate with a high proportion of diffuse radiation. The inverter-level energy output from the solar canopies are compared to observed solar irradiance data from a nearby meteorological and radiation station (the Rutgers' Photochemical Assessment Monitoring [PAM] Site) and longer range standardized historical data provided by NREL (TMY3). A sky cover algorithm is also developed to classify days as clear, variable, or cloudy to show that increased cloudiness in the afternoon observed on clear and variable days contributes to differences in the rate of energy output in the morning hours versus afternoon hours between the two solar carport canopies.

ACKNOWLEDGEMENTS

The completion of this work would not have been possible without the help and guidance of my advisor, Dr. Mark Miller. Thank you for seeing my potential as a scientist at the end of my undergraduate studies and thank you for pushing me to apply for and eventually come to the end of my doctorate degree. I don't think I ever would have pursued a Ph.D. had it not been at your recommendation.

I would also like to thank my committee members. Dr. Dunbar Birnie has been a great resource this past summer and his previous work related to solar energy has been instrumental in the completion of this dissertation. Thank you to Dr. Benjamin Lintner and Dr. Steven Decker, two dedicated professors in the Atmospheric Science department who I've had the pleasure to get to know both in my undergraduate and graduate studies. Without their teaching, I would not be the scientist I am today.

A huge thank you to all my friends within the department. Thank you to my "atmos-sister", Dr. Arielle Catalano, who has been there since day 1 of my PhD and whose friendship and support in the form of craft nights and hiking were much needed. I wouldn't have survived Quals without her and the many late nights we spent studying together. Thank you also to Dr. Bryan Raney, Max Pike, and Matt Drews. Their friendship and lunches spent together helped to keep me sane.

My husband and family have been a constant source of encouragement throughout this process. Thank you for being patient during the stressful times and thank you for always being there for me.

Financial support for this research came from the Institute of Earth, Ocean, and Atmospheric Sciences (EOAS) at Rutgers University and the Rutgers Energy Institute (REI). Chapter 2 of this work has already been published in the Renewable Energy journal in December 2018, entitled *A Climatology of Solar Irradiance and its Controls across the United States: Implications for Solar Panel Orientation.*

CONTENTS

Abstract ii

Acknowledgements...v

List of Tables...xi

List of Illustrations xii

Chapter 1: Introduction..1

1.1 Motivation..1

1.1.1 The Growth of Photovoltaics...1

1.1.2 Optimizing Energy Incident on a Photovoltaic Module..................3

1.1.3 Accounting for Land Use with Large Photovoltaic Arrays.............7

1.1.4 Current Photovoltaic Array Techniques...and Beyond..................10

1.2 Scientific Objectives..13

1.3 Overview of Data and Methodology...13

1.3.1 Data Overview..13

1.3.2 Methodology Overview...15

Chapter 2: A Climatology of Solar Irradiance and its Controls across the United States: Implications for Solar Panel Orientation...18

2.1 Introduction...18

2.2 Materials and Methods 21

2.3 Results and Discussion 26

2.3.1 Continental Scale Radiation 26

2.3.1.1 Direct Beam Radiation...26

2.3.1.2 Diffuse Radiation....30

2.3.1.3 Diffuse-to-direct Radiation....30

2.3.2 Regional Scale Radiation....31

2.3.2.1 Meteorological Modulators of Regional Radiation....32

2.3.2.2 Regional Scale Direct and Diffuse Radiation....34

2.3.2.3 Regional Scale Diffuse-to-direct Radiation....34

2.4 Conclusions....35

Chapter 3: The Dual-Angle Solar Harvest (DASH) Method: An Alternative Method for Organizing Large Solar Panel Arrays that Optimizes Incident Solar Energy in Conjunction with Land Use 39

3.1 Introduction....39

3.2 Materials and Methods 41

3.2.1 Data 41

3.2.2 Method 43

3.2.2.1 Plane-of-Array Radiation....44

3.2.2.2 Array-Total Radiation....49

3.2.2.3 Applying the DASH Method....53

3.3 Results and Discussion 56

3.3.1 Testing the DASH Model at Two Ideal Locations 56

3.3.2 Applying the DASH Method on a National Scale 58

3.4 Conclusions 61

Chapter 4: Rutgers' Solar Array Performance Analysis in Relation to Tilt and Azimuth as Influenced by Local Diffuse/Direct Insolation Balance 64

4.1 Introduction....64

4.2 Data 65

4.2.1 Solar Carport Canopies....66

4.2.2 Rutgers' PAM Site....67

4.2.3 US DOE/NREL Typical Meteorological Year....68

4.3 Methods....69

4.3.1 Sky Cloud Cover Assessment Based on PAM Site Data....70

4.3.1.1 15-Minute Sky Cover Algorithm....70

4.3.1.2 Daily Sky Cover Algorithm....75

4.3.2. Sky Cloud Cover Assessment Based on TMY3 Data....76

4.4 Results and Discussion....77

4.4.1 PAM Site Insolation Data....78

4.4.2 Solar Canopy Electrical Output Data....79

4.4.3 TMY3 Reference Insolation Data....80

4.4.4 Comparing Lot 105 to the Yellow Lot....81

4.4.5 The Diffuse Field as Related to the Local Cloud Field....83

4.4.6 Solar Collection in the Morning versus Afternoon – Additional Effects....86

4.5 Conclusions....87

Chapter 5: Conclusion and Future Directions....90

5.1 Conclusion....90

5.1 Conclusions from Chapter 2....90

5.2 Conclusions from Chapter 3....91

5.3 Conclusions from Chapter 4....93

5.2 Future Directions....94

Tables....96

Illustrations....97

References....148

Chapter 1....148

Chapter 2....151

Chapter 3....153

Chapter 4....157

Chapter 5....159

LIST OF TABLES

Table 2.1. Regional Distribution of Stations 96

This table displays the number of Class I and Class II stations at each of the eight sub-divided regions for this study.

Table 3.1. Test Station Details 96

Specific details for the two test stations of Barstow, CA and Akron, OH regarding the number of panels necessary to observe specific energy gains using the DASH method with a 30/60 tilt angle split between β_1 *and* β_2, as well as each station's latitude, longitude, elevation, and optimum tilt angle.

LIST OF ILLUSTRATIONS

Figure 2.1. NSRDB Station Locations 97

The locations and divisions of all 1,454 NSRDB stations. Class I stations (242; green circles) contain a complete period of record with the highest quality solar modeled data, Class II stations (618; blue triangles) contain a complete period of record but have some windows of quality interpolated period, and Class III stations (594; orange squares) have gaps in their period of record but all have at least three years of data. There are also 40 total sites with measured data (white circle with inlaid triangle), but none have a complete period of record. From the NSRDB 1991-2010 User's Manual [19].

Figure 2.2. 1991-2005 Average Direct Radiation 98

The average direct radiation (Wh/m2) for each season: December-January-February (a), March-April-May (b), June-July-August (c), and September-October-November (d). The dots represent the locations of the individual Class I and Class II stations from the NSRDB, which were used to interpolate the data across the entire continental US.

Figure 2.3. Average Direct Radiation versus Latitude 99

Direct radiation at each station plotted against latitude for December-January-February (a), March-April-May (b), June-July-August (c), and September-October-November (d). Each point is semi-transparent; thus, the more opaque the scatter points, the larger the concentration of direction radiation values at that particular latitude. The best fit line is plotted over the data, and the associated R^2 value is labeled in each panel.

Figure 2.4. Average Direct Radiation versus Longitude 100

Direct radiation at each station plotted against longitude for each season. December-January-February (a), March-April-May (b), June-July-August (c), and September-October-November (d). This is plotted the same way as Figure 1.3.

Figure 2.5. Elevation at Each Station 101

The elevation and geographical location of each Class I and Class II station. Both the size and color depict the elevation.

Figure 2.6. 1991-2005 Average Aerosol Optical Depth 102

The average aerosol optical depth for each season: December-January-February (a), March-April-May (b), June-July-August (c), and September-October-November (d). Plotted the same way as in Figure 1.2.

Figure 2.7. 1991-2005 Average Total Sky Cover..103

The average total sky cover (in tenths) for each season: December-January-February (a), March-April-May (b), June-July-August (c), and September-October-November (d). Plotted the same way as in Figure 1.2.

Figure 2.8. 1991-2005 Average Diffuse Radiation 104

The average interpolated diffuse radiation (Wh/m^2) for each season: December-January-February (a), March-April-May (b), June-July-August (c), and September-October-November (d). Plotted the same way as in Figure 1.2.

Figure 2.9. Average Diffuse Radiation versus Latitude..105

Diffuse radiation at each station plotted against latitude for December-January-February (a), March-April-May (b), June-July-August (c), and September-October-November (d). Plotted the same way as in Figure 1.3.

Figure 2.10. Average Diffuse Radiation versus Longitude 106

Diffuse radiation at each station plotted against longitude for December-January-February (a), March-April-May (b), June-July-August (c), and September-October-November (d). Plotted the same way as in Figure 1.3.

Figure 2.11. 1991-2005 Average Ratio of Diffuse to Direct Radiation 107

The average interpolated ratio of diffuse radiation to direct radiation for each season: December-January-February (a), March-April-May (b), June-July-August (c), and September-October-November (d). Plotted the same was as in Figure 1.2.

Figure 2.12. Avg Ratio of Diffuse to Direct Radiation versus Longitude 108

Ratio of diffuse to direct radiation at each station plotted against longitude for December-January-February (a), March-April-May (b), June-July-August (c), and September-October-November (d). This is plotted the same way as Figure 1.3.

Figure 2.13. Location of Regional Stations...109

The location of each Class I and Class II station, colored according to which region it was sub-divided into for this study.

Figure 2.14. 1991-2005 Mean Total & Opaque Sky Cover for Each Region 110

The average 15-year mean monthly and 15-year envelope of minimum to maximum values total sky cover (blue line) and opaque sky cover (green dashed line) in the Northwest (a), Plains (b), Midwest (c), Northeast (d), Southwest (e), Desert-Southwest (f), South-Central (g), and Southeast (h). These are plotted against the left vertical axis. The difference between total and opaque sky cover is represented by the purple line with circles and is plotted against the right vertical axis.

Figure 2.15. Total – Opaque Sky Cover 111

The annual cycle of total-opaque sky cover, which is a proxy for optically thin clouds, for each of the eight regions according to the key on the upper right.

Figure 2.16. 1991-2005 Mean Aerosol Optical Depth for Each Region 112

The average 15-year mean monthly (black line) and 15-year envelope of minimum to maximum values (grey shading) of aerosol optical depth in the Northwest (a), Plains (b), Midwest (c), Northeast (d), Southwest (e), Desert-Southwest (f), South-Central (g), and Southeast (h).

Figure 2.17. 1991-2005 Mean Direct & Diffuse Radiation for Each Region 113

The average 15-year mean monthly direct (blue line) and diffuse (red line) radiation in the Northwest (a), Plains (b), Midwest (c), Northeast (d), Southwest (e), Desert-Southwest (f), South-Central (g), and Southeast (h).

Figure 2.18. Ratio of Diffuse to Direct Radiation for Each Region 114

The annual cycle of the ratio of diffuse to direct radiation for each of the eight regions, according to the key in the upper right. A value closer to one indicates that the diffuse radiation is near to or equal to the direct radiation, while a value closer to zero indicates a large gap between the direct radiation and the diffuse radiation.

Figure 2.19. 1991-2005 Mean Diffuse Radiation for Each Region 115

The annual cycle of average mean diffuse radiation for each of the eight regions, according to the key in the upper right.

Figure 3.1. NSRDB Station Locations 116

The locations and divisions of all 1454 NSRDB stations. Class I stations (242; green circles) contain a complete period of record with the highest quality solar modeled data, Class II stations (618; blue triangles) contain a complete period of record but have some windows of quality interpolated period, and Class III stations (594; orange squares) have gaps in their period of record but all have at least three years of data. There are also 40 total sites with measured data (white circle with inlaid triangle), but none have a complete period of record. From the NSRDB 1991–2010 User's Manual.

Figure 3.2. Geometry of the Sun with respect to a Solar Panel.....................................117

The various angles associated with a solar panel with tilt, β. The solar panel is in in Northern Hemisphere as the panel is facing south. α is the solar elevation angle of the sun with respect to the horizon, θ_Z is the solar zenith angle, and θ_i is the angle of incidence, which is the angle between the direct normal beam and the surface normal with respect to the solar panel.

Figure 3.3. Single Optimized Tilt Angle...118

Each dot represents the calculated optimum tilt angle for each Class I and Class II station in the NSRDB, while the color fills are interpolated from the station data. Tilt angles are color-contoured every 2.5 degrees. The test locations of Barstow, CA and Akron, OH are marked by the red circles.

Figure 3.4. 1991-2005 Year Averaged Cloud Cover...119

The annual averaged cloud cover in tenths, adapted from Kafka and Miller 2018 [34]. Plotted the same way as figure 3.3.

Figure 3.5. Diagram Showing Solar Array Inter-Row Effects 120

Panel (a) illustrates the lengths and angles associated with inter-row shadowing effects when a shadow from a solar panel with tilt, β, is long enough to be projected onto the solar panel behind. Panel (b) illustrates the concept of inter-row masking of the diffuse field. The first row of the solar array has an uninterrupted view of the diffuse field in front of it, while part of the diffuse field as seen from the second row is masked from the row in front. $Panel_L$ is the length of the solar panel and $Panel_{sp}$ is the row spacing from figure 3.6.

Figure 3.6. Geometry of Solar Panel Shadowing...121

The various angles associated with the shadow cast behind a solar panel with tilt, β, when the sun is at a solar elevation angle α. $Panel_L$ is the length of the solar panel, $Panel_g$ is the projection of the solar panel along the ground, $Panel_h$ is the height from the ground to the top of the tilted solar panel, $Panel_{sh}$ is the ground length of the shadow cast behind the solar panel, and $Panel_{sp}$ is the sum of $Panel_g$ and $Panel_{sh}$, or the panel spacing length.

Figure 3.7. Theoretical Footprint of a 100-Row Solar Panel Array using the Optimum Tilt Angle..122

The length of ground space in meters needed to house a 100-row solar panel array where all panels are tilted at the single optimum tilt angle, as shown in figure 3.3. The spacing between rows was determined by the shadow length behind a tilted solar panel at 10:00 AM local time on December 21, the winter solstice. Plotted the same way as figure 3.3.

Figure 3.8. Diagram Showing Single Angle Array Versus Dual Angle Array..............123

An idealized cartoon showing the number of rows that would fit in a standard single angle array (a) versus the number of rows that would fit by adapting a dual angle system. In this case, more rows of panels tilted at a lower angle could fit in the same space compared to panels tilted at the original angle as the shadow length behind the lower panel is much shorter. Drawing is not to scale but is designed to visualize a dual angle array. The solar panels are represented by the blue rectangles and the resulted shadow is depicted by the light gray triangles, assuming the light source is located to the left.

Figure 3.9. Percent Gain or Loss of F_{TOT} for Every Dual Angle Combination for Barstow, CA 124

The resultant percent gain/loss in array-wide incident solar energy ($F_{TOT,array}$) using every possible combination of β_1 and β_2 for Barstow, CA, when using (a) a 30/70 split between β_1 and β_2 and (b) a 50/50 split between β_1 and β_2. The white diagonal band indicates combinations of angles that are less than or equal to a 5° difference (where DASH isn't calculated). Gains in $F_{TOT,array}$ are shown in shades of red, while losses of $F_{TOT,array}$ are shown in shades of blue. Selected gains of 5, 10, and 20% are shown with the red lines, while the optimum tilt angle is highlighted with the set of dashed black lines.

Figure 3.10. Number of Extra Rows for Every Dual Angle Combination That Fit into the Footprint of a 100-Row Single Angle Solar Array in Barstow, CA 125

The number of extra solar panel rows that can fit into the footprint of a 100 row solar array using the single optimum tilt angle for Barstow, CA, when using (a) a 30/70 split between β_1 and β_2 and (b) a 50/50 split between β_1 and β_2. The white diagonal band indicates combinations of angles that are less than or equal to a 5° difference (where DASH is not calculated). The same selected gains (solid red lines) shown in figure 3.9 are also shown here, while the optimum tilt angle is highlighted with the set of dashed black lines.

Figure 3.11. Percent Gain or Loss of F_{TOT} for Every Dual Angle Combination for Akron, OH.........126

The resultant percent gain or loss in harvested solar energy ($F_{TOT,array}$) using every possible combination of β_1 and β_2 for Akron, OH, when using (a) a 30/70 split between β_1 and β_2 and (b) a 50/50 split between β_1 and β_2. Plotted as in Figure 3.9, but the 50% gain contour is also shown (in yellow).

Figure 3.12. Number of Extra Rows for Every Dual Angle Combination That Fit into the Footprint of a 100-Row Single Angle Solar Array in Akron, OH.........127

The number of extra solar panel rows that can fit into the footprint of a 100 row solar array using the single optimum tilt angle for Akron, OH, when using (a) a 30/70 split between β_1 and β_2 and (b) a 50/50 split between β_1 and β_2. Plotted as in Figure 3.10.

Figure 3.13. Number of Extra Panel Rows by Tilting All Panels 5° Lower than β_{opt}...128

Colors indicate the number of extra panels (exceeding 100) that can fit into the same footprint of a 100-row β_{opt} array when all panel tilts are lowed by 5°.

Figure 3.14. Number of Extra Panel Rows by Tilting All Panels 5° Lower than β_{opt}

Figure 3.14. Dash Method: Percent of Panel Rows Changed to β_2 for a 10%/20% Gain in Energy..129

Colors indicate the percent of panel rows that needed to be adjusted to β_2 to see (a) a 10% increase and (b) a 20% increase in array-wide incident solar energy and using the fewest possible extra panel rows across the same footprint of a 100-row β_{opt} array.

Figure 3.15. DASH Method: β_2 Angle for a 10%/20% Gain in Energy........................130

Colors indicate the tilt angle, β_2, necessary to see (a) a 10% increase and (b) a 20% increase in array-wide incident solar energy using the fewest possible extra panel rows across the same footprint of a 100-row β_{opt} array.

Figure 3.16. 1991–2005 Average Ratio of Diffuse to Direct Radiation........................131

The average interpolated ratio of diffuse radiation to direct radiation for each season: December-January-February (a), March-April-May (b), June-July-August (c), and September-October-November (d). Plotted as in Figure 3.3; adapted from Kafka and Miller 2018 [3.33].

Figure 4.1. Geometry of the Rutgers Solar Carport Canopy...132

Photograph showing a side-view of one of the rows of the Livingston Campus Solar Carport Canopy. The photograph has been annotated to show the tilt angle (15°), from horizontal, of one side of the canopy. The other side of the canopy is flat.

Figure 4.2. Aerial Map of Livingston Solar Carport Canopies......................................133

Aerial diagram, taken from Google Maps, showing the relative locations of the two different solar carport canopies on Livingston Campus at Rutgers University: The Yellow Lot (upper left) and Lot 105 (lower middle). The photograph has been annotated to point out the azimuth angle of each of the canopies: the Yellow Lot is aimed at 126°, or generally ESE and Lot 105 is aimed at 216°, or generally SSW. As a reference, an azimuth angle of 180° would indicate a due southward orientation. A third Rutgers solar array is visible in the lower right corner.

Figure 4.3. PAM Site Radiation Data of a Clear, Variable, and Cloudy Day................134

Ideal examples of a clear day, variable day, and cloudy day. A screenshot showing sky conditions mid-day from the BloomSky instrument at the PAM Site are shown in the top row, the observed and monthly mean profiles of 15-minute GHI and DHI are shown in the middle row and the observed and monthly mean profiles of 15-minute GHI and DHI variance are shown in the bottom row GHI is plotted in green, DHI is plotted in blue, observed profiles are plotted with solid lines, and monthly mean profiles are plotted with dashed lines. Please note the difference in scale between panel (h) compared to panels (g) and (i).

Figure 4.4. Sky Cover Algorithm Output for a Clear, Variable, and Cloudy Day.........135

For each ideal example of a clear, variable, and cloudy day in Figure 4.3, the 15-minute output from the sky cover algorithm described in section 4.3.1 is plotted (top row), while the middle row displays the percent of 15-minute observations that were classified in each sky cover bin each month and the bottom row displays the percent of 15-minute observations that were classified in each sky cover bin per hour of the day.

Figure 4.5. Daily Integrated GHI at the PAM Site binned into Dominant Sky Cover...136

Daily integrated totals of GHI constructed from observations at the PAM Site during the entire period of record in section 4.2.2. Each daily sum is reported in units of $Wh/m^2/day$ and is binned according to the daily dominant sky cover algorithm described in section 4.3.1. Variable days are represented by blue dots, cloudy days are represented by orange dots, and clear days are represented by green dots.

Figure 4.6. Daily Integrated DHI at the PAM Site binned into Dominant Sky Cover...137

Daily integrated totals of DHI constructed from observations at the PAM Site during the entire period of record in section 4.2.2. Each daily sum is reported in units of $Wh/m^2/day$ and is binned according to the daily dominant sky cover algorithm described in section 4.3.1. Plotted the same way as figure 4.5.

Figure 4.7. Daily Integrated Inverter Averaged Solar Canopy Data binned into Dominant Sky Cover..138

Daily integrated totals showing the average output from a single inverter across both solar canopies during the entire period of record in section 4.2.1. Each daily sum, in units of kWh/day, is calculated using the 15-minute output across a single inverter and is binned according to the daily dominant sky cover algorithm described in section 4.3.1. The total canopy output can be extrapolated by multiplying by the number total inverters (14). Plotted the same way as figure 4.5.

Figure 4.8. Daily Integrated TMY Solar Data from PVWATTS binned into Dominant Sky Cover..139

Daily integrated totals of GHI using typical meteorological year (TMY) data output from PVWATTS. Each daily sum is reported in units of $Wh/m^2/day$ and is binned according to the daily dominant sky cover algorithm. Plotted the same way as figure 4.5.

Figure 4.9. Normalized Daily Solar Canopy Output on Clear Days..............................140

A subset of the solar canopy inverter data on clear days was created by using the dominant cloud cover algorithm described in section 4.3.1 and was then separated by Lot 105 and The Yellow Lot. Hourly values for each parking lot were summed and the peak of the total was normalized to 1. The slope of each profile between 7:00 AM and 10:00 AM and also between 2:00 PM and 5:00 PM are also displayed.

Figure 4.10. Normalized Daily Solar Canopy Output on Variable Days.......................141

Plotted the same way as figure 4.9 but showing output for variable days.

Figure 4.11. Normalized Daily Solar Canopy Output on Cloudy Days.........................142

Plotted the same way as figure 4.9 but showing output for Cloudy days.

Figure 4.12. Hourly Irradiance Input Projected for the Yellow Lot and Lot 105 for Clear Days..143

Annual hourly averaged irradiance combining flat and tilted sections of the Yellow Lot and Lot 105 based on TMY3 hourly data for DNI and DHI.

Figure 4.13. Hourly Irradiance Input Projected for the Yellow Lot and Lot 105 for Variable Days 144

Annual hourly averaged irradiance combining flat and tilted sections of the Yellow Lot and Lot 105 based on TMY3 hourly data for DNI and DHI.

Figure 4.14. Hourly Irradiance Input Projected for the Yellow Lot and Lot 105 for Cloudy Days 145

Annual hourly averaged irradiance combining flat and tilted sections of the Yellow Lot and Lot 105 based on TMY3 hourly data for DNI and DHI.

Figure 4.15. Hourly Diffuse Radiation Ratio for Cloudy, Clear, and Variable Days.....146

Hourly averaged ratios of DHI to GHI from the PAM Site observational data was binned into cloudy, clear, and variable days according to the sky cover algorithm described in section 4.3.1. The average was taken across the entire dataset for each hour. Cloudy data is shown in orange, variable data is shown in blue, and clear data is shown in green.

Figure 4.16. The Average Diffuse Radiation Ratio Before and After Noon for Cloudy, Clear, and Variable Days...147

Hourly averaged ratios of DHI to GHI from the PAM Site observational data was binned into cloudy, clear, and variable days according to the sky cover algorithm described in section 4.3.1. The average from sunrise to 12:00 noon is shown by the green bars, while the average from 12:00 noon to sunset is shown by the purple bars. These bars represent the average component of diffuse radiation during the first half of the day and the second half of the day for each of the three sky condition bins.

Chapter 1:

Introduction

1.1 MOTIVATION

1.1.1. The Growth of Photovoltaics

The deployment and use of solar panels as a renewable energy source have seen rapid global growth [1.1]. For the past three consecutive years, solar energy has been the fastest growing renewable energy source in the world [1.2], outpacing other renewable sources such as wind, hydropower, and bioenergy. In the U.S. alone, the Solar Energy Industries Association (SEIA) has recently reported that the U.S. solar market is booming [1.3]. During the first quarter (Q1) of 2019, the U.S. installed 2.7 gigawatts (GW) of new solar photovoltaic (PV) capacity, marking the largest Q1 addition on record. These new installations also resulted in the U.S. solar market surpassing 2 million total installations, a huge milestone that occurred only 3 years after the U.S. reached the 1 million installation milestone in 2016. Additionally, more than half (51%) of all new U.S. electricity generating capacity additions during 2019 Q1 came from solar power [1.4]. An additional 2.1 GW of new solar PV capacity was installed during the second quarter (Q2) of 2019, bringing total U.S. PV installed capacity to 69.1 GW [1.5]. Further, it is expected that the total amount of installed PV capacity across the U.S. will more than double in the next five years [1.5].

This "booming" growth in the U.S. solar market [1.3] can be attributed to a combination of declining costs involved with PV modules and installation as well as government tax incentive programs and policies. Compared to other energy technologies, photovoltaics, or solar energy, has displayed the most rapid cost decline [1.6]. From 2010 to 2018, the average cost per watt of installed residential PV (adjusted for inflation) has dropped by 63%, from $7.34 to $2.70 per watt, while the average cost per watt of installed Utility-scale PV (at a fixed tilt) has dropped by 77%, from $4.63 to $1.06 per watt [1.7].

Kavlak et al. 2018 [1.8] studied the low-level and high-level mechanisms that contributed to the plummeting costs of PV modules over the past 40 years. Low-level mechanisms of cost reduction are the measurable and technology-specific determinants of price, while high-level mechanisms describe the processes that can control and dictate the low-level mechanisms of cost reduction. Between 1980 and 2012, it was found that the three primary low-level mechanisms that contributed to the cost reduction of PV modules were increased PV cell efficiency (23%), the declining cost of silicon (21%), and the declining cost of non-silicon materials (16%). Meanwhile, the two primary high-level cost reducing mechanisms were public and privately funded research and development (nearly 60%) and growing economies of scale (nearly 25%) [1.8].

While the declining costs of PV modules certainly played a large role in the overall growth and potential of the solar energy market, it wasn't until government incentives and policies came online that rapid growth truly began. In the past decade alone, solar has seen an average growth rate of 50%, thanks in large part to the Solar Investment Tax Credit (ITC) [1.2, 1.9, 1.10].

The Solar ITC was first introduced by the Energy Policy Act of 2005 [1.2] with the goal of supporting the U.S. market through the transition to renewable energy by offering a one-time 30% tax deduction on all newly installed solar PV modules, both in the residential and commercial sectors. Due to its popularity and the remarkable growth in the solar market that the Solar ITC stimulated, it has been extended multiple times. Currently, the 30% Solar ITC will end in 2019, before stepping down to 26% in 2020, 22% in 2021, and 10% in 2022 [1.10].

Performance-based incentives (PBIs) are another way to motivate companies and people to install PV modules. Rather than a one-time tax incentive (like with the Solar ITC), PBIs offer weekly, monthly, or annual incentives based on the amount of energy generated from a solar PV system [1.11]. Many states and utility companies offer local PBIs to entice the growth of solar energy in their domain, and the rate of incentive is determined upon installment of the PV system.

1.1.2. Optimizing Energy Incident on a Photovoltaic Module

While the cost of PV modules has been getting significantly cheaper with time, an individual solar panel is only as good as the amount of energy it can harvest, which is dependent on several key items: (1) the efficiency of the photo voltaic (PV) cells themselves, or in other words, how efficient the individual cells on a solar panel are at converting photons to electricity, (2) the amount of insolation that is available at a given location, and (3) the angle and direction at which the solar panel is oriented, or how much of the solar irradiance field is incident on the panel. A brief expansion of these three factors are discussed below.

(1) Solar Panel Efficiencies

As previously mentioned, a significant portion of declining costs of solar panel modules can be attributed to rising solar panel efficiencies through the years [1.8]. While efficiencies of earlier versions of PV cells quickly doubled, jumping from 4% efficiency in 1954 to 10% efficiency in 1959, in a span of just 5 years [1.12], subsequent jumps in technology have taken much longer. The first PV cell to break the 20% efficiency barrier didn't occur until 25 years later, in 1985 [1.12]. While further gains in efficiency have taken place in the 35 years since (with some research PV cells reaching 46% efficiency! [1.13]), commercially produced and installed solar panels generally still only see actual efficiencies between 18-22% [1.14]. In other words, the rate of commercially produced solar PV cell efficiency gain has dropped off rapidly.

(2) Available Solar Irradiance

The primary determinant of surface solar irradiance is the seasonal cycle. Higher values of surface irradiance are observed in the summer when the days are longer and the surface of the earth is tilted towards the sun and lower values are observed in the winter, when the days are shorter and the surface of the earth is tilted further away from the sun [1.18] The total available solar irradiance is also a function of the diurnal cycle, which changes throughout the course of the year. Characteristics of the local geography and climate are also important. For example, the local cloud field plays a key role in determining the total irradiance that strikes the ground. Cloudier locations receive less direct beam irradiance and typically have lower values of ground reaching irradiance, while sunnier locations receive more beam irradiance and typically have higher values of ground reaching irradiance.

As noted, the amount of solar radiation that is available to be harvested at a given location is dependent on several factors including the location's latitude, geographic characteristics, diurnal cycle, and climate [1.15]. In addition to modulating the received power density of solar radiation, latitude dictates the average path length of the direct beam of radiation from the sun between the top of the atmosphere and the Earth's surface. Sunlight must pass through a thicker cross section of atmosphere at higher latitudes than at latitudes closer to the equator; thus, more radiation may be absorbed or scattered along this extended path, thereby decreasing the total available solar irradiance at the surface. Elevation has a similar effect as latitude, with higher elevations behaving similarly to lower latitudes as there is less atmosphere for the direct beam of radiation to pass through [1.16, 1.17]. A location's proximity to mountains and other terrain also affects the total available ground reaching solar irradiance, as these large features can block direct light hours before the sun is actually below the horizon [1.16].

Obviously, a location with greater surface irradiance has the potential to harvest more solar energy than a location with lower values of ground reaching irradiance. While the climate is changing, as has been reported in each subsequent IPCC report [1.19], the year-to-year change in solar radiation is generally small and the changing insolation at a given location doesn't largely influence the amount of energy harvested from a solar panel.

(3) Solar Panel Tilt and Orientation

Perhaps the easiest way to increase the amount of energy harvested by a solar panel is to optimize a solar panel's orientation and tilt. The amount of energy that a solar panel harvests is directly related to the amount of incoming solar radiation that strikes the panel's surface [1.20]. The solar radiation field at the surface, or total global horizontal irradiance (GHI) can be broken into two components: the direct normal irradiance (DNI), or direct beam, and the diffuse horizontal irradiance (DHI), or diffuse field [1.21, 1.22]. The direct beam of solar radiation is the beam directly from the sun to the earth's surface and contains the highest concentration of energy. The diffuse field is the solar radiation that comes from all directions, and is the result of scattering, reflection, and refraction. During sunny conditions, the total GHI is composed primarily of the direct normal beam; however, when clouds cover the solar disc, the solar radiation field at the surface transitions to one that is primarily composed of the diffuse field [1.23, 1.24, 1.25].

Under ideal sunny conditions, the highest amount of harvested energy results when the direct beam of insolation is orthogonal to the panel's surface. In the Northern Hemisphere, this means facing the panel south and at a tilt angle 90 degrees from the direct beam of insolation [1.26].

As the sun is constantly changing positions in the sky relative to the surface, the best way to obtain this ideal scenario is with a dual-axis tracker system, which follows the sun's path in the sky both longitudinally and azimuthally [1.27, 1.28, 1.29, 1.30]. However, as these tracker systems require energy to operate, they are expensive to maintain [1.31]. The cheapest solar panel to operate is a fixed angle solar panel, or one that maintains the same angle at all times and is not on a motorized mount [1.32]. However, a fixed angle solar panel is not always orthogonal to the direct beam of radiation. Rather, a single optimized angle must be found that ensures the highest harvested energy possible. As the sun's energy is strongest when it is highest in the sky (less of the beam is lost due to refraction or scattering because of the atmosphere as the beam travels through a shorter path length of atmosphere when the sun is directly overhead compared to when it is lower in the horizon), a good starting point for finding an optimized tilt angle is to consider the angle of the sun at solar noon.

By considering the solar noon angle, a lot of emphasis is placed on the direct normal beam, with little attention to the diffuse radiation field. In higher latitudes, the solar noon sun angle is lower in the sky, which means that a solar panel much be tilted higher to be orthogonal to the direct beam. In contrast, the best way to harvest the diffuse field of radiation is with a flat panel. This is because the diffuse field can often be approximated as being isotropic with incoming radiation from all directions being equal. The higher the tilt angle of the solar panel, the larger the component of the diffuse field that is lost behind the tilted solar panel. Thus, more of the diffuse field is lost with current harvesting techniques at higher latitudes, such as across the mid-latitudes, as the optimum tilt angle is higher than at a location near the equator.

1.1.3. Accounting for Land Use with Large Photovoltaic Arrays

PV installations rarely include a single solar panel. Rather, multiple solar panels are often combined to create one PV array, connected by one or several power inverters. Common locations for solar panel arrays can be on a roof of a building or across an open field or parcel of land. Residential arrays, such as those commonly seen on sloped roofs, can be made up of a few dozen panels. Meanwhile, commercial and utility scale arrays can easily be comprised of hundreds of thousands or even millions of panels [1.33]. For example, the 290 MW Agua Caliente array in Yuma County, Arizona, completed in April 2014, is comprised of 4.9 million solar panels [1.34].

More than half of all PV capacity installed between 2010 and 2018 can be attributed to these large solar panel arrays (non-residential and utility-scale) [1.3]. One drawback or challenge of these large PV arrays is the amount of physical space they must occupy. While many smaller, residential arrays are located on roofs, which don't take up any extra space (i.e. the roof was already there and no extra ground surface was used), most large commercial and utility arrays are positioned on what otherwise was an empty parcel of land.

There are two primary costs to this land use: the actual cost, in dollars, of the land being used and the environmental and ecological costs that come with altering a previously unoccupied or undeveloped landscape. Compared to traditional power plants, the environmental impacts from a large PV array are much less; however, the impacts are not zero. Solar emits far fewer hazardous chemicals into the environment and produces roughly 25 times less greenhouse gas emissions compared to traditional power generation from coal, natural gas, and nuclear power plants [1.35]. From an ecological perspective, large solar arrays can be detrimental to bird populations as more transmission lines are needed compared to traditional power plants. Meanwhile, more research and observational studies are required to accurately diagnose the magnitude to which the natural plant and animal wildlife and habitats can be affected compared to traditional power plants [1.35]. Regardless, these impacts to the natural plant and animal wildlife are not null as the land surface is transformed from its natural state to housing rows upon rows of solar panels, power stations, and inverters [1.30].

The solar harvest per unit area of land is impacted by the "shadowing effect" in which one solar panel casts a shadow upon another. A study performed by the National

Renewable Energy Laboratory (NREL) diagnosed the amount of land required for different sizes and types of PV systems, such as fixed PV mounts, single axis trackers, and dual axis trackers. For large PV systems (greater than 20 MWs of capacity), it was found that arrays comprised of fixed PV mounts required the least amount of land per installed MW. On average, 5.8 acres were required per installed MW of capacity for a fixed mount system compared to 9.0 acres for a single-axis system and 6.1 acres for a dual-axis system [1.36]. While the fixed mount PV arrays take up less space than their moving counterparts, the single- and dual-axis tracker systems shine when it comes to harvested solar energy, or the amount of generated GWh/yr. The same study found that a dual-axis tracker system required only 2.0 acres per generated GW, while a fixed mount system required 2.8 acres and a single-axis tracker system required 3.5 acres [1.36].

A major consideration for future installations of large solar panel arrays must not only be the cost of the solar panels themselves, but also the cost of land. While fluctuations in price do exist, the price of land is generally increasing with time [1.37, 1.38]. Taking the 290 MW Agua Caliente solar array in Arizona as an example, it is easy to see that a very large parcel of land was required. One solution with lower costs as well as lower environmental impacts for mid-sized arrays has been to use closed landfills [1.30]. Closed landfills are characterized by degraded land and are certainly cheaper than a clean, open field; however, closed landfills are neither infinite in number nor are they always conducive for the installation of large solar panel arrays. The ground might be too unstable, there may not be enough space, or the orientation of the site may not be optimal for solar energy harvesting. A project like the Agua Caliente solar array is too large for this solution.

1.1.4. Current Photovoltaic Array Techniques...and Beyond

In 2018, 69% of the United States' solar energy generation (or roughly 67 MWh) came from utility-scale PV arrays [1.39]. The U.S. Energy Information Administration (EIA) reported that nearly 40% of all utility-scale PV systems at the end of 2017 were fixed-tilt systems as opposed to tracker systems [1.40]. These types of systems treat the solar radiation field as one unit. In other words, all panels are oriented in the same direction and tilted at the same angle, where they can all harvest energy in the same manner. Most people have driven by or seen PV arrays of this nature; think of an open field filled with row after equally spaced row of solar panels all tilted at the same angle.

As PV technology was born under the premise of collecting the sun's energy and converting it into electricity, it is no wonder that the first solar array, with a capacity of 1 MW, was installed near Hesperia, California at the end of 1982 [1.41], and the second solar array, with a capacity of 5.2 MW, was installed in California's Carrizo Plain in 1984 [1.42]. Both located in southern California and away from the coast, these locations are known for their fair weather and sunny skies, conditions which are favorable for harvesting direct sunlight.

In climates like these, where sunny conditions dominate, the standard arrangement of PV panels into equally spaced rows all oriented at the same tilt angle is optimal as the majority of the total GHI is composed of the direct normal beam. However, installations of large PV arrays have not been confined to the sunniest locations across the United States. Rather, five of the top ten solar states, ranked by the total amount of installed solar capacity, are located across the eastern U.S. [1.43], which is significantly cloudier than the desert southwest (i.e. southern California, New Mexico, Arizona, Nevada, and Utah). North Carolina is ranked second, Florida is ranked fifth, New Jersey in ranked seventh, Massachusetts is ranked eighth, and New York is ranked ninth. All of these states have between 1,775 MW installed capacity and 5,601 MW installed capacity, and cumulatively, can power the equivalent of nearly 2.3 million homes [1.43].

The locations of these PV arrays, paired with the fact that land prices across the eastern U.S. are generally higher than the rest of the country, with the exception of California [1.44], calls into question the current way in which PV arrays are designed. First, these locations are much cloudier than a place like southern California. This means that the radiation field varies widely; there are sunny days when most of the GHI is composed of the direct normal beam, there are overcast days when most of the GHI is composed of the diffuse field, and there are partly cloudy days when the composition of GHI can vary drastically hour-to-hour.

This dissertation focuses on applications and installations of large solar panel arrays in partly cloudy climates. First, the controls and variance of the total radiation field and average cloud cover across the United States are investigated, highlighting the importance of the diffuse field across several regions. This climatology quantifies how the radiation field varies both temporally and spatially across the country and examines how latitude, elevation, cloud cover, precipitable water, and the optical depth contribute to variations in the radiation field both on a national scale and on a regional scale. Second, an alternative approach of organizing large solar panel arrays is proposed based upon a combination of modeling and the radiation climatology. The technique treats the

DNI and GHI as two separate radiation fields as opposed to one and maximizes the amount of harvested solar energy within a constrained area, solving for both maximized incident energy on individual solar panels as well as maximized harvested energy within a set footprint using the fewest panels possible to meet a specified gain in energy. This is accomplished by having two separate tilt angles on a large solar panel array. In theory, one tilt is more optimized for the direct normal beam, while the other tilt is optimized for the diffuse field. It was found that this method worked best in partly cloudy climates, while this method was not suited for sunny climates. Third, and finally, the performance of two solar carport canopies oriented with different azimuth angles on the Livingston campus are compared relative to their orientation differences and to the local diffuse and direct insolation balance. The specifics of these projects are discussed below.

1.2 SCIENTIFIC OBJECTIVES

This body of work aims to answer the following principal questions:

1. *How do the components of the solar radiation field, including the direct normal beam and the diffuse field, vary on a national and regional basis across the United States and what are the primary meteorological and geographic factors driving the observed variation?*
2. *Can solar panel angle optimization techniques typically used in cloudier regions be modified to maximize the energy output per unit area of a solar array?*

3. *To what extent should the diffuse-to-direct ratio of the solar radiation field in cloudy areas impact the orientation of solar panels in design-constrained physical structures such as carport canopies?*

1.3 OVERVIEW OF DATA AND METHODOLOGY

1.3.1 Data Overview

The primary sources of data used in this dissertation include semi-modelled irradiance and meteorological data from the National Solar Radiation Database (NSRDB), observed irradiance data from the Rutgers Photochemical Assessment Monitoring (PAM) site, observed inverter data from the two carport solar canopies on the Rutgers' Livingston Campus, and typical meteorological year (TMY) data from the National Renewable Energy Laboratory (NREL) for Newark, NJ.

One primary source of the data analyzed in this dissertation was provided by the National Solar Radiation Database (NSRDB). The NSRDB is a spatially dense network of U.S. sites, many of which provide a 20-year period of record (1991-2010) of modeled solar radiation data as well as other standard meteorological variables [1.45]. Daily and hourly averages of global horizontal irradiance, direct normal irradiance, diffuse horizontal irradiance, optical thickness, column-averaged precipitable water, and cloud fraction were leveraged throughout this dissertation. While the NSRDB does ingest observational data from a much smaller network of solar measuring sites across the country, it also blends ground-based METAR data and top-down satellite data to create hourly retrievals of radiation data. A more detailed review of the components of the NSRDB and what went into the model are discussed in Chapter 2.

While pure observational data would have been preferred, there are only 40 sites around the country that provide a long enough period of record suitable for use for a climate study. A sample size this small would not have been suitable for a nation-wide climate study. The benefits of the NSRDB is that it was created specifically for use in climate studies. In other words, the solar irradiance profiles were meant to be representative of the statistical properties of the solar field on the time scale of a month or a year as opposed to being representative of the exact solar radiation field at a particular time on a specific day.

Further, only higher quality sites were used, which left 788 stations across the continental U.S. for use in the study. In Chapter 2, these 788 stations were first analyzed on a national level before being further broken down into eight geographically and climatologically different regions across the country. Meanwhile, the analysis during Chapter 3 was fixed at the national level.

Observed data from the Rutgers Photochemical Assessment Monitoring (PAM) Site are introduced and analyzed in Chapter 4. The Rutgers PAM Site is a permanent installation located on Rutgers Horticulture Research Farm 3 in East Brunswick, NJ and has been in continuous operation since October 1, 1994. More than three years of irradiance data from April 2016 to June 2019 was utilized, which included 1-minute observations of global horizontal irradiance and diffuse horizontal irradiance. Direct normal irradiance was simply the difference between the two observations.

Chapter 4 also includes the use of observed inverter data from the Rutgers Livingston Campus Solar Carport Canopy System. The Solar Carport Canopy System is comprised of two different parking lots (Lot 105 and the Yellow and Green Lot), both of which are covered by rows of solar panel canopies. Each canopy is split between a segment tilted at 15° relative to the horizon and a segment tilted at 1° relative to the horizon. Further, Lot 105 is rotated approximately 36° to the west from a due south orientation, while the Yellow Lot is rotated approximately 54° to the east from a due south orientation. There are a total of 14 Solaron 500 kW inverters between the two parking lots, 4 of which are connected to Lot 105 and 10 of which are connected to the Yellow and Green Lots. Inverter level data is provided in 15-minute intervals and data was downloaded from January 2016 to April 2019.

Finally, Chapter 4 also used typical meteorological year (TMY3) data for Newark, NJ, which was provided by NREL. TMY3 data are composed entirely of observed data that have been pieced together from many years in order to represent typical solar radiation and meteorological conditions over the course of a year. Thus, there is a year's worth of data, where every day can theoretically come from a different day in the past. Outputs of global horizontal irradiance, diffuse horizontal irradiance, direct normal irradiance, and extraterrestrial, or top of the atmosphere, irradiance were used.

1.3.2. Methodology Overview

In Chapter 2, a 15-year climatology of the NSRDB dataset is constructed from hourly integrated values of solar irradiance, which represent the cumulative daily total of incident solar radiation at each station location and which is reported in units of Watt-hours per square meter (Wh/m^2). These units make it unnecessary to correct for time zones or daylight savings times as they are representative of the entire day. Data were analyzed spatially (i.e. How does the solar radiation field vary across different regions of the country?) and temporally (i.e. How does the solar radiation field vary during the different seasons?). The composition of the diffuse field of radiation across the United States was investigated and evidence and reasons why the diffuse field varied were explained.

In Chapter 3, an alternative method for organizing large solar panel arrays is presented in which two different panel tilts are implemented across one solar panel array. This method, called the dual-angle solar harvest (DASH) method, looks at large solar panel arrays as a dual-optimization problem. The industry standard is to tilt a solar panel according to the angle at which the most energy can be generated. While this optimizes energy output for an individual solar panel, this method fails to consider the cost of land and space. The cost of buying and installing solar panels has significantly decreased, while the cost of land is generally rising. Thus, solar panel arrays should not only optimize the amount of energy that can be harvested from an individual solar panel, but they should also optimize for array-wide energy, or the total amount of energy that can be harvested from the entire array.

The DASH method is composed of a relatively simple model that represents the amount of solar irradiance incident on any tilted surface. Model inputs include diffuse and direct radiation, which came from Chapter 2. This model was then used to simulate the amount of harvested solar radiation across a large solar panel array of 100 rows using all combinations of pairs of angles broken down into all possible fractional splits.

In Chapter 4, observations from two different solar carport canopies on Rutgers Livingston Campus with the same panel tilt angle but different azimuth rotation angles are used to investigate how cloud cover and diurnal variations in the diffuse field affect the energy output. The solar carport canopy inverter-level data are compared to both observations of the solar irradiation field from the Rutgers PAM Site as well as the standardized TMY3 historical dataset from NREL.

First, the irradiance data from the PAM Site were used to construct a sky cover algorithm which diagnosed days into three bins: clear, variable, and cloudy. A similar algorithm was developed for the TMY3 data to corroborate the findings in the first algorithm. The PAM Site classifications were applied to the output from the solar carport canopies and differences in daily integrated energy output with respect to sky cover were discussed. Finally, the differences in azimuth twist (from due South) were investigated with regards to time-of-day on clear, variable, and cloudy days.

Chapter 2:

A Climatology of Solar Irradiance and its Controls across the United States: Implications for Solar Panel Orientation

2.1. INTRODUCTION

As the world population increases in the coming decades, the International Energy Agency has estimated that global energy demand will increase by an additional 30% between 2016 and 2040, with 40% alone coming from an expected increase in electricity usage [2.1]. Growing concerns about rising global air and sea surface temperatures as well as increasing public awareness about the harmful effects of non-renewable energy sources (i.e. oil, gas, and coal) have resulted in an expectation of governments to invest more money into cleaner, renewable energy sources. The 2017 Energy Outlook projected two thirds of future global investments for building new power plants to be focused on renewable energy by 2040, with the largest source coming from solar energy [2.1]. Thus, the global market share of solar photovoltaic (PV) energy is expected to continue rising.

Silicon PV cells, which are what comprise today's modern solar panel, were first introduced for outdoor use in 1955, as an initiative by Bell Laboratories [2.2]. These early PV cells operated with ~2% efficiency, but technological advances have steadily improved the efficiencies of operational PV cells to ~15 to 22.5% and research PV cells to ~46% [2.3]. This, paired with lowered costs of the production of PV cells, plus government subsidies and incentive programs to further reduce the cost of solar panel installations, has led to the growth of the fraction of solar energy that is powering the US electrical grid.

Besides increasing a PV cell's efficiency to convert solar energy to electricity, the electrical output of a PV cell is also highly dependent and limited to the fraction of the solar energy that is incident on its surface, which is dependent on sky cover, elevation, latitude, and cell orientation relative to the solar radiation field. Sky cover is constantly changing, so weather conditions and associated cloud cover are an important determinant upon the sum of electricity that can be produced by a solar panel at a given time and location.

The incoming solar radiation field, which is to be harvested by solar panels, consists of a direct component and a diffuse component. The direct component is received exclusively from the small portion of the sky occupied by the solar disk and the diffuse component is radiation received from all other directions within the celestial hemisphere. The diffuse component is only a small fraction of the direct component in cloudless skies, consisting primarily of the portion of incoming radiation scattered by air molecules, which lies mostly in the blue wavelength portion of the visible spectrum. Aerosols and, particularly, cloud cover increase the diffuse component of incoming solar radiation, and when the sun's disk is no longer visible through overcast, virtually all incoming radiation is diffuse.

Since the initial passage of the U.S. Solar Investment Tax Credit (ITC) in 2006, the amount of new solar farms, or land areas entirely devoted to the installation of large solar panels, as well as solar panel installation on top of both commercial and residential buildings has largely increased. In the past decade alone, solar energy has experienced an annual growth rate of 50%, with the largest growth coming from solar farm installations [2.4].

While the efficiency of a solar panel can be maximized by using a tracking system to follow the motion of the sun, the cost and maintenance of such systems are prohibitive for wide scale use; the use of a single tilt angle is much cheaper to maintain [2.5]. A simple rule of thumb at a solar farm is to orient the rows of solar panels southward (in the northern hemisphere) and angled according to the latitude of the site [2.6] (or placed on the southernmost-facing side of the roof) so that a panel will be roughly orthogonal to the sun's disk at noon. This orientation has been preferred because, when skies are clear or mostly sunny, the direct beam of solar radiation contains more energy per meter squared than the diffuse field. Meanwhile, the ideal way to orient a solar panel to harvest diffuse radiation, such as when skies are overcast, is to orient them flat (i.e. orthogonal to the local zenith) [2.7]. Locations are rarely ever always sunny or always overcast; most locations can be characterized by variable weather conditions. While more complex, determining and calculating the optimal fixed tilt angle has been widely researched using different approaches [2.6-2.12]. These studies make it clear that optimizing the efficiency of the solar harvesting process may be impaired by the exclusive use of all latitude angled or all flat oriented solar panels.

The purpose of this paper is to produce a climatology of the components of the solar radiation field such that regions can be identified in which harvesting diffuse light may contribute substantially to the total output of solar panels and panel arrays. Previous studies have analyzed the regional and continental scale of global horizontal irradiance and its variance across the US and other countries [2.13-2.18], but none, to our knowledge have expanded this to include the climatology of diffuse radiation or the meteorological variables driving the variation in solar irradiance.

This climatology is produced by analyzing the seasonal cycles of solar radiation across individual locations within the US and across eight separate US climate zones. This analysis can be used to determine which areas of the US are best suited for expansion of solar energy development, and which areas might benefit from a combined direct-diffuse harvesting strategy to maximize the harvesting of solar energy using solar panels.

2.2. MATERIALS AND METHODS

Data from the U.S. Department of Energy's National Solar Radiation Database (NSRDB), which is a high-density network of U.S. sites containing modeled hourly radiation data for the 20-year period spanning from 1991 to 2010, were used in this study [2.19]. The NSRDB contains measurements and retrievals of the components of the solar radiation field (global horizontal, direct normal, and diffuse horizontal irradiance) as well as several meteorological quantities.

Figure 2.1 depicts the spatial distribution and classification of the NSRDB stations where the classification numbers (I, II, or III) refers to the length and quality of record for each site. Only class I and class II stations are utilized for this study, as they contain higher quality data compared to class III stations. While observed data would have been preferable, there is no network of observed radiation data which provides the same degree of spatial and temporal data coverage as that of the NSRDB that can be used to accurately represent regional solar radiation climates. While the NSRDB does take into account the available sites with observed data, these only account for less than 1% of the entire data record.

An in depth evaluation of the NSRDB model to the measured data is included in the NSRDB handbook [2.19], where it is shown that the mean bias error (MBE) for global horizontal irradiance ranges from -0.06% to 1.73%, the root mean square error (RMSE) ranges from 5% to 8%, and the R^2 value ranges from 0.83 to 0.85. Much of this error can be encompassed by the error of the observations themselves, which ranges from 5% to 10%. For a climatological study, these ranges of errors are acceptable and are minimized at longer time scales.

Each station in the NSRDB contains hourly records of irradiance values. These hourly records indicate the integrated total solar irradiance at a particular site during the hour prior to the observation time rather than a single point observation at the hour of observation. Even though the NSRDB data contains hourly averaged values of modeled solar radiation, the intent of this modeled dataset is to provide the statistical properties of solar radiation, on a time scale of a month or a year, that are as close as possible to the actual observed statistical properties of measured solar radiation. The modeled data within the NSRDB network are produced by two modeling schemes: a meteorological-statistical model (METSTAT) [2.20] and a model created by the State University of New York (SUNY) [2.21].

The SUNY model uses satellite radiation measurements from the two Geostationary Operational Environmental Satellites (GOES) that cover the US (the

GOES-east and the GOES-west) and assumes an inverse relationship between radiation reflected into space and radiation that reaches the surface. For example, if the GOES satellite measures a large amount of reflected radiation, there is either cloud cover or a relatively "dense" atmosphere (i.e. a high abundance of reflective pollutants, moisture, or other molecules), or a combination of the two, and thus the modelled surface irradiance will be smaller, as less of the sun's radiation makes its way to the surface.

The METSTAT model uses National Weather Service (NWS) observations of total and opaque sky cover as well as measured solar radiation data from the Solar Radiation (SOLRAD) network. Observations of sky cover were initially made by humans, but with the implementation of automated surface observing systems (ASOS) at many sites in the early 1990's, these human observations were replaced with estimates from a ceilometer, which measures cloud base heights up to several layers if the cloud layers are optically thin. When the lowest cloud layer is optically thick and it is completely overcast, the ceilometer can only measure the base of the lowest cloud layer. Because a ceilometer measures cloud coverage directly overhead, a problem results when a persistent cloud deck is directly above the ceilometer but no clouds in other quadrants of the sky exist. In this case, the resultant observation of overcast skies may be unrepresentative of the areal cloud coverage that influences the entire solar radiation field. Further, ceilometers possess height limitations and, therein, frequently under-sample high clouds which otherwise would have been seen by human observers and are unable to distinguish between total and opaque sky cover. To compensate for this discrepancy in data between the original manual and the newer ASOS weather stations, the National Climatic Data Center's (NCDC) ASOS Cloud Data Set was used, which estimates total and opaque sky cover (in tenths) using cloud height information from satellite imagery.

However, even with this implementation of ASOS cloud data, the METSTAT model's uncertainty in cloud cover, especially when cloud cover is broken or scattered, is higher than with the SUNY model. This is a byproduct of the zenith-pointing ceilometer's narrow, overhead-only sampling volume. Clouds in a broken cloud field may block the direct beam during some portion of a given hour with a frequency that is not well-represented by the ceilometer measurement. To compensate, the METSTAT model uses a random number generator to draw from a cumulative probability distribution of measurements of the impacts of this cloud-blocking effect before the transmittance is computed.

The SUNY model utilizes one method to calculate the total and opaque sky cover in its entire period of record, while the METSTAT model transitions from human-based total and opaque sky cover observations to a combination of ceilometer and ASOS derived total and opaque sky. For simplicity, the NSRDB dataset would have been comprised of SUNY data alone; however, the GOES satellite imagery was only archived beginning in 1998, which would have ignored the earlier METSTAT data collected from 1991-1997. Thus, a combination, or hybrid, of the SUNY and METSTAT models is used.

Besides providing hourly integrated amounts of solar radiation at all of its sites, the NSRDB also contains statistical summaries of class I and class II stations for the years 1991 to 2005. These statistical summaries, which contain monthly and annual means of solar radiation (total, direct normal, and diffuse), sky cover at each station, and meteorological variables, are computed from the hourly data. There are also 15-year means (i.e. the entire dataset) of these monthly and annual means. Standard deviations for each hour of the day (i.e. the variability) as well as for each month and year of these quantities are also computed and included. These summaries are used in this study.

In this study, we analyze the direct and diffuse solar radiation, total sky cover, opaque sky cover, and aerosol optical depth. Both the direct and diffuse radiation are reported in watt-hours per square meter (Wh/m^2). This unit can be interpreted as the integration, or summation, of incident solar irradiance, reported in W/m^2, on a surface over the course of an entire day (from sunrise to sunset). While a W/m^2 represents a snapshot of the sun's energy on a surface at a given time, a Wh/m^2 represents the total over the entire day. A higher value may not only represent a location that is further south in latitude (in the Northern Hemisphere), but also the length of day, which varies station to station (dependent on latitude) and day to day (dependent on season). Both quantities are resolved to within 1 Wh/m^2.

In the statistical summaries, total and opaque sky cover are reported in tenths where a value of zero represents completely clear skies and a value of ten represents completely overcast skies. Sky cover does not elucidate separate cloud layers; it is an integrated quantity. Opaque sky cover refers to clouds that have a cloud optical thickness greater than eight, which means that no direct radiation passes through them. Examples of generally opaque cloud types are stratus clouds, cumulonimbus, or stratocumulus clouds [2.22]. This genre of cloud types does not include thin, more transparent, cirrus ice clouds that frequently reside in the upper troposphere. Total cloud cover refers to all types of clouds with any optical thickness value. Subtracting opaque sky cover from total sky cover identifies optically thin clouds. While there is no way to associate these transparent clouds with a particular cloud type, we note that the seasonal distribution suggests that at least some of these clouds are likely to be cirrus [2.23-2.25].

2.3. RESULTS & DISCUSSION

A solar panel in Maine is not going to harvest the same amount of solar energy over the course of a year as a solar panel in California. But what about a solar panel in New Jersey compared to a solar panel in Iowa? In this analysis, we investigate the atmospheric and geographic drivers that dictate the variation of direct and diffuse radiation across the US. We first examine the spatial distribution by season to determine where direct and diffuse radiation is maximized and how it varies throughout the year on the continental scale. Next, we divide the country into eight specific regions chosen based on general climatological and geographical similarities and analyze the temporal distribution of direct and diffuse radiation on this regional scale. Finally, we discuss the need for some regions of the US to optimize the collection of diffuse radiation in order to maximize the collection of solar energy.

2.3.1. Continental Scale Radiation

In this section we summarize the continental scale radiation field and analyze the contributing factors that lead to the observed distribution of radiation.

2.3.1.1. DIRECT BEAM RADIATION

Figure 2.2 displays the average direct beam radiation in Wh/m^2 across the continental US in three-month seasons. Each of the individual stations, representing each data point, is shown by an open circle and a linear interpolation scheme, from Python's *matplotlib.mlab* library and *griddata* function, was used to fill the gaps between stations. Values can be interpreted as the average summation of radiation that was accumulated over the course of an hour for each three-month season. Thus, these values do not represent the highest possible amount of hourly accumulated radiation at a given location.

The primary determinants of direct radiation are latitude, elevation, atmospheric particles and cloud cover, the latter two of which vary seasonally. Latitude (i.e. the north-south relationship) is the dominant factor during the winter months, and to some extent the fall months, as indicated by the higher R^2 values in panels (a) and (d) in Figure 2.3. However, latitude is not the only control during these months, otherwise the R^2 value would be even closer to 1. In the winter plot (Figure 2.2a), the radiation difference between southern California (~ 5,000 Wh/m^2) and central Georgia (~4,000 Wh/m^2), which are both located at about the same latitude, is ~1,000 Wh/m^2. Thus, the direct radiation in southern California is 25% greater in central Georgia. Meanwhile, the difference between southern California (~5,000 Wh/m^2) and northern Oregon (~2,500 Wh/m^2), which are approximately the same longitude, is ~2,500 Wh/m^2. Thus, the direct radiation in southern California is double that in Oregon and, in summary, fall and wintertime direct radiation vary the most latitudinally, or going north to south.

During the summer months, longitude (i.e. the east-west relationship) becomes the dominant factor in direct radiation variance, as can be seen by the high R^2 value in Figure 2.4c. Unlike during the winter months, there is close to a 5,000 Wh/m^2 difference in direct radiation between southern California (~9,000 Wh/m^2) and central Georgia (~4,000 Wh/m^2) (Figure 2.2c), which is five times the difference compared to the winter months. Further, the direct radiation difference between northern Oregon (~7,500 Wh/m^2) and southern California (~9,000 Wh/m^2) is approximately 2,500 W/m^2, and much less than the doubled value difference observed in winter. Thus, the direct radiation variance is largest longitudinally, or going east to west.

One factor that influences non-latitudinal differences in the radiation field is elevation. Locations at a higher elevation experience less scattering and reflection of solar radiation because there is less atmosphere through which the incoming beam traverses before reaching the surface. Moreover, the atmosphere above these locations is generally drier and "cleaner", which means less absorption of solar radiation by water vapor and less atmospheric particles through which to be scattered or reflected. There is also less humidity-related swelling of the hygroscopic aerosols that are present. The elevation at each station is depicted in Figure 2.5. The larger the circle and the deeper the color, the higher the elevation. Not only does the West Coast have higher mountains (The Rockies versus the Appalachians), but the ground surface in general (not including the mountains) slopes upward from about the Ohio River Valley to the Rocky Mountain Range. This can be seen by the gradual increase in size of the station dots from about 85ºW to about 100ºW. While the Plains across the central US might seem flat, they are actually gradually sloping upward to the west. Thus, elevation alone can account for some of the longitudinal difference in direct radiation; however, it cannot explain why there is an east-west relationship with direct radiation in the summer and spring, while there is a north-south relationship during the fall and winter.

A second factor that can alter the direct radiation field is the type of particles in the air. Smoke, pollution, sea salt, and water vapor are all types of particles that can significantly scatter or reflect incoming solar radiation dependent on their concentrations. One way to measure particles and their effect on the “transparency” of the atmospheric column is with aerosol optical depth (AOD). Figure 2.6 depicts the average AOD in three-month time steps. In general, AOD is higher across the eastern US compared to the western US. The dense population across the eastern US and its resultant pollutants are largely responsible for this distribution. This is particularly notable across the Northeast, which has a higher optical depth than the Southeast during the winter and spring months. Along the West Coast, AOD is also high, especially compared to the interior west. This local maximum in AOD can be attributed to population density and a lesser contribution from sea salt. The highest values of AOD across the Northwest quadrant of the country occur during the summer and fall months, when wildfires are prevalent.

A third factor is cloud cover. It is well known that a larger portion of the direct normal beam will be scattered, reflected, or refracted when passing through a cloud layer than when passing through clear air. Figure 2.7 depicts the average total sky cover for every three-month season. In general, cloud cover is generally lower across the Southwest US compared to the Southeast US for every season. During the winter months, there is a strong north-south gradient in cloud cover with higher cloud cover towards the north and lower cloud cover towards the south. This mirrors the north-south relationship observed with direct radiation during the winter months. As this same variation does not exist with AOD, it stands to reason that the distribution of direct radiation during the winter is primarily driven by cloud cover versus AOD. Further, there is a strong east-west gradient in cloud cover during the summer months with much lower cloud cover across the western US and much higher cloud cover across the eastern US. Thus, the temporal variation of cloud cover generally mirrors the continental distribution of direct radiation.

From these four factors (latitude, elevation, AOD, and cloud cover), we can conclude that elevation plays a significant role in modulating direct beam radiation year-round, latitude plays the largest role during the fall and winter months, and AOD and cloud cover play the largest roles during the spring and summer months.

2.3.1.2 DIFFUSE RADIATION

Continental scale diffuse radiation is comprised of direct beam radiation that is scattered, reflected, or refracted by small molecules in the atmosphere, cloud cover, and near-surface obstacles, such as buildings or vegetation. Figure 2.8 displays the average seasonal diffuse radiation in Wh/m^2 observed at each site. As with direct radiation, there is a north-south gradient during the winter and fall months and an east-west gradient during the summer months, as can be seen by the high R^2 values in Figures 2.9a, 9d, and 10c. The north-south gradient during the fall and winter is attributable to latitude, as with direct beam radiation, and the east-west gradient is modulated by water vapor loading and cloud cover during the summer. Thus, where direct radiation is higher (i.e. the Southwest), the diffuse radiation has a local minimum, while where the direct radiation is lower (i.e. the Southeast), the diffuse radiation has a local maximum. In other words, it varies inversely, as expected.

2.3.1.3 DIFFUSE-TO-DIRECT RADIATION

Perhaps more important (and more telling) than the distribution of direct beam and diffuse radiation alone is the distribution of the ratio of diffuse to direct radiation, which is shown in Figure 2.11. Unity in this figure indicates equal amounts of direct and diffuse radiation while a value close to zero indicates that that direct radiation is dominant.

While the east-west gradient is most pronounced in summer, it is also prominent during the other seasons, unlike the individual components of direct and diffuse radiation, which implies that moisture, cloud cover and elevation play key roles throughout the year. This ratio, plotted against longitude with the associated R^2 values, can be seen in Figure 2.12. The R^2 values with respect to latitude were all much smaller; thus, there is not a significant latitudinal relationship. Locations across the eastern half of the country, as well as along the coastline of the western US, generally have a higher ratio of diffuse to direct radiation, while locations across most of western US generally have a lower ratio. So not only is the amount of direct radiation across the eastern US lower than across the western US, but the proportion of diffuse to direct radiation is greater. One can imagine that the east-west R^2 values would be much higher were it not for the elevated ratios along the West Coast. However, this means that the sensitivity of diffuse radiation when it comes to installing solar panels along the West Coast is similar to the sensitivity across the eastern half of the country.

2.3.2 Regional Scale Radiation

We divided the 788 individual class I and class II stations into eight separate regions: The Northeast (NE), the Southeast (SE), the Midwest (MW), the South-Central

(SC), the Plains (PL), the Northwest (NW), the Southwest (SW), and the desert Southwest (DE). These regions can generally be classified by their geography as well as their climatology. The geographical breakdown of these eight regions can be seen in Figure 2.13, while the specific number of stations per region can be seen in Table 1. In each region, we calculated the 15-year average value (1991-2005) of direct radiation (Wh/m^2), diffuse radiation (Wh/m^2), the ratio of diffuse to direct radiation, total sky cover (tenths), opaque sky cover (tenths), the difference between total and opaque sky cover (tenths), and AOD. Our analysis begins with a description of the meteorological factors that modulate the radiation fields in the eight regions and concludes with an analysis of the radiation fields themselves.

2.3.2.1 METEOROLOGICAL MODULATORS OF REGIONAL RADIATION

As aforementioned, cloud cover and AOD are the two primary meteorological factors that alter the distributions of direct and diffuse radiation. When there is significant coverage of optically thick clouds, the absorption of solar radiation by water vapor is secondary to the scattering of radiation by cloud droplets and ice crystals [2.26]. When optically thin cirrus ice clouds are the only cloud present in the sky, radiation transfer calculations show that the absorption by water vapor is an important factor in determining the amount of direct-beam radiation that reaches the surface.

Figure 2.14 depicts the 15-year monthly mean envelope of monthly mean minimum and maximum hour-integrated irradiance for total and opaque sky cover as well as the difference between the two, which is a proxy for cirrus and optically thin clouds.

In general, cloud cover is maximized during the winter months and minimized during the summer months, although regional differences are evident. Of particular note are the large seasonal changes in total and opaque cloud cover in the Northwest, Southwest, Plains, Midwest, and South-Central regions, and the relatively small seasonal variability across the desert Southwest, Northeast, and Southeast. The Northeast and Southwest have particularly wide ranges of total and opaque cloud cover during the summer months in this 15-year record.

While opaque, or optically thick sky cover, such as stratus or cumulus clouds, has the largest effect on incoming solar radiation, the effect of thinner, more transparent cloud cover, such as cirrus clouds, is not insignificant. Regional variations in cirrus cloud cover are compared in Figure 2.15. In general, cirrus and other optically thin clouds are more frequently observed in summer, which is opposite the pattern of total and opaque cloud cover. This is likely because they are residuals of convection, which generally occurs in the spring and summer months. The desert Southwest has the most unique time series because the seasonal frequency of cirrus and optically thin clouds is bimodal with a peak in February and then again in May. This second peak corresponds to the monsoon circulation over the desert Southwest, which generates deep convection.

Regional aerosol optical depth (AOD), shown in Figure 2.16, peaks during the summer months across all regions, while cloud cover (Figure 2.14) generally peaks during the winter months. Thus, the variance of AOD is not directly correlated to cloud cover, but rather varies due to the concentration of atmospheric particles, such as sea salt, anthropogenic pollution and smoke. There is also an increase in AOD from west to east, which is likely largely due to higher concentrations of water vapor across the eastern US, which swell aerosol particles. This is due to its proximity to the atmospheric rivers that flow from the tropics into the Gulf of Mexico as well as higher concentrations of pollution and aerosols from the higher density of human population across the eastern half of the country. The highest AOD is observed across the Southeast US, and as the mean is close to the upper bound of the envelope, this can be interpreted that most of the years feature high values of AOD in this region. In general, the variability, or year-to-year range of AOD across the southwest quadrant of the country is largest, which means that the annual diffuse component also varies most in that region.

2.3.2.2 REGIONAL SCALE DIRECT AND DIFFUSE RADIATION

Figure 2.17 displays the average 15-year mean monthly direct and diffuse radiation along with the range and the standard deviations for each region. The peaks in direct radiation during the summer are, of course, expected, as there are more hours of sunlight; however, since the summer solstice occurs in June, if latitude and season were the only factors modulating the radiation field, the peaks would also occur in June. Because the peaks are not always observed in June, the timing of the peak in direct beam radiation cannot entirely be explained by the maximum solar output; cloud coverage and AOD also influence the timing.

2.3.1.3 REGIONAL SCALE DIFFUSE-TO-DIRECT RADIATION

The seasonal breakdown of diffuse-to-direct radiation is shown in Figure 2.18. Unlike Figure 2.19, which depicts the amount of diffuse radiation that could be harvested in each region, Figure 2.18 adds another dimension of operational significance because the seasonal diffuse-to-direct ratio portends the fractional amount of each component of the radiation field will be available for harvesting. Similar seasonal trends are found in the Northeast, Southeast, South-Central, and Midwest regions where a preponderance of diffuse radiation during the late spring, summer, and early fall suggests that more efficiently harvesting diffuse radiation may be a useful and profitable endeavor. Similar trends are found in the Southwest, desert Southwest, and Plains, where harvesting of direct-normal radiation is preferred. Radiation in the Northwest region cross-cuts these two regional signal clusters. In that region, there is a suggestion that improving the efficiency of diffuse radiation harvesting in all but the summer months may be the best approach, while preferential harvesting of direct-normal radiation during the summer season is recommended. It should be dutifully noted that the seasonal variability in the diffuse-to-direct radiation field in the Northwest and Southwest (Figure 2.17), and to a lesser extent the Plains and desert Southwest, have a considerable range over this 15-year sample period. This variability is attributable to larger climate signals, whereupon these regions may require tweaking of the solar harvesting strategy based upon seasonal weather signals, such as El Nino and La Nina.

2.4. CONCLUSIONS

The study described herein presents an analysis of the National Solar Radiation Database (NSRDB) to provide a comprehensive 15-year climatology of direct and diffuse radiation, as well as cloud cover and AOD across the United States. The radiation field at the continental scale and across eight climatologically and geographically similar regions is examined. On a continental scale, the climatology of direct radiation varies in two key ways depending on the time of year. The fall and winter months exhibit a prominent north-south variation in direct radiation driven by the solar zenith angle, while the spring and summer months exhibit a larger east to west variation in direct radiation that is most dependent on a site's elevation, AOD and cloud cover. Frequent cloud cover across the eastern US combined with generally lower elevations relative to the western US enable more diffuse radiation to reach the surface in the eastern US.

The diffuse-to-direct ratio relates directly to the question of solar panel orientation. As previously stated, solar panels are typically permanently oriented so that their flat surface is, on average, nearly perpendicular to the direct beam, which enables efficient harvesting of direct radiation. When there is a predominance of diffuse radiation, this orientation is less than optimal. Across the eastern US, where there is more diffuse radiation, this analysis raises the question as to what fraction of fixed-angle solar panels should be dedicated to harvesting direct beam and what fraction should be dedicated to harvesting the diffuse field. It further suggests that solar energy collection efficiency might be substantially improved if solar panel orientation were tuned to a location's elevation, average sky cover, and AOD. These properties vary from region to region, which motivates a more granular analysis that accounts for regional variations in these properties to guide operations.

At a regional scale, the diffuse-to-direct ratio varies most from May to September. Regional gradients in elevation, cloud cover, and AOD modulate this variance. Both cloud cover and AOD are maximized east of the Mississippi River, but AOD peaks in summer, while cloud cover peaks in winter. A steadily increasing AOD and the accompanying increase in solar absorption and scattering lessens the efficiency of the harvest of direct beam radiation from west to east in clear skies and when optically thin clouds are present. Steadily increasing opaque cloud cover from west to east methodically increases the scattering (reflection) of incoming solar radiation to space and redistributes radiation from the direct beam to the diffuse field. Thus, a dwindling amount of direct beam radiation is available for harvest. The Northeast, Southeast, Midwest, and South-Central have a fundamentally different radiation field from May to September than the Southwest, Plains, and desert Southwest; there are significantly larger diffuse-to-direct ratios in the former regions. The Northwest exhibits a changeable diffuse-to-direct radiation field that features greater diffuse beam radiation during May and June due to cloud cover and greater direct beam radiation from July through September.

Among the more interesting aspects of this analysis is the 15-year range of diffuse-to-direct radiation from the western to eastern regions. Western regions experience much greater year-to-year variability as a result of large-scale climate signals, particularly the El Niño Southern Oscillation cycle (ENSO). The gradient in the year-to-year range across the western US suggests that adaptive harvesting strategies, which consider larger climate signals and their impact on the ratio of diffuse-to-direct ratio, may be required to fully exploit the available solar radiation. Conversely, the relatively narrow range of year-to-year variability in the diffuse-to-direct ratio in the eastern US suggests that a relatively constant harvesting strategy that optimizes the fractional harvesting of diffuse and direct radiation, depending on location, should be preferred.

Our analysis depicts a complex seasonally-changing directional solar radiation field across the US that is driven by geographic factors such as latitude, elevation, surface coverage and by meteorological conditions such as cloud coverage, cloud transmissivity, aerosols, relative humidity, and column water vapor. Efficiently harvesting this radiation requires a solar-panel collection strategy that is tuned to radiation field and its modulators. Strategies that enable more efficient harvesting of diffuse solar radiation east of the Mississippi and that consider year-to-year variations in the Northwest and Southwest, especially during the summer months, should significantly increase the efficiency of the yearly and seasonal solar radiation harvest in these regions. It is likely, even certain, that proper tuning of solar harvesting systems to the match the directionality of the radiation field may increase harvesting efficiency at a rate that greatly exceeds increases in the efficiency of the PV cells alone.

Benghamem [2.27] propose optimal tilt angles for individual solar panels to maximize the simultaneous harvesting of direct and diffuse radiation. The suggested angles for panels are smaller in the summer months to enable more efficient harvesting of diffuse radiation. Another approach may be to devote a specified percentage of solar panels to the harvesting of diffuse radiation by placing them flat (orthogonal to the local zenith), while leaving the balance at a fixed angle that maximizes the collection of direct beam radiation. In a follow-up paper, we will use the climatology of direct and diffuse radiation and moisture variables analyzed in this study to calculate the optimal configuration of solar panels in the US by region and to study the effects of larger scale climate signals upon the harvesting strategy in different regions.

Chapter 3:

The Dual Angle Solar Harvest (DASH) Method: An Alternative Method for Organizing Large Solar Panel Arrays that Optimizes Incident Solar Energy in Conjunction with Land Use

3.1. INTRODUCTION

Rapid growth, both worldwide and in the United States, has been observed in the deployment and use of solar panels as a renewable energy source [3.1-3.3], which can be attributed to cost reductions and improved efficiencies. Over the past 40 years, costs to manufacture and purchase solar panels have significantly decreased, which can largely be credited to growing economies of scale (i.e. larger manufacturing plants), a decrease in the price of base materials, and improvements via research and development [3.4]. Meanwhile, the efficiency of photovoltaic (PV) cells over the past 60+ years has increased from ~2% to upwards of 15-22.5% [3.5]. Among energy technologies, the most rapid decline in price has been observed with photovoltaics [3.6].

Commercial or utility scale PV arrays are able to provide tens or even hundreds of thousands of homes with power annually; however, they require large parcels of land, which are neither infinite nor free. Rather, the cost of land has generally been rising with time [3.7]. Solar panel rows must be adequately spaced in order to minimize shadowing effects of the rows in front; the higher the tilt angle, the larger the row spacing required.

A study carried out by the National Renewable Energy Laboratory (NREL) estimated that 5.8 to 9.0 acres of land were required for each installed MW of PV capacity [3.8]. For example, the 290 MW Agua Caliente PV array in Yuma County, AZ is comprised of more than 5 million solar panels and encompasses more than 2,000 acres of land [3.9].

Many studies exist which have diagnosed the optimal tilt angle for individual solar panels to ensure the highest energy output per panel. The amount of energy that a solar panel can harvest is a function of (1) the efficiency of the PV cell itself, (2) the amount of insolation that is available at a given location, (3) the angle and direction at which the solar panel is oriented, and (4) the proximity to objects or obstructions that can cause shadowing. Some studies have focused on dual-axis sun tracking systems, which move in tandem with the sun's position both horizontally and vertically [3.10-3.14], while other studies have focused on fixed angle solar panels which do not move [3.15-3.31].

However, due to rising costs of land and decreasing costs of PV modules, the arrangement and orientation of solar panels as part of a large solar panel array should be part of a co-optimization problem in which both the per-panel energy output is optimized along with the array-wide energy output of all panels within a given footprint. Panels at slightly lower tilt angles than the optimum tilt angle can be spaced closer together without sacrificing large amounts of possible energy output. Panels at much higher tilts can also be spaced closer together; however, they sacrifice a much larger portion of incident radiation. Secondary benefits of these lower tilt angles include reduced inter-row shadowing effects, reduced inter-row masking of the diffuse field, and better orientation for harvesting of the diffuse field of radiation, suggesting improved results in cloudier climates.

In this paper, we propose an alternative method of organizing large solar panel arrays by tilting panels within an array at two different angles. This approach, which we have called the dual-angle solar harvest, or DASH, method, allows for more rows of solar panels to be installed in an area of the same size as an array where all panels are tilted according to the optimal tilt angle. This is accomplished with a fraction of the panels tilted at an angle lower than the optimum tilt angle, thus allowing some of the rows to be spaced closer together as the length of the panel shadow is smaller.

Array-wide panel-incident radiation with the DASH method is compared to array-wide panel-incident radiation for an array of the same footprint comprised of all panels tilted at the single optimum tilt angle. We demonstrate that significant gains in solar array harvest efficiencies may be realized with implementation of the DASH method. The DASH method is not suitable for all locations and it can be implemented on a case-by-case basis as solar array developers must make the decision whether or not to spend more money up front on extra solar panels that can fit into the same amount of space as an array where are panels are tilted at the optimum tilt angle.

3.2. MATERIALS AND METHODS:

3.2.1 Data

Hourly integrated modeled radiation and cloud cover data from NREL's National Solar Radiation Database (NSRDB) were used in first modeling the amount of plane of array (POA) irradiance on a solar panel and then on an array. The NSRDB is comprised of a dense network of 1,454 stations across the U.S. and is filtered by the quality and completeness of each record (Figure 3.1). Each higher quality station (Class I and Class II data) has a companion monthly average hourly statistics file for each year in the 20-year period of record from 1991 to 2010, which provides hourly profiles of global horizontal irradiance (GHI), direct normal irradiance (DNI), and diffuse horizontal irradiance (DHI). Each hourly value represents the average summation of radiation over the given hour for that month and for that year. The intent of the NSRDB is to provide statistical properties of the components of the solar radiation field on a time scale of a month or a year; it is not intended to be used for point measurements [3.32].

In a companion study [3.33], we constructed a detailed climatology of the components of solar radiation and analyzed their geographic and atmospheric drivers (i.e. elevation, latitude, cloud cover, and aerosol option depth), using only the 858 higher quality Class I and Class II station data. While observed data would have been preferable, no network exists which provides the same level of spatial and temporal data coverage. Even though most stations contain modelled data (there are 40 sites with purely observed data), they are based on measurements and observations from the two Geostationary Operational Environmental Satellites (GOES-east and GOES-west) as well as the National Weather Service (NWS) and the Solar Radiation (SOLRAD) network.

Further, a comprehensive evaluation of the NSRDB model was performed and is included in the NSRDB handbook, in which it was found that the mean bias error for global horizontal irradiance ranges from -0.06% to 1.73%, the root mean square error ranges from 5% to 8%, and the R^2 value ranges from 0.83 to 0.85 with much of this error being attributed to the 5-10% error in the observations themselves [3.32].

A main conclusion in our companion study [3.33] was the large component of diffuse radiation that existed with respect to direct radiation across portions of the eastern U.S. as well as across the coastal Pacific Northwest. It was demonstrated that in these regions, diffuse radiation accounts for a relatively large proportion of the amount of global irradiation. Moreover, it was demonstrated that the cloud fraction, and to a lesser degree, higher values of aerosol optical depth (such as from anthropogenic sources around densely populated zones) contributed to this increase in the relative amount of diffuse irradiance.

During the spring and summer months, when the sun's energy density is maximized and when the harvesting of solar radiation via solar panels results in the highest energy generation, the diffuse-to-direct ratio was found to be between 60-80%. Thus, orienting solar panels to be preferentially tilted towards the highest sun angle, which is optimized for harvesting the direct beam, is not optimal in locations shown to exhibit a high diffuse-to-direct ratio.

3.2.2 Method

Section 3.2.2.1 describes the approach used to model the amount of solar radiation incident on a single tilted solar panel and selects the single optimum tilt angle, β_{opt}. Section 3.2.2.2 then applies this technique to a 100-row array of solar panels tilted at the optimum tilt angle, calculating the minimum spacing between rows and adding inter-row shadowing effects. Section 3.2.2.3 then applies these equations to the DASH method. Two test locations are used to investigate all combinations of pairs of angles tested against the footprint of a 100-row β_{opt} array. Then, the DASH method is applied nationally with β_1 set to β_{opt} to see how small changes in some panel tilt angles can have a significant effect on the array-wide incident solar energy.

3.2.2.1. PLANE-OF-ARRAY RADIATION

The first step in modeling the amount of incident radiation across an array using the DASH method was to model the amount of energy incident on a single tilted panel every hour. Figure 3.2 depicts the geometry of the sun with respect to a solar panel that is tilted. In its simplest form, total incident solar flux on a surface tilted at angle β can be reduced into three components as:

$$F_{TOT,\beta} = F_{DIR,\beta} + F_{DIF,\beta} + R_g \tag{1}$$

Where $F_{DIR,\beta}$ is the direct beam radiation on the tilted surface, $F_{DIF,\beta}$ is the diffuse radiation on the tilted surface, and R_g is the ground reflected radiation on the tilted surface [3.34]. It should be emphasized that $F_{TOT,\beta}$ represents the energy incident on the solar panel every hour, not the energy harvested from the solar panel. The total amount of energy harvested depends on a solar panel's efficiency, which varies for different solar panels. Thus, the values of $F_{TOT,\beta}$ in this study do not represent the solar energy that is converted to usable energy.

The direct beam radiation on a tilted surface was modelled in the same way as many other studies, including Passias and Källbäck [3.35] and Hay [3.36], where $F_{DIR,\beta}$ is simply a function of the direct normal component of radiation, *DNI*, and the angle of incidence of the radiation beam on the tilted surface, θ_i:

$$F_{DIR,\beta} = DNI\ (\cos\theta_i) \tag{2}$$

The angle of incidence is a function of the panel tilt angle, β, the solar declination angle, δ, the solar hour angle, ω, the azimuth angle at the surface, γ, and the latitude angle, ϕ:

$$\cos\theta_i = \cos\delta\cos\omega\,(\cos\gamma\sin\beta\sin\phi + \cos\phi\cos\beta) + \sin\delta\,(\sin\phi\cos\beta - \cos\gamma\cos\phi\sin\beta) + \sin\gamma\sin\beta\cos\delta\sin\omega \tag{3}$$

As all solar panels in the project are oriented due south, such that $\gamma = 0$, (3) can reduce to:

$$\cos\theta_i = \sin(\phi-\beta)\sin\delta + \cos(\phi-\beta)\cos\delta\cos\omega \tag{4}$$

In literature, the diffuse radiation on a tilted surface has been modelled in many ways. The simplest approach is with an isotropic model (first developed by Hottel and Woertz [3.37] in 1942 and later improved by Liu and Jordan [3.38] in 1963) which assumes that the diffuse radiation is uniform across the hemisphere. Klucher [3.39] found that the isotropic model performs well under overcast conditions but underestimates the radiation during clear and partly cloudy conditions, such as in the circumsolar region of the sky and when the sun is near the horizon.

The second, more complicated, type of diffuse model is an anisotropic model, in which it is assumed that the diffuse radiation is not uniform across the hemisphere. Many of the anisotropic models take the direct beam and ground reflected components from Liu and Jordan [3.38] and alter the diffuse component. The Klucher model [3.39] from 1979 adds two terms to account for circumsolar radiation and horizon brightening effects and incorporates a modulating function that increases or decreases the weights of these terms based on diffuse-to-total radiation ratio, thereby mimicking partly cloudy conditions.

Other models, like the Hay-Davies model created in 1980 [3.40] add only a circumsolar component of radiation to the isotropic model with the implementation of an anisotropy index, while the Reindl model of 1990 [3.41] builds on the Hay-Davies model by adding an additional term to account for horizon brightening effects [3.42-3.43]. There is also the Muneer model of 1997 [3.44], which treats shaded and sunlit surfaces and overcast and non-overcast conditions separately. More recent work has resulted in a more sophisticated approach by Kocifaj [3.45-3.47], where the heterogeneity of the irradiance field is represented under varying cloud fractions.

For this project, we chose to model the diffuse field with the Klucher model [3.39], based on recommendation by Jakhrani et. al [3.34], which compared several diffuse models and found the Klucher model [3.39] to have the lowest standard error mean. This model is a function of panel tilt, β, solar zenith angle, θ_z, diffuse horizontal irradiance, *DHI*, and global horizontal irradiance, *GHI*:

$$F_{DIF,\beta} = DHI\left(\frac{1+\cos\beta}{2}\right) \times \left[1 + F' \sin^3\left(\frac{\beta}{2}\right)\right] \times (1 + F' \cos^2\theta_i \sin^3\theta_z) \tag{5}$$

$$F' = \left\{1 - \left(\frac{DHI}{GHI}\right)^2\right\} \tag{6}$$

The first term is simply the isotropic diffuse field model described by Liu and Jordan [3.38], the second term represents the horizon brightening effects, and the third term describes the effects of circumsolar radiation. The second and third terms are modulated by a factor F', which is maximized under clear skies and minimized under overcast skies. In other words, when skies are clear, the effects of horizon brightening and circumsolar radiation are greatest; when skies are overcast, those effects are smallest.

The solar zenith angle, θ_z, is a function of the solar elevation angle, α:

$$\theta_z = 90° - \alpha \tag{7}$$

$$\sin\alpha = \sin\phi\sin\delta + \cos\phi\cos\delta\cos\omega \tag{8}$$

Hourly outputs of the solar elevation angle, α, were calculated using the *get_altitude* function from the Python library PySolar, which takes inputs of a location's latitude, longitude, and time-zone aware datetime variable and outputs the solar elevation angle at the specified location and time. Results from this function were compared to direct calculations from equation (8). As the hourly statistics files provide monthly averages of the radiation field, the datetime variable in α was set to the mid-point of each month. For example, α was calculated each hour on June 15th for the month of June.

Finally, the ground reflected irradiance was based on conventions found in Lave and Kleissl [3.19] and Jakhrani et al. 2013 [3.34]:

$$R_g = r_\beta \rho_g GHI \tag{9}$$

where r_β is the reflection coefficient, ρ_g is the ground albedo, and *GHI* is the total global horizontal irradiance. The reflection coefficient, r_β, is a simple function of the panel tilt such that $r_\beta = (1 - \cos\beta)/2$ and we assumed a ground surface albedo of 0.2 as was used in Lave and Kleissl [3.19].

Equations (1)-(9) were combined with the hourly station data from the NSRDB (GHI, DHI, DNI, latitude, longitude, and time zone) to create arrays of incident solar radiation on a theoretical solar panel of every tilt between 0° and 90° in 1° increments for each Class I and Class II station. These hourly totals (when $\alpha > 0$) were summed over the course of the day to create a single array that contained daily integrated sums of the total incident radiation for each angle.

These daily integrated totals of F_{TOT} were summed each month to create an annual F_{TOT} array with every possible angle. Python's *max()* function was employed to find the angle at which the largest annual value of F_{TOT} existed; the optimum tilt angle, β_{opt}. Figure 3.3 depicts the resultant distribution of optimum tilt angles across the US. In general, optimum tilt angles are lower across the eastern half of the country and along the West Coast, which is where cloudiness is generally higher (see Figure 3.4, adapted from [3.33]) and the diffuse field of radiation accounts for a larger portion of the total global horizontal irradiance. As was previously stated, a flat panel is the best way to harvest the diffuse field; thus, it follows that a lower panel angle would be better equipped to handle the larger variance between the direct beam and the diffuse field of radiation.

3.2.2.2 ARRAY-TOTAL RADIATION

The next step was to model the array. Figure 3.5 illustrates two primary inter-row radiation effects as part of a large solar panel array. The rows themselves can have significant effects on the amount of radiation incident on a panel. First, a row can project a shadow on a row behind, thereby reducing the incident radiation on the row behind, and second, a row in front of another row "masks" out part of the diffuse field, also reducing the incident radiation.

We will first deal with the inter-row shadowing problem. To allow for the direct beam of radiation to reach the second, third, and so on rows, sufficient spacing between rows must be accounted for. Smaller shadow lengths are observed in the summer versus winter; a common rule of thumb is to calculate the minimum row spacing required for the panels to be un-shadowed between 10:00 AM and 2:00 PM on the winter solstice [3.48], which is a good compromise between inter-row shadowing and width of rows. Total panel spacing for each row can then be represented as:

$$Panel_{sp} = Panel_g + Panel_{sh} \tag{10}$$

Where $Panel_g$ represents the length of the solar panel projected along the ground (and gets shorter at higher tilt angles) and $Panel_{sh}$ represents the length of the shadow cast behind the solar panel (and gets longer at higher tilt angles). These lengths can be visualized in figure 3.6.

Equations (11), (12), and (13) represent the geometry associated with $Panel_g$ and $Panel_{sh}, where\ Panel_l$ is the length of the PV module and $Panel_h$ is the height of the highest part of the solar panel to the ground (as seen in figure 3.6).

$$Panel_g = Panel_l(\cos\beta) \tag{11}$$

$$Panel_{sh} = \frac{Panel_h}{\tan\alpha} \tag{12}$$

$$Panel_h = Panel_l(\sin\beta) \tag{13}$$

The solar elevation angle, α, was calculated at 10:00 AM on December 21. Combining equations (11)-(13) results in:

$$Panel_{sp} = Panel_l\left(\cos\beta + \frac{\sin\beta}{\tan\alpha}\right) \tag{14}$$

$Panel_{sp}$ was calculated at each station using every optimum tilt angle, β_{opt}, shown in figure 3.3, assuming that the length of the solar panel, $Panel_l$, was 2.0 m, based on the length of an average commercial-use solar panel [3.48-3.49]. Since $Panel_{sp}$ represents the physical space taken up by a single solar panel row, we can multiply that value by any number of rows to create a theoretical solar panel array. For this purpose of this study, $Panel_{sp}$ was multiplied by 100 to represent the amount of one-dimensional ground space that would be needed to house a 100-row solar panel farm at every station location. As both β_{opt} and α varies at each station, $Panel_{sp,100}$ is also different, which is shown in figure 3.7. The "sawtooth" pattern observed is a by-product of time zones. As $Panel_{sh}$ was calculated at 10:00 AM local time, locations close to the time zone boundary essentially saw 1-hour "bumps" in time analysis.

The row spacing algorithm removes most row-to-row shadow effects; however, some shading still occurs, primarily during the winter months and in the very early morning and late evening hours. When a panel is in full shadow, it still receives diffuse radiation but no longer receives direct beam radiation. In terms of actual panel energy output, partial shadowing is a non-linear problem due to the way that PV modules are interconnected. Thin film PV modules are less affected by partial shadowing compared to crystalline PV modules [3.48]. However, for the purpose of this project, we were only interested in the amount of radiation *incident* on a panel surface and not in the amount of energy output *from* a panel. Thus, we treated the shadow effect linearly. For the fraction of panel not in shadow, the amount of radiation was simply as described in equation (1), while for the fraction of panel in shadow, the amount of radiation was equation (1) without the direct beam component.

A method for calculating the amount of panel shaded from a panel in front at different times was adopted from the method in Passias and Källbäck 1984 [3.35]. When the shadow cast behind a panel is greater than the $Panel_{sp}$ calculated in equation (14), a portion of the shadow will be cast on the panel behind, which can be seen in figure 3.5a. The length, L_{sh}, and width, W_{sh}, of the projected shadow is a function of panel tilt, β, the solar declination angle, δ, the solar hour angle, ω, the solar elevation angle, α, the angle of incidence, θ_i, the solar panel length, $Panel_l$, and the solar panel width, $Panel_w$, and the panel row spacing parameter, $Panel_{sp}$.

$$L_{sh} = Panel_l - \left(\frac{\sin\alpha}{\cos\theta_i}\right) Panel_{sp} \tag{15}$$

$$W_{sh} = Panel_w - \left(\frac{\sin\beta\cos\delta\sin\omega}{\cos\theta_i}\right) Panel_{sp} \tag{16}$$

The next problem is the "masking" effect (see figure 3.5b), in which all rows behind the first row do not see the entire "hemispheric" view of diffuse radiation [3.35]. The amount that the incident diffuse radiation is reduced depends on row spacing (closer rows result in a reduced incident diffuse radiation), panel length, panel tilt, and sun angle. Passias and Källbäck 1984 [3.35] came up with a relatively simple model that represents the reduction in the diffuse field relative to an average masking angle, $\bar{\psi}$.

$$F_{DIF,\psi} = 1 - \cos^2\left(\frac{\bar{\psi}}{2}\right) \tag{17}$$

Where $\bar{\psi}$ can be evaluated as:

(18)

$$\bar{\psi} = \sin\beta \frac{Panel_{sp}}{Panel_l}\left[\tan\beta \tan^{-1} a + \ln(1+b) - \frac{1}{2}\ln\{1+b^2\} - \frac{\tan^{-1} a}{\sin\beta\cos\beta\,(1+b)}\right]$$

and

$$a = \frac{Panel_l \sin\beta}{Panel_{sp} - Panel_l \cos\beta} \tag{19}$$

$$b = \frac{Panel_l \cos\beta}{Panel_{sp} - Panel_l \cos\beta} \tag{20}$$

The panel inter-row shadowing [equations (10)-(16)] and inter-row masking [equations (17)-(20)] algorithms were applied to all rows except for the first row. The summation of incident radiation for a 100-row array with all panels tilted at the optimum tilt angle, β_{opt}, was adjusted for shadowing and masking losses throughout the year to result in an annual array-wide $F_{TOT,\beta_{opt},array}$ value.

3.2.2.3. APPLYING THE DASH METHOD

The same method in 3.2.2.2 as applied to the single optimum tilt angle, β_{opt}, was applied to all angles (0º to 90º) at every station. To model the theoretical incident energy across a dual-angle array, the number of rows, N, of panels tilted at β_1 and β_2 had to be solved for, which is simply a function of the fraction of panels to be tilted at β_1 and the panel spacing of β_1, β_2, and β_{opt}.

$$N_2 = 100 \frac{Panel_{sp,\beta_{opt}}}{\left(Panel_{sp,\beta_1}\left[\frac{fract_1}{(1-fract_1)}\right]\right) + Panel_{sp,\beta_2}} \tag{21}$$

$$N_1 = N_2 \left[\frac{fract_1}{(1-fract_1)}\right] \tag{22}$$

Certain constraints were placed on the above set of equations. First, β_1 and β_2 had to be at least 5° apart. Second, the minimum spacing between rows was set to 1.0 meters. This was done to more closely simulate an actual solar panel farm, in which enough spacing between rows must exist for maintenance work to be done. If this hadn't been set, flat panels would be modeled with no space between them. Third, N_1 and N_2, or the number of panel rows tilted at β_1 and β_2, could only be whole numbers. After the above equations were used, if there was a remainder large enough to fit an additional panel row, an extra row was added. Figure 8 displays a cartoon (not to scale) showing how a dual-angle system is able to fit more panel rows compared to an array of panels all tilted at the single optimum tilt angle.

All combinations of angles were tested using various $fract_1$ values. The best dual-angle array was one that not only resulted in an overall gain in harvested solar energy per unit space, but one that also accomplished this using the fewest number of extra rows possible, thereby curbing costs. Higher unit energy gains could be realized by adding even more rows at lower (or sometimes higher angles), but at a certain point, the energy harvest per solar panel degrades rapidly compared to the energy harvest of a panel at β_{opt}. The annual incident solar radiation with respect to every panel tilt angle can be visualized by a parabolic concave downward curve, where the peak of the curve is the β_{opt} angle. Thus, angles close to β_{opt} see little change in incident solar radiation, while angles further away from β_{opt} start to see significant decreases in incident solar radiation. The rapid degradation in incident energy is due to an increase in the angle-of-incidence, θ_i, between the panel and the direct beam at hours when the sun is strongest [recall that $F_{DIR,\beta} = DNI\ (\cos\theta_i)$ where $\cos\theta_i$ gets smaller as θ_i gets larger], and can also be due to stronger effects from inter-row shadowing and the masking of the diffuse field, $\bar{\psi}$, , particularly when the panel is tilted higher than β_{opt}.

The total annual array-wide incident energy at angle β can be represented by:

$$F_{TOT,DUAL} = F_{TOT1,first\ row} + (N_1 - 1)\ F_{TOT1,other\ rows} + (N_2\ F_{TOT2,other\ rows}) \tag{23}$$

Where $F_{TOT1,first\ row}$ is the incident energy on a single panel tilted at β_1 without any inter-row shadowing or masking effects and $F_{TOT1,other\ rows}$ and $F_{TOT2,other\ rows}$ are the incident energy on a panel tilted at β_1 and β_2, respectively, that take into account the inter-row shadowing and masking effects. Python was used to solve for the model output that resulted in an X% array-wide energy gain with the least number of extra panels, or N_{extra}, where N_{extra} is simply:

$$N_{extra} = (N_1 + N_2) - 100 \tag{24}$$

The results of the model are discussed in section 3.3.

3.3. RESULTS AND DISCUSSION

In section 3.3.1, we apply the DASH method to two selected test locations which exhibit diverse geographic and climate characteristics and explore all model solutions. In section 3.3.2, we apply the DASH method nationally, keeping one angle equal to the optimum tilt angle, β_{opt}, and discuss the results related to the best performance of the DASH method.

3.3.1 Testing the DASH Model at Two Ideal Locations

Two geographic and climate diverse Class I NSRDB locations were chosen to further test the DASH method. Our test locations were required to have the highest quality data, hence the Class I distinction, and needed to represent a range of cloud cover and geographic distinctions. The locations selected were Barstow, CA and Akron, OH, which differ greatly in annual cloud cover and latitude, but still manage to have similar single optimum tilt angles, β_{opt}, of 30° and 28°, respectively. Characteristics of both locations are displayed in Table 3.1. Even though the higher latitude of Akron (40.92°N) would suggest a higher β_{opt} than Barstow, Akron's annual cloud fraction of 6.7 tenths (ranging from 7.8 in the winter to 5.6 in the summer) implies a larger diffuse component, which is better harvested by a flatter angle. Meanwhile, Barstow's sunny climate with an annual cloud fraction of 2.5 tenths (ranging from 4.0 in the winter to 1.4 in the summer), resulted in a β_{opt} much closer to the latitude angle of 34.85°N. The results of the DASH method at each location for various array-wide energy gains when $fract_1 = 0.30$ is also displayed in Table 3.1.

Figures 3.9-3.12 illustrate the range of solutions for every possible dual angle combination between 0º and 90º (in 1º increments) for Barstow, CA (Figures 3.9, 3.10) and for Akron, OH (Figures 3.11, 3.12) using the 0.30 fractional split between β_1 and β_2 (i.e. 30% of the rows are arranged at β_1 and 70% of the rows are arranged at β_2). Figures 3.9 and 3.11 display the percent gain in F_{TOT} across the entire array for each dual angle combination, while figures 3.10 and 3.12 display the number of extra panel rows that fit into the footprint of a 100-row solar array when all panels are tilted at the single optimum tilt angle. The best dual angle solution for a tested gain in array wide F_{TOT} is when the number of extra panel rows is lowest.

Both locations observe a gain in array-wide incident solar energy when the higher fraction of panel rows (β_2) are tilted near or lower than the optimum tilt angle (red shading to the left of the vertical black dashed line representing β_{opt} in figures 3.9 and 3.11). This makes sense as panels with lower tilt angles can be spaced closer together. Meanwhile, the tilt of the remaining panels (β_1) can be higher or lower than the optimum tilt angle to see an array-wide gain (shown by the red shading both above and below the horizontal dashed black line representing β_{opt}. Higher gains are observed when β_1 is also lower than the optimum tilt angle, but the number of extra panel rows is much higher.

Even though both locations have nearly the same optimum tilt angle, Akron has the potential for higher array-wide energy gains simply because the size of the 100-row optimum tilt array is larger due to longer shadow lengths on the winter solstice observed at a higher latitude. This implies that a location at a higher latitude has more to gain by implementing the DASH method compared to a location at a lower latitude. It also suggests that the common rule of thumb of spacing panels according to the winter solstice sun angle is more appropriate for lower latitudes than higher latitudes, as this method results in array sizes that are double, triple, or even larger than an array using a similar panel tilt much further south. For an array at a higher latitude to have similar row spacing as an array at a lower latitude, a lower tilt angle must be employed.

3.3.2 Applying the DASH Model on a National Scale

In this section, we apply the DASH method to all 858 Class I and Class II stations from the NSRDB. From section 3.3.1, it became apparent that there are multiple solutions for the DASH method that are very similar. In other words, similar gains in incident array-wide solar energy can be attained from multiple pairs of angles at different fractions.

As it would be impossible to show every viable solution for each station, we chose to add one additional constraint to the problem. We kept β_1 equal to the optimum tilt angle, β_{opt}. By doing this, we were able to explore how (usually) small changes in tilt angle applied to a fraction of the single optimum tilt angle array could result in significant gains in array-wide incident solar energy per unit space.

For example, a panel tilted at the optimum tilt angle of 28° in Akron, OH requires a panel spacing of 4.74 m; however, a panel tilted just 5° lower requires a panel spacing of 4.31 m. Nearly 10 extra panel rows (an increase of 10%) at this lower tilt angle can fit into the footprint of the 100-row β_{opt} solar array (seen in figure 3.6).

Figure 3.13 illustrates the profound effect that a 5° reduction in tilt angle (compared to β_{opt}) can have across the entire United States. From a spatial perspective, more panel rows can fit at higher latitudes than lower latitudes, which is simply due to the lower sun angle and longer inter-row shadow length on the winter solstice. While nearly 10 extra rows can fit in Akron, OH, 6 extra rows can fit in Barstow, CA.

Setting β_1 equal to β_{opt}, the DASH method model was run for every station across the United States, testing all fractional arrangements of panels tilted at β_1 (i.e. β_{opt}) between 0.2 and 0.8 in 0.05 increments. The "best" solution of the DASH method was one that resulted in both the fewest number of extra panel rows and the lowest fraction of panels tilted at β_2 for a given percent gain of incident array-wide solar energy. In other words, what was the solution where the greatest number of rows could remain at β_{opt} while still resulting in a particular gain of energy?

Figure 3.14 depicts the fraction of panels that had to be lowered from β_{opt} to reflect a 10% gain (figure 3.14a) and a 20% gain (figure 14b) in incident solar energy across the array, while figure 3.15 displays the necessary tilt angle of β_2 to produce the 10% (figure 3.15a) and 20% (figure 3.15b) gains in array-wide energy. Blank regions of the map indicate places where no fraction of panels at any angle of β_2 could yield the tested percent gain in energy. This doesn't necessarily mean that no solution of the DASH method exists, but it implies that the DASH method does not work with the optimum tilt angle, β_{opt}. A solution that probably works is one with both panel angles oriented lower than β_{opt}.

For the 10% gain in array-wide incident solar energy, at least 11 extra panel rows are required nationally; for the 20% gain, this increases to at least 21-24 rows. In general, the DASH method performs better (i.e. places where the lowest percentage of rows are required to change from β_{opt}) across the higher latitudes than the lower latitudes. This is likely because of the "latitude effect" with higher β_{opt} panel tilt angles (figure 3.3) and wider panel spacing observed in these locations (figure 3.7), thereby making it "easier" for lower panel tilts to fit into the array.

In Akron, OH, only 35% of the panel rows have to be adjusted from β_{opt} to observe a 10% gain in array-wide incident solar energy, compared to a much larger 70% in Barstow, CA. In other words, much less change to a "typical" array is required in Akron compared to Barstow. For a 20% gain, 55% of the panel rows must be adjusted in Akron, while no solution with β_{opt} is feasible in Barstow.

Perhaps the "best" performance of the DASH method is observed in some of the cloudiest regions of the country (figure 3.4), such as centered over the Great Lakes and along the coastal Pacific Northwest. These locations have locally lower β_{opt} angles (figure 3) so it is not merely a result of higher panel tilts and longer panel spacing associated with β_{opt} that results in smaller fractions of panels at β_2. Rather, the higher cloud fraction at these locations implies a more dominant diffuse field (see figure 3.16), which would be able to support lower tilt angles with less reduction in incident solar energy. Figure 3.15 confirms that these same locations have some of lowest recommended β_2 angles, which are able to be spaced closer together than higher angles (also resulting in more rows remaining at β_{opt}).

Of note, the spatial pattern observed in figure 3.14a is actually similar to the distribution of annual cloud fraction (figure 3.4); where cloud fraction is higher, more panel rows are able to remain oriented at β_{opt}; where cloud fraction is lower, less panel rows remain oriented at β_{opt}. This further suggests that regions with a more dominant diffuse field (i.e. cloudier locations) are better suited for implementation of the DASH method.

A dual-angle arrangement on a large solar array could be particularly useful in partly cloudy climates. On more overcast days, the lower panels would more efficiently harvest solar radiation, on sunnier days, the higher panels would more efficiently harvest solar radiation, and on days of variable cloud cover, such as skies filled with fair weather cumulus clouds, the combination of two angles could produce better handling of a highly varied solar radiation field. On days of fair-weather cumulus, there can be many short intervals of direct sun (when no cloud is obscuring the sun disk) and covered sun (when a cloud is obscuring the sun disk). In other words, the solar radiation field varies between mostly direct and mostly diffuse. The varied angles could perhaps capture this radiation field more efficiently and reduce minute-to-minute variability in power generation. Future work could help quantify this hypothesis.

3.4. CONCLUSIONS

Decreasing costs of solar panels paired with rising costs of land are making it imperative to not only consider the amount of energy harvested per unit solar panel, but to also consider the amount of harvested energy within a unit area.

In this study, we suggest an alternative approach of organizing large solar panel arrays that considers this co-optimization problem and introduces a new dual-angle technique, called the dual-angle solar harvest (DASH) method, in which a solar array is composed of panels tilted at two different angles instead of one optimized tilt angle. While no pair of angles can ever beat the single optimum tilt angle panel per panel, our study suggests that implementation of the DASH method could result in significant gains of harvested solar energy per unit area compared to an array of all panels arranged at the single optimum tilt angle.

We first present a phase space for two climatically and geographically different locations (Akron, OH and Barstow, CA) that show the resultant gain in array-wide energy and the number of extra panel rows required for all combinations of pairs of angles for two different fractional distributions of rows using this technique.

Applications and uses of the DASH method are many; this paper explores one solution of the DASH method nationwide in which one of the two angles is kept constrained at the optimum tilt angle. We show results for the best dual-angle solution that results in both a 10% and a 20% gain of incident solar energy, which is the solution where the fewest number of panel rows must be oriented at a different tilt angle to attain the desired energy gain. In other words, how can the smallest change to an array produce a desired energy gain? We show that only 35% of the panels must be adjusted from the β_{opt} angle in Akron, OH to observe a 10% gain, while double the amount of panels (70%) must be adjusted in Barstow, CA to observe this same gain using β_{opt}. Meanwhile, for a 20% gain, 55% of the panel rows must be adjusted in Akron, while no solution with β_{opt} is feasible in Barstow.

The best performance using the DASH method occurs across the Pacific Northwest and the Great Lakes, where conditions are cloudier and where the diffuse component of radiation accounts for a significant portion of the total radiation field. Certainly, these variables co-vary to a degree, but the diffuse-to-total radiation ratio also encompasses other quantities that scatter or reflect the direct beam, such as air pollution, smoke, high values of relative humidity (i.e. an increase of water vapor throughout the column, which swells aerosol particles and absorbs solar radiation), and sea salt. It is proposed that a dual-angle approach to harvesting solar energy can be better tuned to the local radiation field, and the lower angle allows panel rows to be spaced more closely together, thereby increasing harvested energy within a unit area.

This study may be viewed philosophically as a next iteration in optimized panel geometry as both panel tilts and the physical footprints of a panel array are co-optimized. Further, the implementation of dual angles carries the added benefit that an array can be better tuned for varying cloud conditions. Lastly, this study strongly suggests that specially shaped solar panels (i.e. not flat) may be capable of even more impressive harvest efficiency gains.

Chapter 4:

Rutgers' Solar Array Performance: Effect of Orientation and the Local Diffuse/Direct Insolation Balance

4.1. INTRODUCTION

The deployment of new solar panel installations has seen rapid growth over the past decade [4.1, 4.2]. This rapid growth can be attributed to both plummeting costs in the manufacturing process [4.3] as well as government incentive programs, such as the Solar Investment Tax Credit (ITC) first introduced in 2005 [4.4, 4.5]. Many institutions and companies are now turning towards Photovoltaics (PV) as an alternative source of energy.

In urban areas, where open land is both limited and more expensive compared to rural areas [4.6], space-saving PV installations are sought out. One space-saving installment practice has been the implementation of solar parking-lot canopy systems. Not only do solar parking-lot canopies provide shade [4.7, 4.8] while also serving as a source of energy, but they can also greatly reduce the maximum pavement surface temperature, thereby curtailing some of the urban heat island effect [4.7]. Furthermore, a 2010 case study in Tippecanoe County, Indiana found that more than 6.5% of the county's urban land was consumed by parking lots [4.9]. Assuming similar proportions elsewhere, this suggests an abundance of possible locations that could be suitable for solar carport canopy systems.

The Rutgers solar parking canopy system, completed in March 2014, is a large and visible landmark for students and faculty alike, encompassing a footprint of approximately 32 acres [4.10]. The power generation and utilization, however, are not adequately quantified or understood by the general Rutgers community. In this study, we combined a number of data sources to help understand more about how solar array power generation depends on weather conditions, and how these weather conditions impact sunlight intensity in either “direct” illumination mode or by capturing “diffuse” light that might have been scattered by clouds in many ways.

The seasonal and time-varying recent electrical output performance of the Rutgers solar parking-lot canopy array is analyzed in comparison with a nearby meteorological weather station operated by Rutgers and longer range standardized historical solar data provided by the US Department of Energy’s National Renewable Energy Laboratory (NREL). The comparisons take into account the physical installation details of the canopies (tilt and azimuth orientation) and examine time-of-day output variations and the influences of extent of cloud cover and the importance of the contribution of diffuse light on the array output.

Our comparison here allows the rigorous measurement of diffuse and direct sunlight intensity parameters and their application to understanding real electrical output from a major physical installation. The following sections address the physical installation as well as the data analysis that we have performed on the existing weather station and electrical output responses.

4.2. DATA

Three important sources of data have been gathered and compared to gain insight about sunlight variability and its impact on seasonal and daily solar array output, as described in the following sections.

4.2.1. Solar Carport Canopies

The Rutgers University, Livingston Campus Solar Carport Canopy System is an 8 MW DC solar PV canopy system built over three large parking areas in Piscataway, New Jersey: the Yellow Lot and the Green Lot (located at 40°31'35.3"N 74°26'20.4"W, and referred to as only the Yellow Lot for the remainder of this paper) and Lot 105 (located at 40°31'29.6"N 74°26'03.8"W) [4.11]. Each canopy is split equally into a portion that is tilted 15° relative to the horizon and a portion that is flat (see Figure 4.1); the cardinal orientations of the canopies, however, differ between the two locations, with the canopies at the Yellow Lot oriented 126° ESE and the canopies at Lot 105 oriented approximately perpendicularly (216° SSW) (see Figure 4.2). These canopies support a total of 30,242 modules, each rated at 265 Watts-DC. Taken together these canopies cover 32 acres of parking lot and provide shade for approximately 4,000 parking spaces. The output from the PV canopies is broken into 14 regions for electrical conversion by 500KW Solaron inverters 10 of which are connected to the Yellow Lot and 4 of which convert the power from Lot 105 [4.12]. Individual inverter power output observations have been logged every 15 minutes and stored remotely as part of the verification protocol enabling the collection of SREC (Solar Renewable Energy Certificates) provided by the state. For the present study we have retrieved inverter-level data from January 2016 to April 2019 for comparison with the same time period of weather station data (see section 4.2.2 below).

As the inverters occasionally go offline for maintenance or due to other problems, we calculated the mean of the 10 inverters from the Yellow Lot and the mean of all 4 inverters from Lot 105 for each 15-minute interval, ignoring any data gaps. This resulted in one continuous time series of inverter data for each parking lot covering the 3+ year period.

4.2.2 Rutgers' PAM Site

The Rutgers Photochemical Assessment Monitoring (PAM) Site is located approximately 7 km south of the solar arrays on the Rutgers Livingston Campus (located at 40°46'22.65"N 74°42'94.37"W). A full suite of broadband and narrowband solar radiation measurements has been collected continuously for the past three years (starting in April 2016). Broadband solar irradiance in the wavelength range 200-3600 nm are measured using a Kipp and Zonen solar tracking system every second. The total radiation field (direct plus diffuse) is measured using a Kipp and Zonen CMP-22, which is an ISO 9060:2018 spectrally flat class A pyranometer with a directional irradiance error below 5 W/m² and a temperature sensitivity of <0.5%. The diffuse radiation field is measured using a shaded Kipp and Zonen CMP-21, which is an ISO 9060:2018 spectrally flat class A pyranometer with a directional irradiance error below 10 W/m² and a temperature sensitivity of <1%.

Diffuse irradiance from July-August 2016 was not available from the Kipp and Zonen system due to a maintenance issue, so backup measurements were supplied by a Dynamax Delta-T model SPN-1. The SPN-1 measures irradiance in the 400-2700 nm wavelength range with a temperature sensitivity of <1%. Unlike the primary Kipp and

Zonen tracking system, the SPN-1 uses multiple detectors and an internal occulting dome that insures that at least one of the detectors is always shadowed and at least one is not.

The PAM Site also houses a BloomSky instrument, which not only captures a photograph of the sky every 4-6 minutes, but also records temperature, humidity, and air pressure. The BloomSky was primarily used to confirm types of clouds or sky conditions on selected days as shown below in Figure 4.3.

Irradiation data from April 2016 to July 2019 were downloaded from the site. Data output included 1-minute observations of global horizontal irradiance (GHI), or the total radiation field incident on a locally horizontal plane, and diffuse horizontal irradiance (DHI), which provides only the diffuse field by blocking the direct sun illumination. The direct normal irradiance (DNI) wasn't measured by our system directly. Between May 9, 2018 and June 20, 2018, the primary Kipp and Zonen solar tracking system was out for calibration. During this period, data from the backup pyranometers were used.

4.2.3. US DOE/NREL Typical Meteorological Year

The actual measurements of electricity and sunlight above were referenced to standardized sunlight variability data provide by the US Department of Energy (DOE) through the National Renewable Energy Laboratory (NREL). These "Typical Meteorological Year" data sets [4.13] provide full 365 day sets each containing hour-level granularity for a variety of weather-related parameters, including GHI, DHI, and DNI (as defined above), as well as temperature, rainfall, humidity and other parameters. Throughout the US there are over 1000 available TMY3 locations of which the closest to our campus array is the dataset for Newark, NJ. The TMY datasets have been assembled by NREL using historical measurements over time and are built to represent typical ranges of variability of cloud cover and lighting levels and were used here to provide a standardized baseline to compare with the actual light levels measured above.

The TMY data were augmented with a sun-position algorithm [4.14] to allow us to calculate the effective insolation for the tilted canopy segments for all times of day throughout the year – essentially calculating the angle, Θ, between the panel's normal vector and the instantaneous location of the sun. $DNI * \cos(\Theta)$ is then the direct illumination component for an arbitrarily tilted and aligned array. It should be noted that NREL has built a popular user interface called PVWATTS 2.0 [4.15] where solar engineers can make solar array output estimates for tilted panels based on calculations also using the TMY3 data, though the hourly granularity is lost when using that software.

4.3. METHODS

The above data sources were processed to make interesting observations on the electrical output variations and differences between the two solar canopy arrays over the three-year period. Of most critical value was knowing the important role that cloud cover plays in scattering light from the direct ray into diffuse brightness, given that the solar panels capture both types of light. In this section we describe our method of categorizing cloud cover types and then separately examining solar array output variations under those specific types of conditions. This section goes into detail about how those categories were chosen and relevant comparisons are provided.

4.3.1. Sky Cloud Cover Assessment Based on PAM Site Data

The 1-minute irradiance data from the PAM Site was used to diagnose three different types of days: clear, variable, and cloudy. Not all days could easily fit into one of these three bins; some days were left unclassified as they were deemed too complicated. For example, a day that started off with clear skies in the morning, transitioned completely overcast in the afternoon, and ended with some partial clearing in the evening could be very difficult to fit into one classification.

To help simplify this problem, our sky cover algorithm was broken into two steps. The first step involved diagnosing 15-minute periods of sky conditions, while the second step combined these 15-minute classifications to find the single best daily classification, if possible.

4.3.1.1. 15-MINUTE SKY COVER ALGORITHM

First, observed 1-minute GHI and DHI data from the PAM Site were down sampled to 15-minute means and the variance was calculated using Python's *numpy.var( )* function. Monthly averages of the same quantities were also calculated, which were used to determine ratios of the GHI and DHI for each time frame, as shown in equations 1-3,

$$GHI_{var,ratio} = \frac{GHI_{var,15-min}}{GHI_{var,avg}} \tag{1}$$

$$GHI_{ratio} = \frac{GHI_{15-min}}{GHI_{avg}} \tag{2}$$

$$DHI_{ratio} = \frac{DHI_{15-min}}{DHI_{avg}} \tag{3}$$

Where the subscript *15-min* corresponds to the down sampled 15-minute observations of GHI and DHI, *var* corresponds to 15-minute variance, and *avg* corresponds to the monthly mean for each 15-minute window.

Simply put, these ratios represent how far from the normal each 15-minute observation was and were used to determine sky cover conditions. To gain a better understanding of the normal irradiance profile for distinct types of sky cover conditions, ideal cases of clear sky days, overcast days, and partly cloudy, or variable, days were chosen. Daily time-lapses of sky conditions from the BloomSky instrument were used to help select these model days. There are two primary types of variable cloudy days that our algorithm accounts for: the first is a day that is characterized by fair-weather cumulus cloud development (usually in the afternoon), and the second is a day that is almost entirely characterized by broken clouds, which can include but is not limited to a combination of periods of thicker clouds, periods of thinner clouds, and periods of clear sky conditions.

Figure 4.3 shows an example of an ideal clear sky day, an ideal variable cloudy day, and an ideal overcast day. The first row shows a screenshot from the BloomSky instrument around mid-day, the second row displays the observed profiles of 15-minute mean GHI and DHI along with the monthly averages of these values, and the third row displays the observed profiles of 15-minute variance of GHI and DHI in conjunction with their monthly averages. The distances between the observed profiles and the monthly averages are visual representations of equations 1-3 and were used to help visualize how far from the normal each day was during the creation of the sky cover algorithm.

From these ideal examples, there are several patterns with regards to the irradiance profiles and the variance profiles that become obvious. These patterns are useful in determining sky cover conditions for all days.

For the purpose of this study, the calculated variance is a measure of how the GHI or DHI changes within the 15-minute time frame. When variance is low, sky conditions are homogenous. In other words, the values of GHI and DHI do not change much within the 15-minute window. This can either describe clear sky conditions or completely overcast conditions. On the contrary, when variance is high, sky conditions are heterogenous. A simple example of this is a sky filled with small fair-weather cumulus clouds; the amount of ground reaching direct irradiance varies largely each time a small cloud passes over the sun disk, which can easily occur within the 15-minute window. Thus, higher variance is indicative of more variable cloud cover.

During clear sky conditions, the observed GHI is either near or higher than the monthly average, while the observed DHI is generally less than the average (Figure 3d). Meanwhile, the observed variance, particularly removed in time from the sunrise and sunset hours, is much lower than the average (Figure 4.3g).

During cloudy conditions, the observed GHI is much lower than the monthly average, while the observed DHI is generally near or greater than average

(Figure 4.3f). Meanwhile, the observed variance is still quite a bit lower than the average but does tend to feature values higher than clear sky conditions (Figure 4.3i).

The primary distinction between clear or overcast sky conditions and variable sky conditions is the variance. When variable sky conditions exist, the variance is often at or much higher than the monthly average (Figure 4.3h). On a day where fair-weather cumulus clouds develop in the afternoon, as is the case on the example shown in Figure 3b, the observed GHI profile compared to the monthly mean is similar to what is seen on a clear sky day, with the difference being that GHI can sometimes be higher than what is possible on a clear sky day (think a fully exposed sun disk with added radiation being reflected from a nearby cloud), and it can also sometimes be lower than what is possible on a clear sky day (such as when a scattered cloud passes directly over the visible sun disk) (Figure 4.3e).

Relationships 4-8 were used to classify each 15-minute period of data:

$$\boldsymbol{Cloudy} = (GHI_{var,ratio} < 1)\ \&\ (GHI_{ratio} < 1) \tag{4}$$

$$\boldsymbol{Variable} = (GHI_{var,ratio} \geq 1)\ \&\ (GHI_{ratio} \geq 0.5) \tag{5}$$

$$\boldsymbol{Variable} = (GHI_{var,ratio} < 1)\ \&\ (GHI_{ratio} \geq 1) \tag{6}$$

$$\boldsymbol{Clear} = (GHI_{var,ratio} \leq 0.1)\ \&\ (GHI_{ratio} \geq 1) \tag{7}$$

$$\boldsymbol{Clear} = (GHI_{var,ratio} < 1)\ \&\ (GHI_{ratio} \geq 1)\ \& \tag{8}$$

$$(DHI_{ratio} \leq 0.1)$$

The order in which the relationships are applied matter and they should be applied in the order listed above. There are some data gaps in the above relationships. In other words, some of the 15-minute periods were not classified using this algorithm and values were set to NaNs. However, as the ultimate goal was to try to assign one of three daily sky cover classifications, these "empty" time frames were simply ignored during step two of the classification algorithm.

In total, there were 81,586 15-minute periods between sunrise and sunset. Of these, 53,512 were classified into one of the five bins described above, which represents more than 65% of the dataset. The remaining ~35% of the dataset was more complicated than the above relationships. There is no one single method to accurately bin or classify each 15-minute period of irradiance data into just one of five sky condition categories. The relationships between the ratios of GHI and DHI as well as the variance of GHI can be tuned in different ways. Clouds are far more complicated than the relationships listed in this paper, but for the purpose of this study, we were interested in a dataset that had a distinct separation between clear skies, cloudy skies, and variable skies.

The top row of Figure 4.4 displays the output of our sky cover algorithm for the same days in Figure 4.3. Each black dot represents the sky cover classification for each 15-minute period. It is particularly apparent on the clear sky day that the sky cover algorithm struggles in the early morning and late evening hours. It is a well-known problem that it is exceedingly difficult to classify sky conditions when the sun is near the horizon (i.e. near sunrise and sunset) [4.16, 4.17]. Excess scattering and reflection of aerosols near the horizon, when the sunlight has to travel through the largest slice of atmosphere, as well as objects obscuring part of the sun can often lead to algorithms indicating some form of cloudiness even if skies are clear. For this reason, we first removed data both an hour after sunrise and an hour prior to sunset in all subsequent analysis.

The middle and bottom rows of Figure 4.4 describe the percentage of 15-minute observations per month (Figure 4.4d, 4.4e, 4.4f) and per hour (Figure 4.4g, 4.4h, 4.4i) that fell into each classification. In general, variable cloudiness peaks in the afternoon and during the summer months (due to seasonally higher summertime convection [4.18, 4.19, 4.20]), while more widespread cloudiness peaks in the morning/evening hours and during the winter (related to synoptic scale storm systems [4.20]).

4.3.1.2. DAILY SKY COVER ALGORITHM

The second step of the sky cover algorithm was designating the dominant cloud type for each day. First, the number of 15-minute classifications that fell into each of the five bins was counted. The sky cover classification that featured the highest count each day was designated as the dominant sky cover classification. An exception was made with respect to variable days. As was shown in Figure 4.3e and Figure 4.4b., an ideal example of a variable cloudiness day was not always one that featured a majority of 15-minute observations of variable conditions. To take into account days with optimal fair-weather cumulus development in the afternoon, a day was re-classified as variable if the number of 15-minute periods classified as variable met or exceeded 14 (greater than 3.5 hours) and the number of 15-minute periods classified as cloudy did not exceed 14 (less than 3.5 hours).

Based on the cut-off values noted above, a total of 465 days were classified as cloudy, 459 days were classified as variable, and 236 days were classified as clear, resulting in a total of 1,160 days or 3.18 years' worth of classified data. These classifications of the type of cloud cover were then used to sample the solar array output data, as described in more detail in Section 4.4.

4.3.2. Sky Cloud Cover Assessment based on TMY3 data

Similar to the above analysis using our on-site, real-time meteorological information, we have analyzed NREL's TMY3 data to categorize those standard days into the same three categories. This is hampered to some degree because the TMY3 data are only reported at hourly intervals rather than the minute-by-minute data afforded by the PAM Site. Still, there are key differences in the GHI and DHI values in the TMY3 hourly datasets that allow us to similarly categorize each day. As suggested by the middle row of Figure 3 above, a key difference in categorizing clear and cloudy days is the ratio between the GHI and DHI: under circumstances of very cloudy skies there will be little difference between the GHI and DHI because very little direct sunlight is reaching the solar panel. On the other hand, under very clear sky circumstances, most of the light will be directly illuminating the solar panels and will largely outpace the DHI contribution; and these differences will change through the day (as above) where the AM might be very clear, but the PM might be dominated by heavy cloud cover. So, when viewing the hour-level data from TMY3 data we have taken a strategy of fitting the hour-by-hour GHI data for each day against an ideal parabolic shape, and similarly fitting the hour-by-hour DHI data for each day with a different parabolic shape (but both pegged to that day's sunrise and sunset times). The measured GHI and DHI data can then be compared to categorize each day. If diffuse light is dominant, the DHI/GHI ratio will be close to 1.0. Similarly, on a very clear day we expect the diffuse light to be weak in comparison to GHI. The "variable" days will be in-between. Using the fitted DHI/GHI ratio as a metric we used cutoff values of

$$\boldsymbol{Cloudy}: \quad (DHI_{peak}/GHI_{peak}) \geq 0.60 \tag{9}$$

$$\boldsymbol{Variable}: \quad (DHI_{peak}/GHI_{peak}) < 0.60 \ \ \& \ \ (DHI_{peak}/GHI_{peak}) \geq 0.30 \tag{10}$$

$$\boldsymbol{Clear}: \quad (DHI_{peak}/GHI_{peak}) < 0.30 \tag{11}$$

The 0.60 and 0.30 cutoff values have been chosen to be consistent with the groupings selected using the PAM Site data, above. Using these cutoff values, there were 134 cloudy days, 78 clear days, and 153 variable ones. These classifications of the type of cloud cover were then used to provide a more standardized comparison basis for expected solar array output, as described in more detail in Section 4.4.

4.4. RESULTS AND DISCUSSION

Three types of sunlight data are now processed and compared, subject to the categorization by extent of cloud cover: (1) our PAM Site calibrated measurements, (2) the Rutgers Solar Array metered power output, and (3) NREL's standard typical meteorological year data.

4.4.1. PAM Site Insolation Data

The cloud-cover categorization methods established above in section 4.3.1 were applied to the GHI and DHI data and daily integrations were calculated. Figures 4.5 and 4.6 display the breakdown of daily integrated GHI and DHI observations from the PAM Site colored by each day's dominant sky cover classification. Clear days are colored in green, cloudy days are colored in orange, and variable days are colored in blue. Each dot is scaled in size to represent the number of 15-minute time intervals that were classified with variable conditions. The larger the dot, the greater the number of observations of variable cloudiness conditions. The seasonal component of radiation is easily seen by the peak in magnitude during the summer months. There is also the obvious distinction between clear days and cloudy days. When looking at GHI (Figure 4.5), or the total radiation field, clear days have much higher values than cloudy days, as would be expected. Meanwhile, when looking at the diffuse field, or DHI (Figure 4.6), cloudy days have higher values than clear days because of the increased scattering from clouds.

There is also a relatively wide monthly distribution of GHI and DHI. The lowest values of GHI on cloudy days are those that have the lowest number of variable observations (smaller dot size). This conforms to the understanding that the cloudy days with the lowest values of ground-reaching irradiance have the thickest and most unbroken cloud fields, while the cloudy days with higher values have more periods of thinner or broken clouds, allowing more radiation to reach the ground. The opposite is true for clear days. The highest values of GHI on clear days are those that have the lowest number of variable observations. Again, this makes sense as this matches with situations that have the fewest clouds and have higher GHI than days with some scattered clouds (more variable observations).

The most interesting category is the variable days. This is also the category with the widest monthly irradiance distribution. In terms of GHI (Figure 4.5), daily values range from the upper tier of cloudy days to sometimes surpassing the maximum irradiance observed on a clear day. The variable days that surpass the daily irradiance observed on a clear day occur from spring to early fall. This implies a convective component to the cloud, which likely means that those days are characterized by clear-sky cumulus cloud development in the afternoon as periods of unobscured sun paired with the radiation scattered in from nearby clouds could result in inflated values of ground-reaching GHI. This effect can more clearly be seen in the plot of DHI (Figure 4.6), in which daily values of DHI often meet or exceed the DHI observed on cloudy days. Further, the range of DHI for variable days closely matches the range of DHI observed on cloudy days.

In summary, variable days often exhibit similar amounts of diffuse radiation as cloudy days, but with much higher totals of total radiation. Since nearly 80% of the PAM Site dataset was classified as either cloudy or variable (compared to just 20% classified as clear), this suggests that the diffuse field of radiation is very important with regards to harvesting solar energy in photovoltaic arrays.

4.4.2. Solar Canopy Electrical Output Data

Hourly averaged inverter output from the solar canopy was summed daily and matched to the known cloud cover condition established above. These daily integrated inverter energy output totals is displayed in Figure 4.7 and plotted the same way as Figures 5 and 6. Both the type of day and the extent of cloud-cover variability were assigned based on the contemporaneous PAM Site data. While there is a huge difference between the daily totals on clear days versus cloudy days, the difference between clear days and variable days is much smaller. In fact, there is quite a bit of overlap between the clear days and variable days, which once again highlights the importance of the diffuse field of radiation in contributing to solar array output. As was seen with the PAM Site data (Figures 4.5 and 4.6), some of the variable days also exhibit higher totals than the clear days.

There are several blue and green dots (representing variable and clear days) during the months of December to March that featured daily totals much lower than the average or expected total and much closer to the output anticipated on overcast days. These data points correlated to days that were one to several days after a snow fall event in the area, as confirmed by archived data from the Rutgers' Gardens weather station. Thus, snow was covering the panels. Accumulated snow on solar panels and the resultant degradation in energy output in a well-known problem [4.21, 4.22], which is exacerbated at the Livingston solar carport canopy due to the canopy's relatively flat orientation, thereby preventing snow from quickly sliding off.

4.4.3. TMY3 Reference Insolation Data

Using these categories as established above in section 4.3.2 we have integrated each day's GHI insolation to arrive at the expected sunlight value as a function of cloud-cover-type, as shown in Figure 4.8. This is very similar in format to the data plotted in

Figure 4.5. One notable difference is that there is less overlap in daily brightness between the categories. This is likely due to the much coarser time granularity; essentially each hour interval provided in the NREL TMY3 data sets is an average over that time frame. Still, the seasonal and cloud cover variations are consistent with the PAM Site and solar array output data presented above and provide a qualitative reference baseline.

4.4.4. Comparing Lot 105 to the Yellow Lot

As described in section 4.2.1 the solar canopies over the Yellow Lot and Lot 105 are identical in structure except for the extent of twist relative to the normally preferred southward orientation. The difference in azimuth angle affects the relative timing of harvested solar energy. Since the Yellow Lot is rotated more towards the east and the rising sun, it starts collecting solar energy earlier in the morning. Meanwhile, since Lot 105 is rotated more towards the west and the setting sun, it starts collecting solar energy later in the morning and continues to collect solar energy for longer in the evening compared to the Yellow Lot. We have compared the electrical output from each lot separately to quantify this effect. Figures 4.9-4.11 display the normalized mean hourly outputs of each solar carport canopy divided into clear, cloudy, and variable days. Due to the preponderance of solar radiation from the direct normal beam on clear days, the difference in timing between the collection of energy is largest for clear days (Figure 4.9) and smallest for cloudy days (Figure 4.11). On cloudy days (Figure 4.11), the two profiles are closest together as most of the total radiation field is composed of diffuse radiation coming nearly equally from all directions. The peak of solar collection is also roughly the same on cloudy days, while there is about an hour’s difference in peak collection during clear (Figure 4.9) and variable days (Figure 4.10). This offset in peak occurrence can be attributed to the azimuth angle and the high proportion of direct radiation on clear and variable days.

Another item of note is the slope of the hourly curves in the morning versus the afternoon, which describes how quickly the rate of energy collection increases in the morning and decreases in the afternoon. The slope for each curve between 7:00 AM to 10:00 AM and between 2:00 PM and 5:00 PM is annotated on each Figure (4.9-4.11). While it is a subtle difference, the slope in the morning is steeper than in the afternoon for all sky cover types. This means that the ramp up of energy collection is faster in the morning, while the afternoon exhibits a longer and slightly more gradual drop off. The greatest slope difference occurs on variable days (Figure 4.10), while the smallest slope difference occurs on cloudy days (Figure 4.11). These ramping up and down differences are discussed in more detail in section 4.5 below.

The differences in Yellow Lot and Lot 105 can also be calibrated by applying the hourly sunlight brightness values in the TMY3 database. As noted above in section 4.2.3 it is possible to estimate sunlight exposure on tilted surfaces by carefully calculating the sun's position at each hour and scaling the hourly normal (DNI) and diffuse (DHI) values appropriately. And, again, splitting the TMY3 days into the three groupings and noting the different azimuth angle for the two arrays, we project these hourly average irradiance values for each of the cloud-cover types, as shown in Figures 4.12-4.14. For clear days (Figure 4.12) we see the most significant difference in sunlight exposure between the two arrays, with the Yellow Lot favoring mornings and Lot 105 favoring afternoons, as was the case with the carport canopy data (Figure 4.9). These data also show that Lot 105 has a slightly higher peak irradiance; this results from it pointing closer to due south than the Yellow Lot does (see Figure 4.2). Cloudy days, on the other hand, are primarily driven by diffuse light so the Yellow Lot and Lot 105 projected sunlight exposures are nearly identical, both in brightness level and in time-of-day variation (Figure 4.14), which was also the case with the carport canopy data (Figure 4.11). Variable days are somewhere in between (Figure 4.13). Further the same early day ramp-up as observed in Figures 4.9-4.11 is observed with the TMY3 data, as is shown by annotated calculations of the slope of each side of the curves.

4.4.5. The Diffuse Field as Related to the Local Cloud Field

A closer look at the temporal variations in local diffuse field can provide further insight into the difference in the energy collection slopes between the morning and the afternoon. Figure 4.15 displays the hourly average diffuse-to-total radiation ratio for clear, cloudy, and variable days using data from the PAM Site. The diffuse-to-total radiation ratio is simply the ratio of DHI to GHI. It can be used as a proxy for cloudy cover but does not entirely explain the local cloud field.

When skies are completely overcast and no part of the direct normal beam is incident on the ground, the ratio of diffuse-to-total radiation is 1. Meanwhile, when skies are completely clear, the direct beam is largely undisrupted, and the diffuse-to-total radiation ratio is much lower. As some of the field is still composed of diffuse radiation, even under totally clear skies, the diffuse-to-total radiation ratio will never be 0. It then follows that the diffuse-to-total radiation ratio falls somewhere between the above values under different cloud fractions and cloud fields. Atmospheric aerosols, such as pollution, smoke, or water vapor, can also affect the diffuse-to-total radiation ratio, as these particles can cause scattering and reflection of direct light, thus contributing to the diffuse field.

As is expected, cloudy days feature the highest ratio in Figure 4.15, while clear days feature the lowest ratio. For both clear and variable days, this ratio is also higher in the morning and evening and lower during the middle of the day, which can be attributed to the sun angle. At lower angles (i.e. when the sun is near the horizon), the direct normal beam must pass through a thicker slice of atmosphere, resulting in additional scattering of light and more contributions to the diffuse field, and can also more easily be interrupted by buildings or vegetation, also contributing to the diffuse field.

One particularly interesting part of this profile is the difference between the morning and evening hours. The rate of decreasing ratio in the morning does not match the rate of increasing ratio in the afternoon and evening. If the cloud field were the same all day long, one would expect a more symmetric curve throughout the day. Instead, a steep and notable increase in the diffuse field is apparent in the late afternoon/early evening hours both during the clear and variable days, which suggests a persistent increase in cloud cover during this time frame. This persistent difference in the diffuse field (and cloud cover) between morning and afternoon hours is likely the main cause of the steeper ramp-up in energy observed in the morning (Figures 4.9-4.11). Since this same steeper curve is also apparent in the profiles created from the TMY3 data (Figures 4.12-4.14), which are created by scaling hourly DNI and DHI values onto panels, this suggests that the ramp-up in early day energy is likely due to differences in the diffuse field.

Diurnal cycles in cloud cover are a common element across the planet, and these cycles are often present in the diffuse radiation field. Over land, solar heating of the surface in the morning often gives rise to convection that may steadily deepen through the day depending upon the lower tropospheric stability [4.18, 4.19, 4.20]. Figure 4.16 illustrates this diurnal cycle in the diffuse field, with larger contributions from the diffuse field occurring in the afternoon versus the morning.

The temporal evolution of this convection may include a clear morning followed by increasing convective activity, which manifests as an increase in the diffuse field radiation and an increase in the variability of the diffuse and direct radiation fields. By late afternoon the diffuse radiation may become dominant due to convective clouds blocking the direct beam almost completely. If the convection is strong enough, high level mixed-phase or ice clouds in the form of active or passive convective anvils may cover the clear sky above this convection further enhancing the diffuse radiation field.

Another common situation is the formation of stratocumulus layers in a post-cold frontal environment [4.23, 4.24, 4.25]. In this situation a capping inversion is present in the lower troposphere and solar heating serves to mix the layer between the surface and this inversion. Moisture gradients across this layer are often present in the morning due to a wet surface from rain or snow and stable conditions during the night. In this environment there are typically no clouds in the morning, but clouds form when the moisture gradient across the lower troposphere is relaxed due to solar-heating driven mixing. Once this stratocumulus cloud forms, the diffuse field becomes dominant. Sometimes this stratocumulus layer will thin near sunset allowing an increase in direct solar radiation as the sun sets. Hence, a statistically meaningful, systematic variation in the diffuse radiation field is present at most over-land locations.

4.4.5. Solar Collection in the Morning versus Afternoon -- Additional Effects

In the preceding section we have highlighted what we believe to be the main factor driving differences in solar array output ramping between morning and afternoon conditions: the increase in diffuse light contributed by convective cloud cover driven by daily warming. While this may be the most significant, there are other effects that may contribute to this observation.

A second important effect that differentiates the morning and afternoon relates to the normal daily change in air temperature and how that might influence the solar array output. Solar panels are known to reduce in efficiency as they get warmer. A typical power reduction coefficient for silicon modules of this type would be around -0.4 %/^{o}C [4.26]. Because of the warming effect of sunlight, we usually see the temperature rising in the morning and reaching a peak somewhere in the middle of the afternoon and cooling gradually in the evening and further at night. Based on the TMY3 for Newark [4.13], our local average daily temperature swing is around 6.5^{o}C. But the temperature is not symmetric about the noon hour; in the morning the sun will be rising higher in the sky with each hour, enhancing the direct contribution to the array's output with a slight moderating effect caused by the module's temperature rise (which will be larger than the air temperature change because of the sunlight absorbed by the module). In the afternoon, on the other hand, the temperature might still be rising some through the mid-afternoon even at a time when the sun will be moving lower in the sky and reducing its direct-beam contribution to the module. Temperature effects are more pronounced when we compare the winter vs. summer electrical output levels (Figure 4.7) in comparison to the sunlight brightness levels (Figure 4.5). Excellent summer days provide around ~8,500 $Wh/m^2/day$ in sunlight exposure compared to around ~3,000 $Wh/m^2/day$ for excellent winter days – almost a 3:1 ratio. On the other hand, excellent summer electrical outputs were ~3,700 kWh/day compared to around ~1,700 kWh/day for excellent winter days – a ratio of only ~2:1. The winter-summer daily peak temperature swing is on the order of 30 degrees, which would cause a significant lowering of array efficiency in the summer.

A third contribution to the AM/PM slight asymmetry could be related to practical electronics limitations for the inverters. Inverter efficiency ratings are often quoted at peak power levels, but their actual efficiency at converting DC to AC will depend on both temperature and power level – but we have no way of diagnosing this as our array power measurements are only for the AC side of the circuit.

4.5. CONCLUSIONS

Solar carport canopy systems not only provide shade, but they can also serve as a valuable source of renewable energy [4.7]. This study leverages observed inverter level data from two separate solar carport canopy systems on the Livingston Campus at Rutgers University to investigate how cloud cover and diurnal variations in the diffuse field influence energy output. While these two installations feature the same tilt angle, they differ in their azimuth angle, which allows for the unique opportunity to study time-of-day output variations as a result of their different orientations.

The inverter level energy output from the two parking lot canopy systems was compared to observed solar irradiance data from the Rutgers' PAM Site as well as longer range standardized historical solar data provided by NREL, allowing for a robust analysis of the solar radiation field and how it applies to actual energy output from a physical solar installation.

The 1-minute solar irradiance data from the Rutgers' PAM Site, including measurements of GHI and DHI, was leveraged to develop a sky cover algorithm that classified days as clear, variable, and cloudy. A similar classification scheme was developed with NREL's TMY3 data to corroborate the general solar insolation patterns observed with the PAM Site sky cover algorithm.

The classifications derived from the PAM Site were extended to the solar canopy data. Cloudy days had the lowest daily integrated energy output, clear days generally had the highest daily integrated energy output, and variable days fell somewhere in between and at times even featured higher energy output than on clear days. These peaks were attributed to partly cloudy sky effects, in which radiation from the direct beam is combined with radiation scattered from nearby cumulus clouds, which is diffuse.

Average daily energy output profiles for each classification were also extracted. It was found that the difference in azimuth angle plays a significant role in the timing of harvested energy on both clear and variable days, with a more minimal effect on cloudy days. The more east-facing array, or the Yellow Lot, starts collecting energy earlier in the morning before the more west-facing array, or Lot 105. The opposite is true in the evening, where Lot 105 continues harvesting energy longer than the Yellow Lot. Further, energy output also tended to decrease more gradually in the afternoon compared to the morning. This less steep slope of energy output in the afternoon was attributed to increased cloud cover in the afternoon and more diffuse radiation (related to the diurnal cloud cycle [4.19, 4.20]) and reduced solar panel efficiencies with higher temperatures in the afternoon [4.26].

Chapter 5:

Conclusion and Future Directions

5.1. CONCLUSION

The overarching theme of this body of work can be reduced to one key concept: the oftentimes undervalued importance of the diffuse field of radiation as it relates to solar panels. This key idea was studied and analyzed over the course of three separate but interconnected projects.

5.1 Conclusions from Chapter 2

Chapter 2 conducts a comprehensive and qualitative analysis of the solar irradiance field across the United States using the NSRDB. A 15-year climatology of diffuse and direct radiation is computed, both on a national scale and a regional scale, by breaking the country into eight geographically and climatologically different regions. The seasonal and annual controls and variations in these fields are explained by analysis of the cloud cover, aerosol optical depth (AOD), precipitable water, geography, and altitude of the site locations.

From a continental point of view, the climatology of direct radiation varies in two primary ways depending on the time of year. During the fall and winter months, the direct radiation field varies predominantly in the north-south direction, which is driven by the solar zenith angle. Meanwhile, there is a larger east-west variation during the spring and summer months, which is indicative of a higher dependence on a site's elevation, AOD, and cloud cover. Further, the is an overall higher ratio of diffuse radiation across the eastern US, which is due to more frequent cloud cover as well as generally lower elevations relative to the western US.

From a regional point of view, the ratio of diffuse to direct radiation varies most from May to September, which is primarily driven by regional gradients in elevation, cloud cover, and AOD. Further, the immediate West Coast exhibits the largest year-on-year variability in the solar irradiance field, which can be attributed to large scale climate patterns, such as the El Nino Southern Oscillation (ENSO).

Our findings relative to the variance of the diffuse-to-direct radiation ratio called into question the current way in which many large solar panel arrays are organized. More specifically, solar panels are generally oriented so that their surface is as close to perpendicular to the direct beam, which is optimized for energy harvest of the direct beam. In locations where the diffuse field accounts for a significant portion of the total global horizontal irradiance, such as the Great Lakes or portions of the interior Northeast, we argue that solar arrays should be better tuned to the diffuse field. We also question whether or not solar arrays that feature all panels tilted at the same angle are missing out on a significant portion of the diffuse field.

5.2 Conclusions from Chapter 3

Chapter three is a theoretical study. An alternative approach of organizing large solar panel arrays is suggested, which considers the co-optimization problem of maximizing per-panel incident energy and minimizing the amount of space to do this. This approach introduces a new technique, called the dual-angle solar harvest (DASH) method, in which a solar array is composed of two tilt angles. The premise for this new method was to ultimately save on land costs as the cost of land is rising while the cost of solar panels is falling.

While no pair of angles for two solar panels can ever top the amount of energy that is incident on a pair of solar panels both tilted at the single optimized tilt angle, it can come close. In order to increase array-wide harvested energy, more rows of panels must be installed in the same footprint. This is best done by using panels oriented with lower tilt angles as they can be spaced closer together without adverse shadowing effects.

The DASH method is first evaluated at two climatically and geographically different locations: Akron, OH and Barstow, CA. All combinations and pairs of angles are explored to see how changing different fractions of panel angles affects the array-wide incident solar energy. The DASH method is then explored nationwide, constraining one of the tilt angles to the single optimum tilt angle. With this constrained problem, only 35% of the panel rows must be adjusted in Akron to observe a 10% gain in array-wide incident solar energy, compared to double (70%) the amount in Barstow. For a 20% gain, 55% of the panel rows must be adjusted in Akron, while no fraction of adjustment can produce a 20% gain in Barstow while holding one panel tilt angle steady at the optimum tilt angle.

Nationwide, the best performance using the DASH method occurs across the Pacific Northwest and the Great Lakes, where conditions are cloudier and where the diffuse component of radiation accounts for a significant portion of the total radiation field. The lower angles of the DASH method, which enable more panels to fit within a constrained space, are better suited for harvesting of the diffuse field, which is more dominant in cloudier regions.

5.3 Conclusions from Chapter 4

The fourth chapter investigates how cloud cover and the diurnal cycle of diffuse radiation contribute to time-of-day energy output from two different solar carport canopies on the Livingston Campus at Rutgers University, which are identical in installation in every way except for azimuth tilt. The Yellow Lot is oriented more to the east, while Lot 105 is oriented more to the west.

The difference in time-of-day energy output is largest for clear days and variable days as there is a larger component of direct beam irradiance compared to the cloudy days. Thus, as the Yellow Lot faces more to the east, it starts collecting energy earlier than Lot 105. Conversely, as Lot 105 faces more to the west, it continues collecting energy later in the day compared to the Yellow Lot.

Differences in slope between ramp up of energy output in the morning and ramp down of energy output in the afternoon are observed, with a steeper slope in the morning hours and a more gradual slope in the afternoon hours. The more gradual slope in the afternoon is attributed to a preponderance of cloud cover that develops in the late afternoon/early evening (diagnosed by observations of higher diffuse-to-total radiation ratios later in the day) as well as decreased solar panel efficiencies observed with increased temperatures.

Further, the sky condition classification algorithm showed that roughly 20% of the days in this region are clear, 40% of the days are cloudy, and 40% of the days are variable. In other words, the diffuse component is large. This finding reinforces the findings from Chapter 2, in which it was shown that the diffuse field accounted for a significant portion of the total radiation field across the Northeast.

5.2 FUTURE DIRECTIONS

Part of this dissertation introduced the DASH method, which is an alternative approach to organizing large solar panel arrays by implementing two panel tilts angles. As with the development of any new process or approach, there is always a ton of additional work that could be done. The DASH method as in this dissertation can be thought of as the first iteration of the model.

In Chapter 3, It was shown that the DASH method performs best where conditions are cloudier, such as the Pacific Northwest and the Great Lakes region. This suggested that the DASH method was better tuned to the diffuse field of radiation. Another avenue of work should be further analysis of solar harvest methods in partly cloudy climates. The DASH method is but one attempt at developing a new method for harvesting more complex radiation fields. Other approaches could involve using more than two angles or organizing solar panels in a shape other than the standard row-by-row design.

Additionally, a more sophisticated approach to modeling the plane-of-array insolation used in the DASH method could be employed. In this dissertation, the Klucher model [5.1] was used in modeling the plane-of-array diffuse radiation, which is certainly more complex than a purely isotropic model but is still relatively simple. There are more complex and sophisticated models out there, such as that developed by Kocifaj [5.2, 5.3]. Thus, future work could be done in the method of modeling plane-of-array insolation.

At the moment, the DASH method only uses modelled irradiance data from the NSRDB [5.4] to model the plane-of-array solar radiation. In Chapter 4, 1-minute observed radiation data from the Rutgers' PAM Site were used in analyzing time-of-day differences in energy output between two different solar carport canopies. These same irradiance data could be used in modeling the plane-of-array radiation in New Brunswick to see if the DASH method works as expected with NSRDB data versus observed irradiance data. The PAM Site data also provide temporally detailed information, which could be used to explore hourly performance of the DASH method, particularly when conditions are partly cloudy.

Finally, the DASH method could be expanded to be used in conjunction with forecast irradiance and cloud data. Are persistent stratus clouds expected? Are fair-weather cumulus clouds expected to develop throughout the afternoon? These cloud and sky condition forecasts could be used in tandem with the DASH method to recommend an ideal pair of angles for that day, which takes into account both the time of year and the expected sky cover. Whereas typical solar tracker systems move the panels throughout the day, a hybrid DASH tracker system could arrange the panels in a single dual-angle orientation all day, which is based off the forecast for the day, thereby reducing energy costs and resulting in a solar arrangement that is optimized for each day's local radiation field.

A lot of work remains for fine tuning the DASH method. This thesis only serves as the first iteration of the DASH method. As described above, there are several avenues of research that could be explored. It is the hope that the DASH method ignites a new discussion on the way in which large solar panel arrays are currently organized.

Region	Number of Stations
Northeast	113
Southeast	133
Midwest	148
South-Central	87
Plains	90
Northwest	72
Southwest	95
Desert Southwest	40
Total	**788**

Table 2.1. **Regional Distribution of Stations:** This table displays the number of Class I and Class II stations at each of the eight sub-divided regions for this study.

		Barstow, California			Akron, Ohio		
		# Extra Panel Rows	Beta1	Beta2	# Extra Panel Rows	Beta1	Beta2
Percent Gain of F_{TOT}	5.0%	6	21°	27°	6	21°	26°
	10.0%	11	18°	24°	11	19°	24°
	20.0%	23	20°	14°	22	14°	20°
	50.0%	--	--	--	58	4°	9°
Location	Latitude	34.85°N			40.92°N		
	Longitude	116.8°W			81.43°W		
	Elevation	215 m			368 m		
	Optimum Tilt	30°			28°		

Table 3.1 **Test Station Details:** Specific details for the two test stations of Barstow, CA and Akron, OH regarding the number of panels necessary to observe specific energy gains using the DASH method with a 30/60 tilt angle split between β_1 and β_2, as well as each station's latitude, longitude, elevation, and optimum tilt angle.

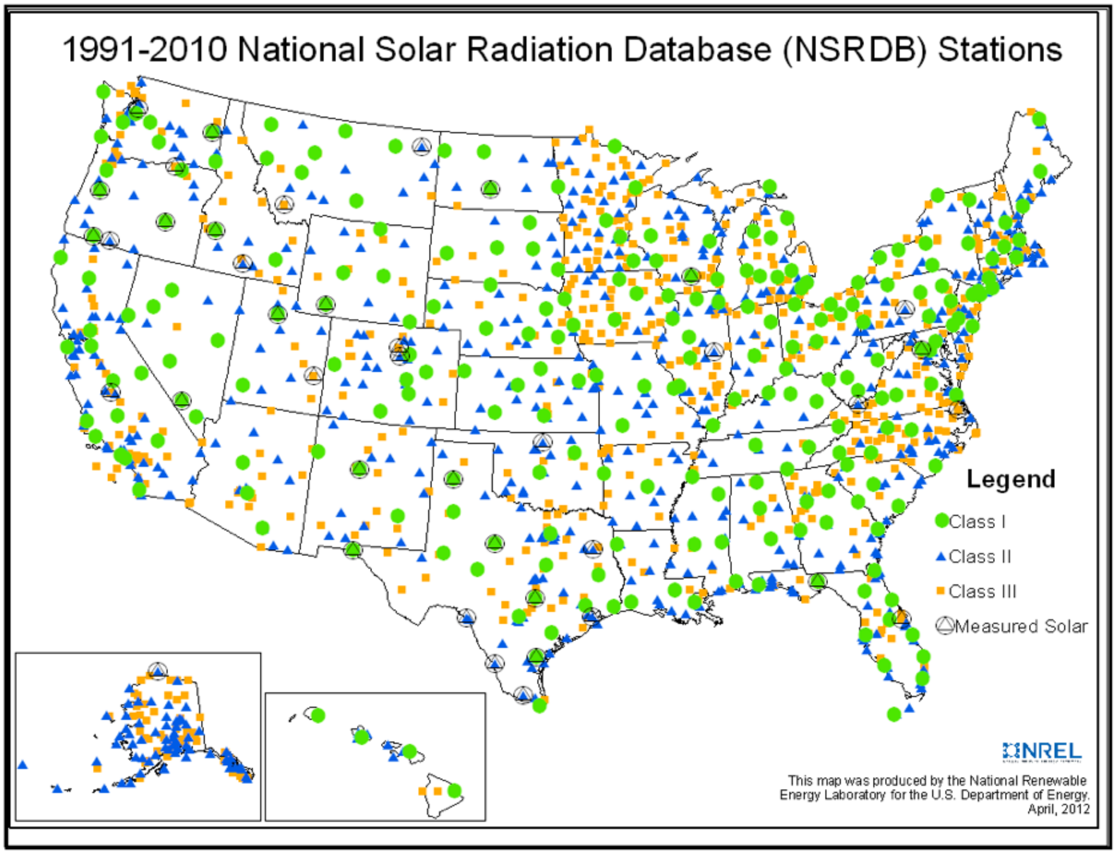

Fig 2.1. **NSRDB Station Locations**: The locations and divisions of all 1,454 NSRDB stations. Class I stations (242; green circles) contain a complete period of record with the highest quality solar modeled data, Class II stations (618; blue triangles) contain a complete period of record but have some significant periods of interpolated or filled data, and Class III stations (594; orange squares) have gaps in their period of record but all have at least three years of data. There are also 40 total sites with measured data (white circle with inlaid triangle), but none have a complete period of record. From the NSRDB 1991-2010 User's Manual [2.19].

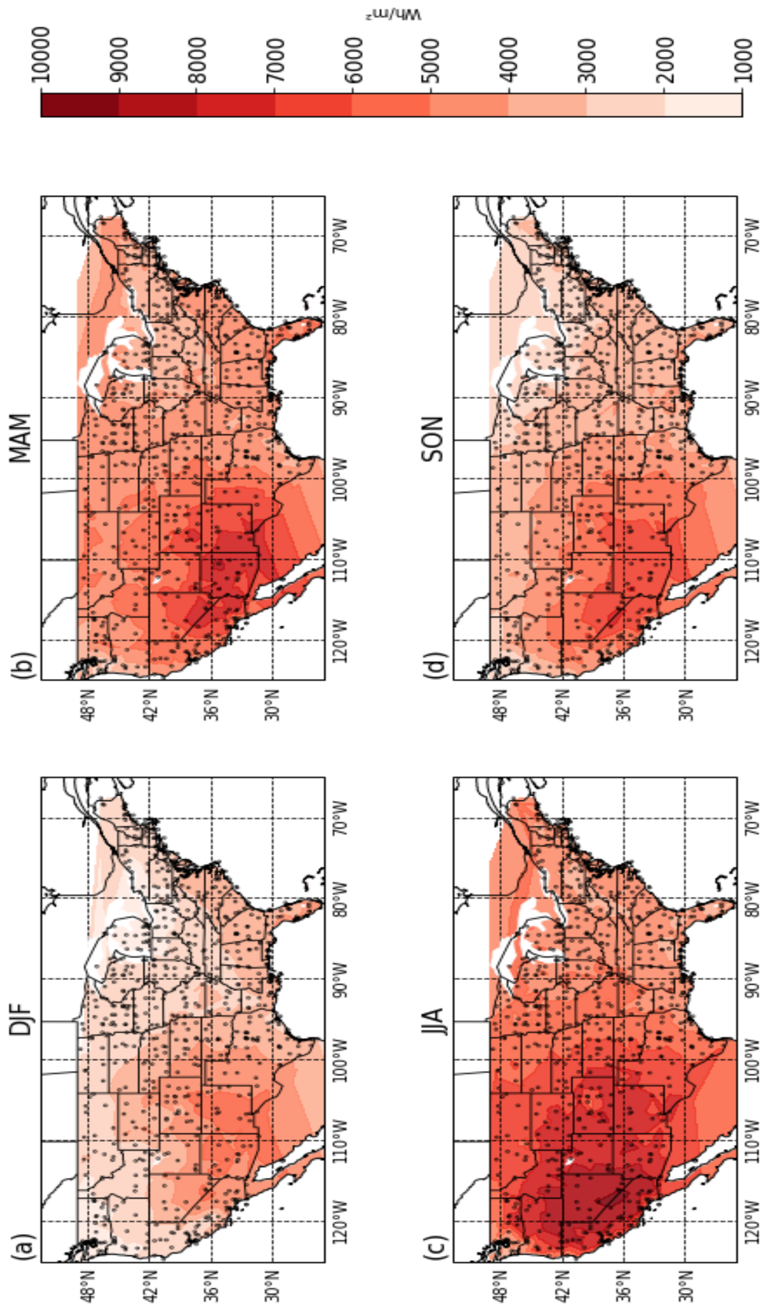

Figure 2.2. **1991-2005 Average Direct Radiation:** The average direct radiation (Wh/m2) for each season: December-January-February (a), March-April-May (b), June-July-August (c), and September-October-November (d). The dots represent the locations of the individual Class I and Class II stations from the NSRDB, which were used to interpolate the data across the entire continental US.

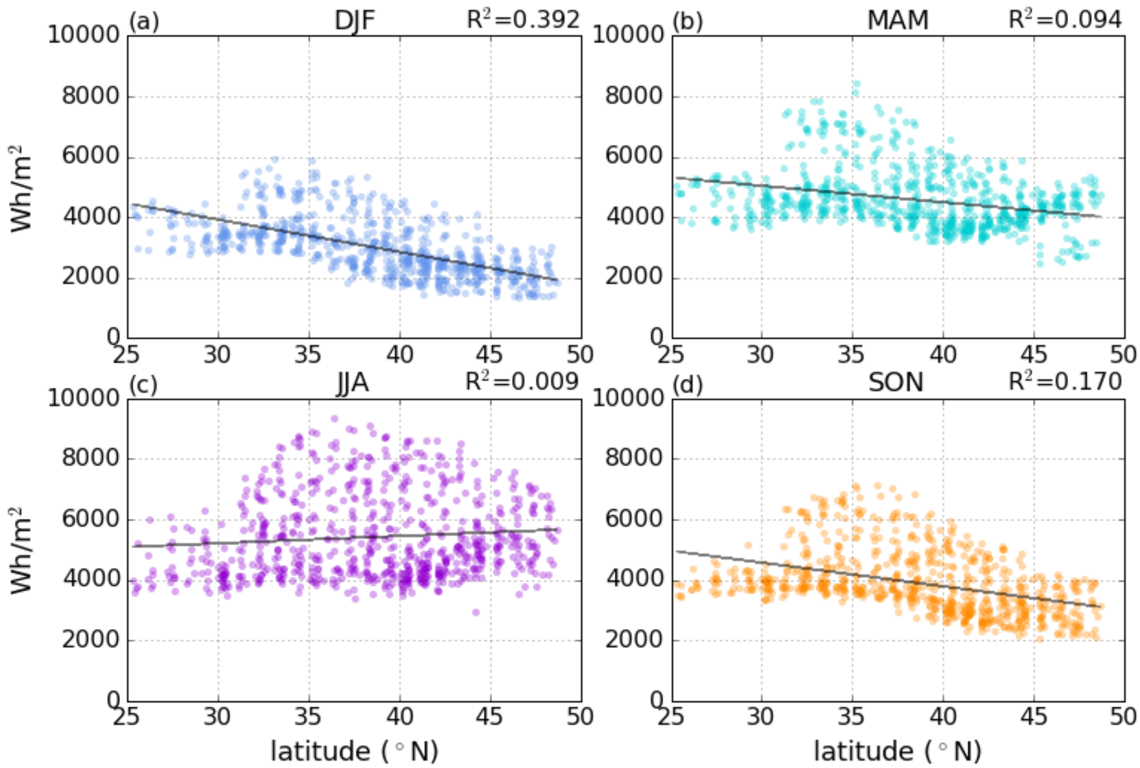

Figure 2.3. **Average Direct Radiation versus Latitude:** Direct radiation at each station plotted against latitude for December-January-February (a), March-April-May (b), June-July-August (c), and September-October-November (d). Each point is semi-transparent; thus, the opaquer the scatter points, the larger the concentration of direction radiation values at that particular latitude. The best fit line is plotted over the data, and the associated R^2 value is labeled in each panel.

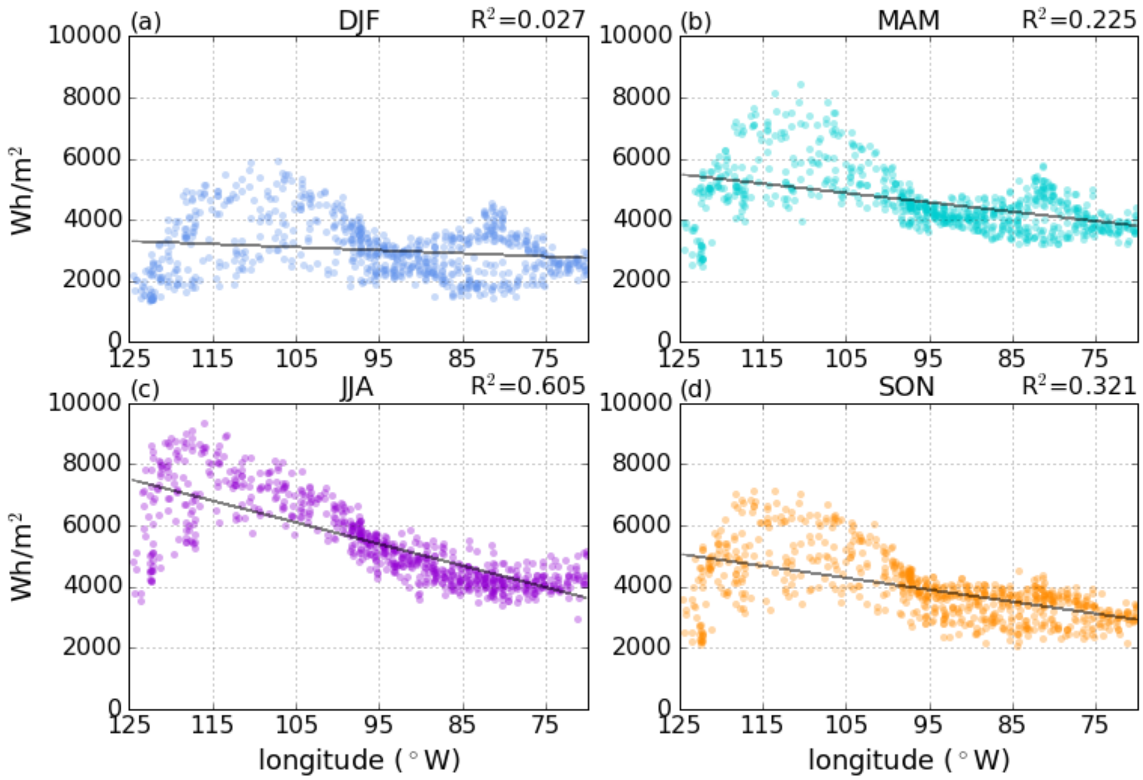

Figure 2.4. **Average Direct Radiation versus Longitude:** Direct radiation at each station plotted against longitude for each season. December-January-February (a), March-April-May (b), June-July-August (c), and September-October-November (d). This is plotted the same way as Figure 2.3.

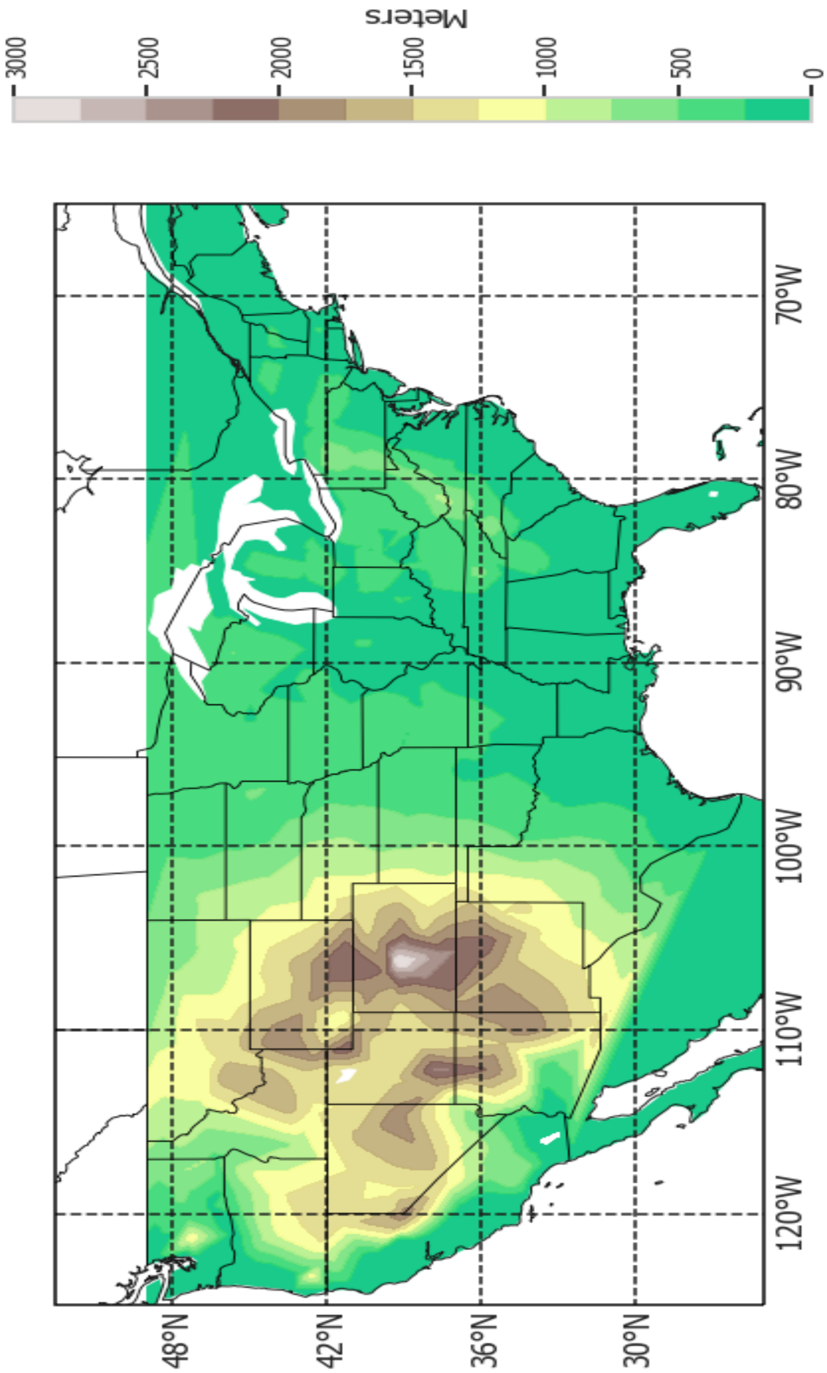

Figure 2.5. **Elevation at Each Station:** Interpolated elevation, in meters above sea level, using data from all NSRDB stations (including Class I, Class II, and Class III stations). The actual elevation may not match a true elevation map due to the location of stations.

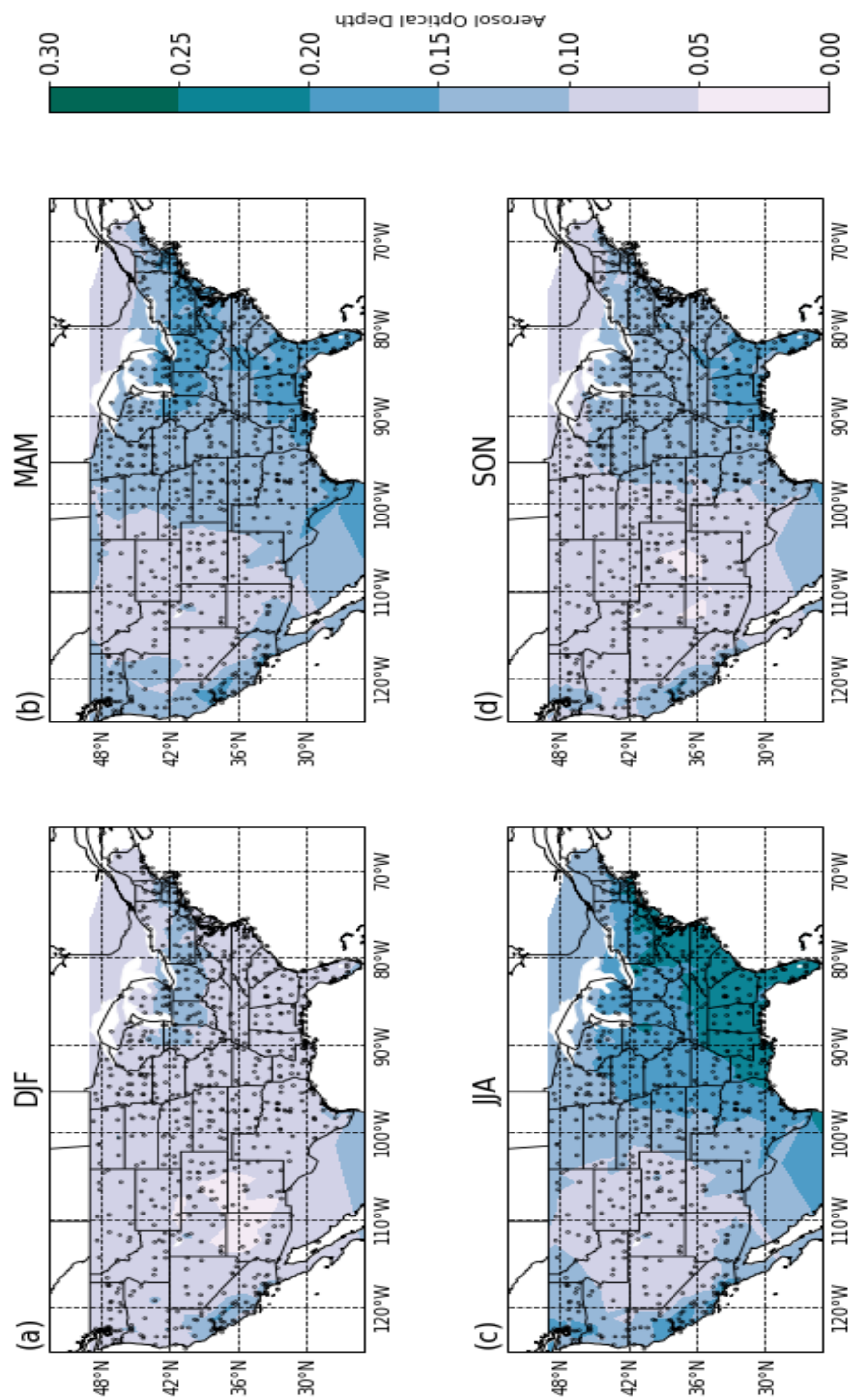

Figure 2.6. **1991-2005 Average Aerosol Optical Depth:** The average aerosol optical depth for each season: December-January-February (a), March-April-May (b), June-July-August (c), and September-October-November (d). Plotted the same way as in Figure 2.2.

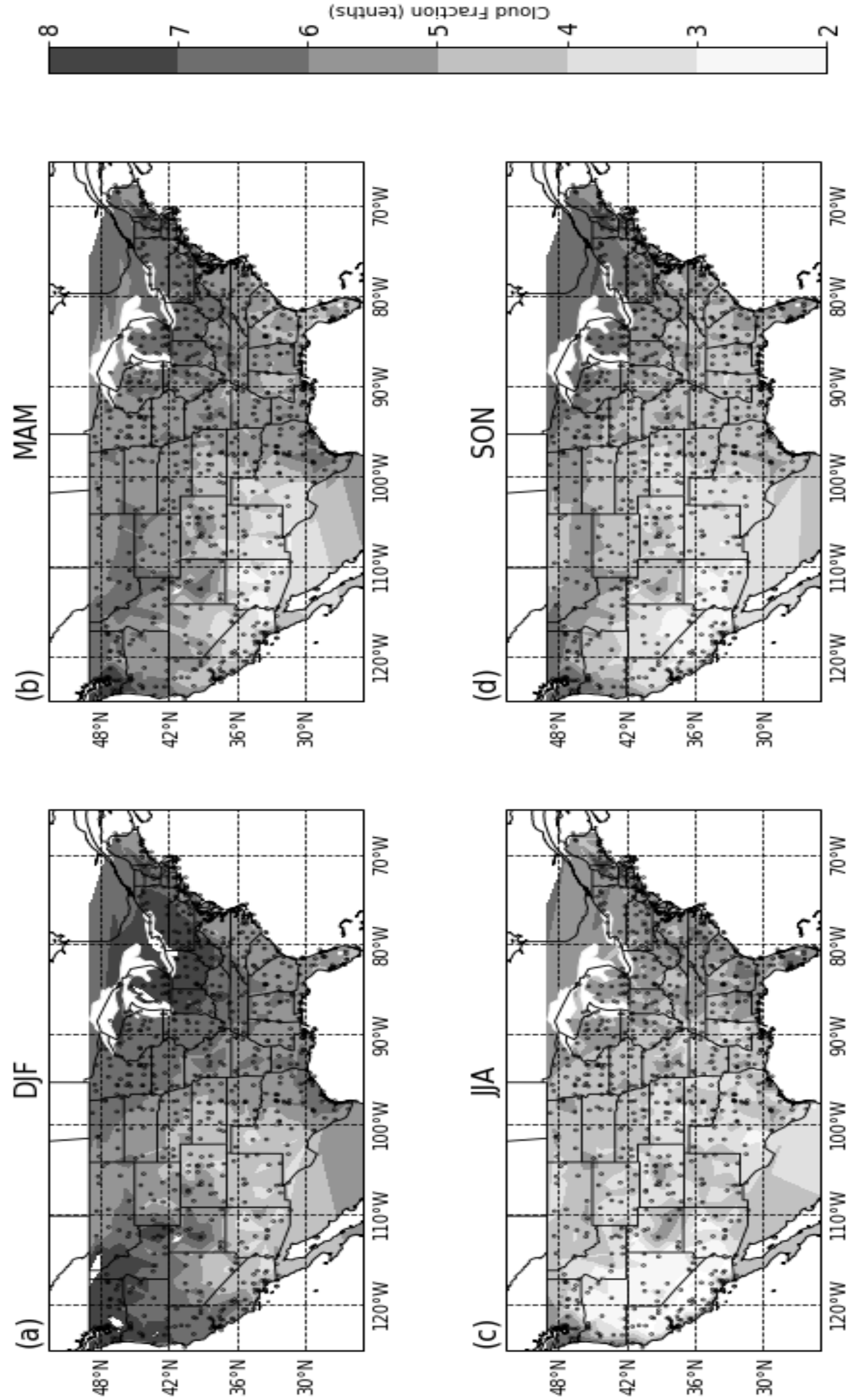

Figure 2.7. **1991-2005 Average Total Sky Cover:** The average total sky cover (in tenths) for each season: December-January-February (a), March-April-May (b), June-July-August (c), and September-October-November (d). Plotted the same way as in Figure 2.2.

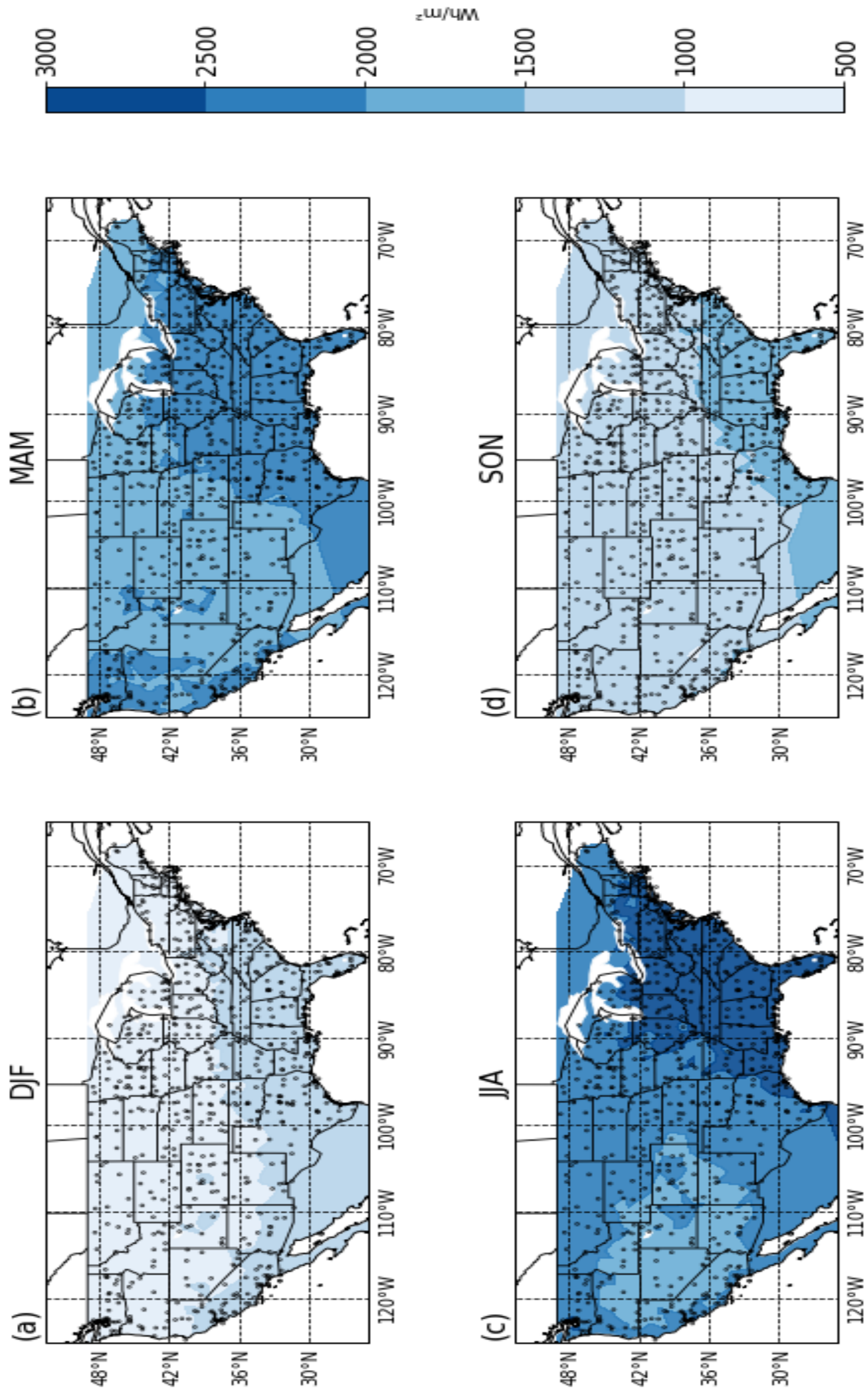

Figure 2.8. **1991-2005 Average Diffuse Radiation:** The average interpolated diffuse radiation (Wh/m^2) for each season: December-January-February (a), March-April-May (b), June-July-August (c), and September-October-November (d). Plotted the same way as in Figure 2.2.

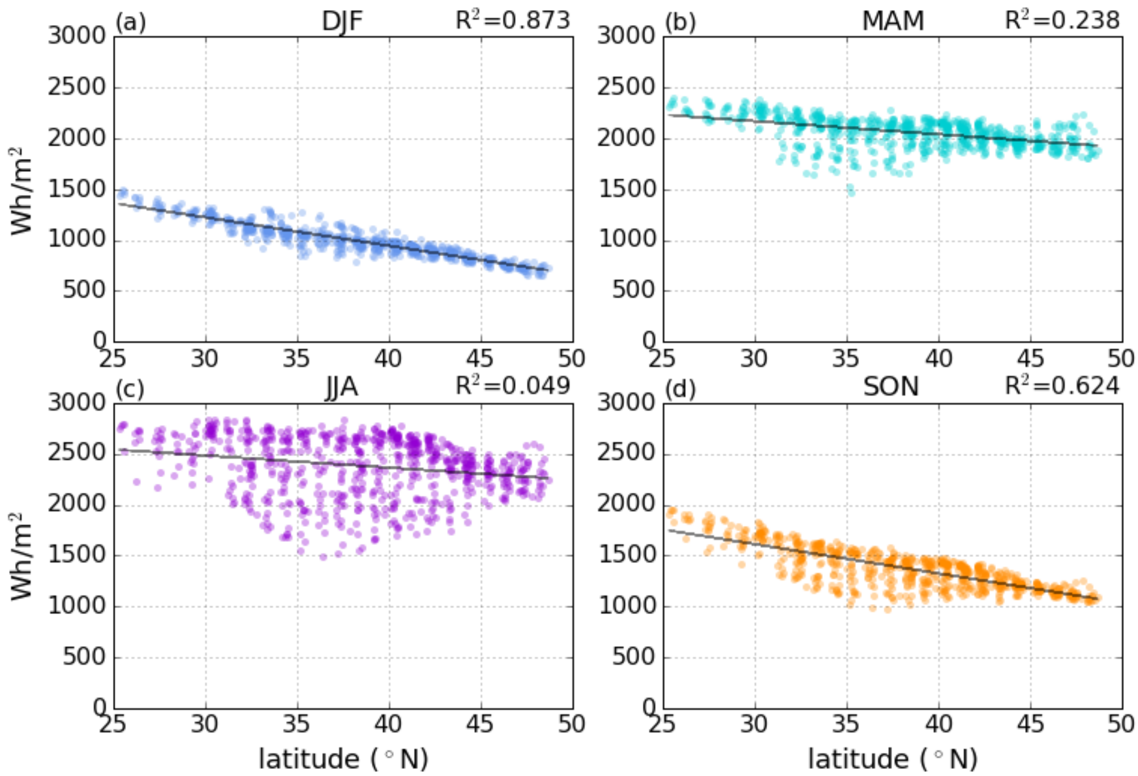

Figure 2.9. **Average Diffuse Radiation versus Latitude:** Diffuse radiation at each station plotted against latitude for December-January-February (a), March-April-May (b), June-July-August (c), and September-October-November (d). Plotted the same way as in Figure 2.3.

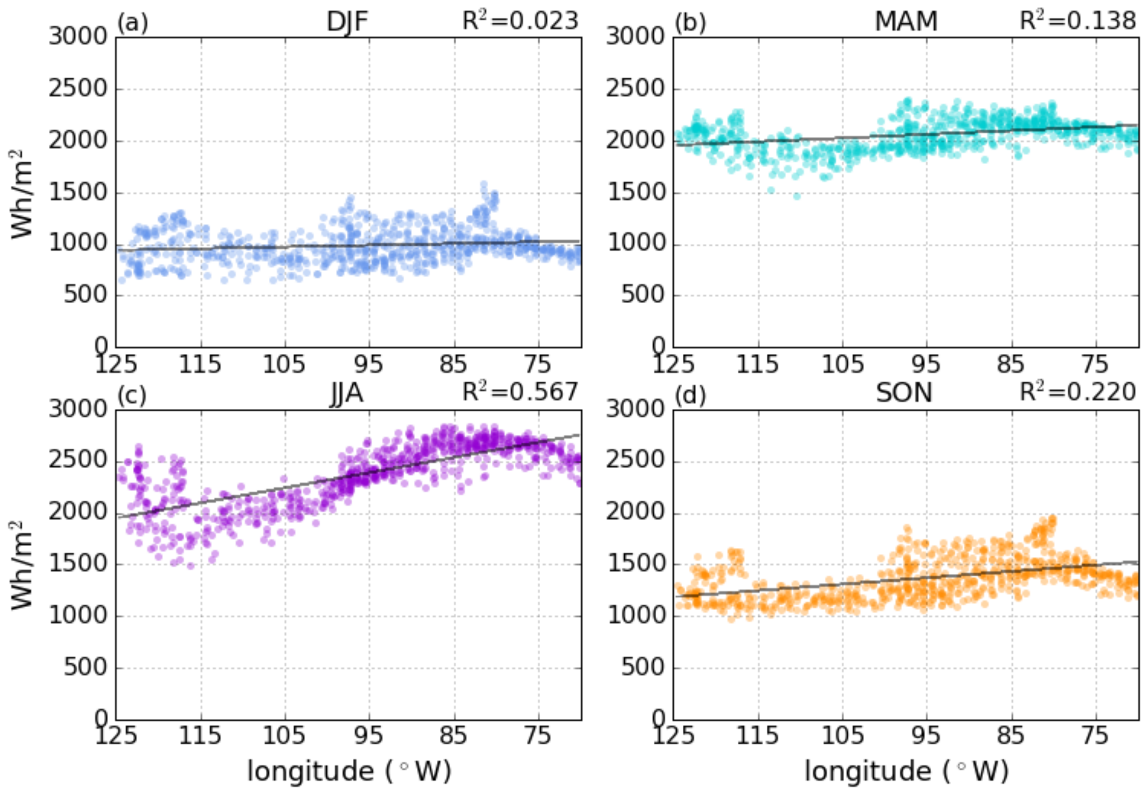

Figure 2.10. **Average Diffuse Radiation versus Longitude**: Diffuse radiation at each station plotted against longitude for December-January-February (a), March-April-May (b), June-July-August (c), and September-October-November (d). Plotted the same way as in Figure 2.3.

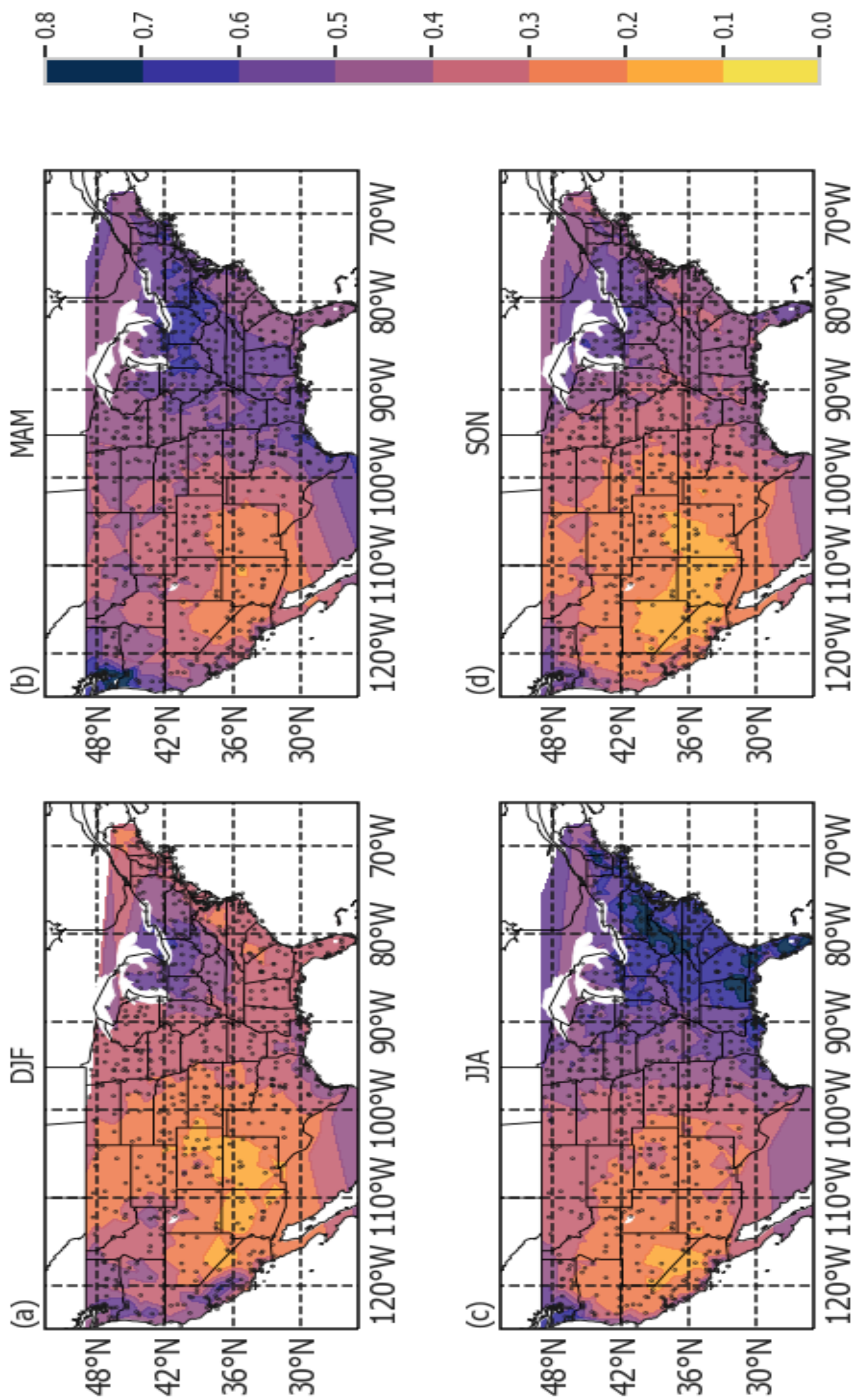

Figure 2.11. **1991-2005 Average Ratio of Diffuse to Direct Radiation:** The average interpolated ratio of diffuse radiation to direct radiation for each season: December-January-February (a), March-April-May (b), June-July-August (c), and September-October-November (d). Plotted the same was as in Figure 2.2.

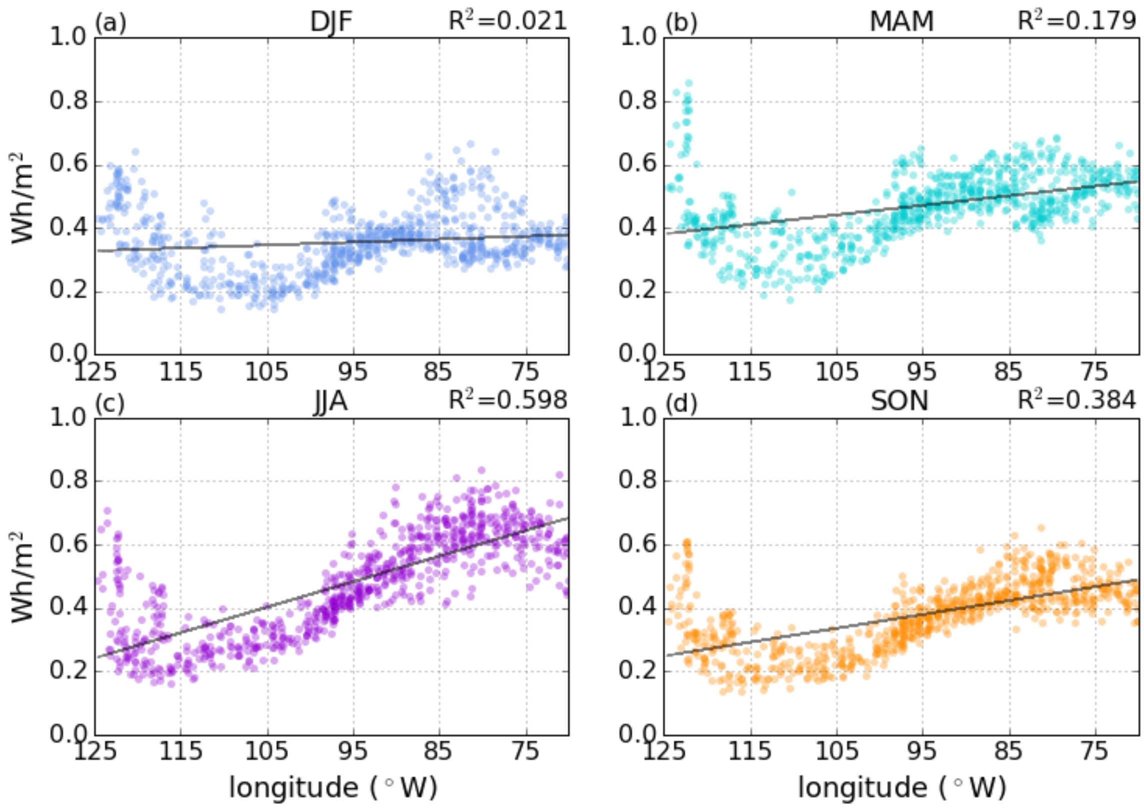

Figure 2.12. **Avg Ratio of Diffuse to Direct Radiation versus Longitude:** Ratio of diffuse to direct radiation at each station plotted against longitude for December-January-February (a), March-April-May (b), June-July-August (c), and September-October-November (d). This is plotted the same way as Figure 2.3.

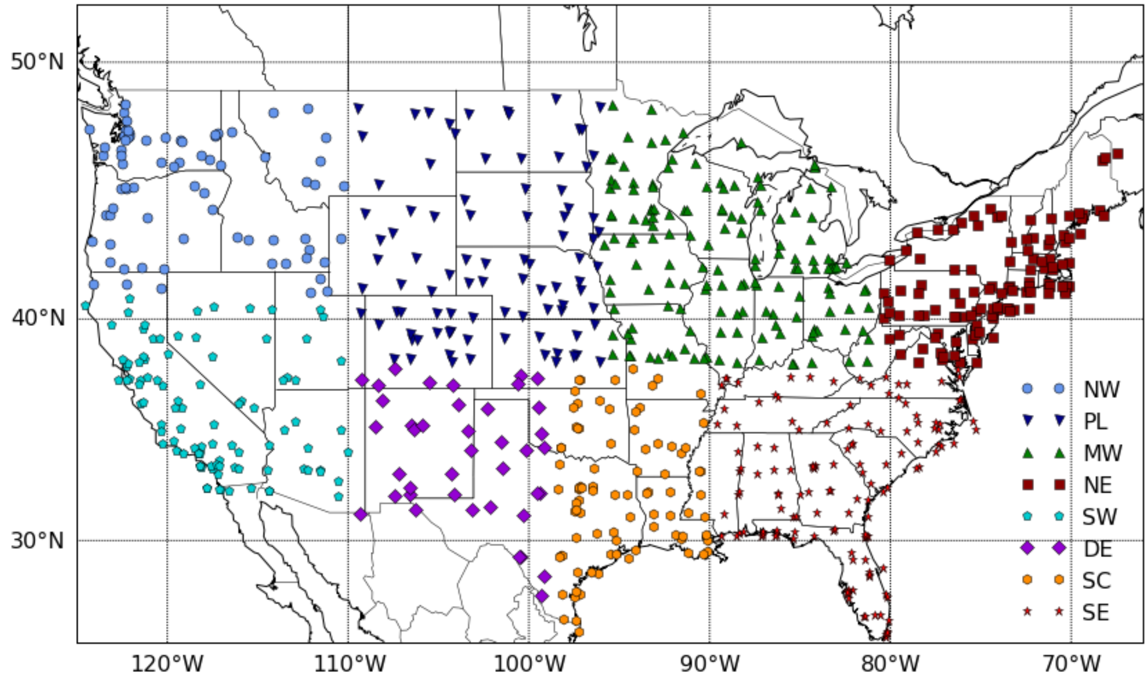

Figure 2.13. **Location of Regional Stations:** The location of each Class I and Class II station, colored according to which region it was sub-divided into for this study.

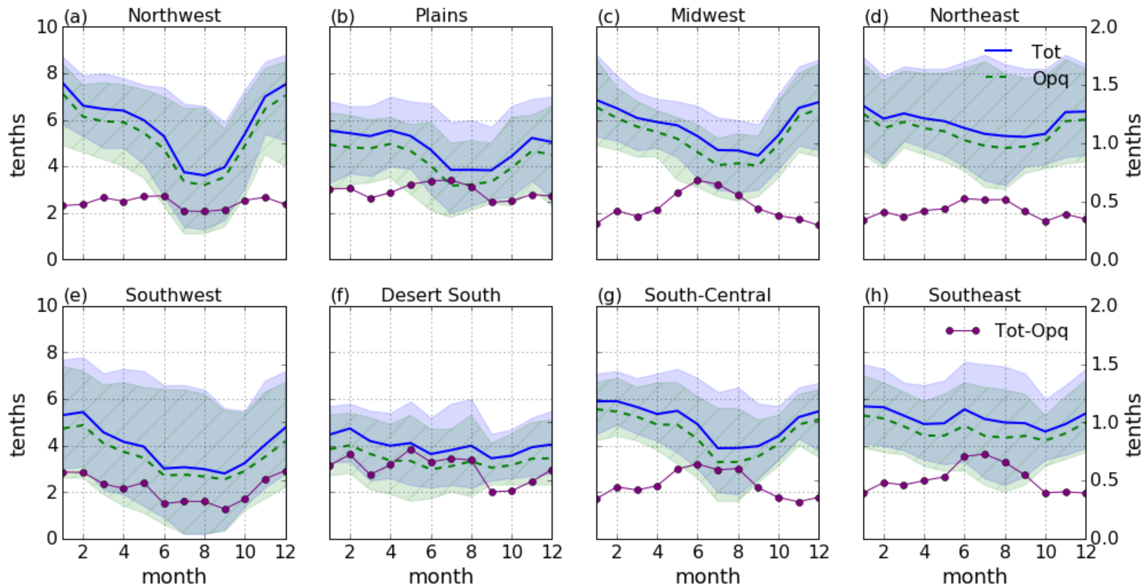

Figure 2.14. **1991-2005 Mean Total & Opaque Sky Cover for Each Region:** The average 15-year mean monthly and 15-year envelope of minimum to maximum values of total sky cover (blue line) and opaque sky cover (green dashed line) in the Northwest (a), Plains (b), Midwest (c), Northeast (d), Southwest (e), Desert-Southwest (f), South-Central (g), and Southeast (h). These are plotted against the left vertical axis. The difference between total and opaque sky cover is represented by the purple line with circles and is plotted against the right vertical axis.

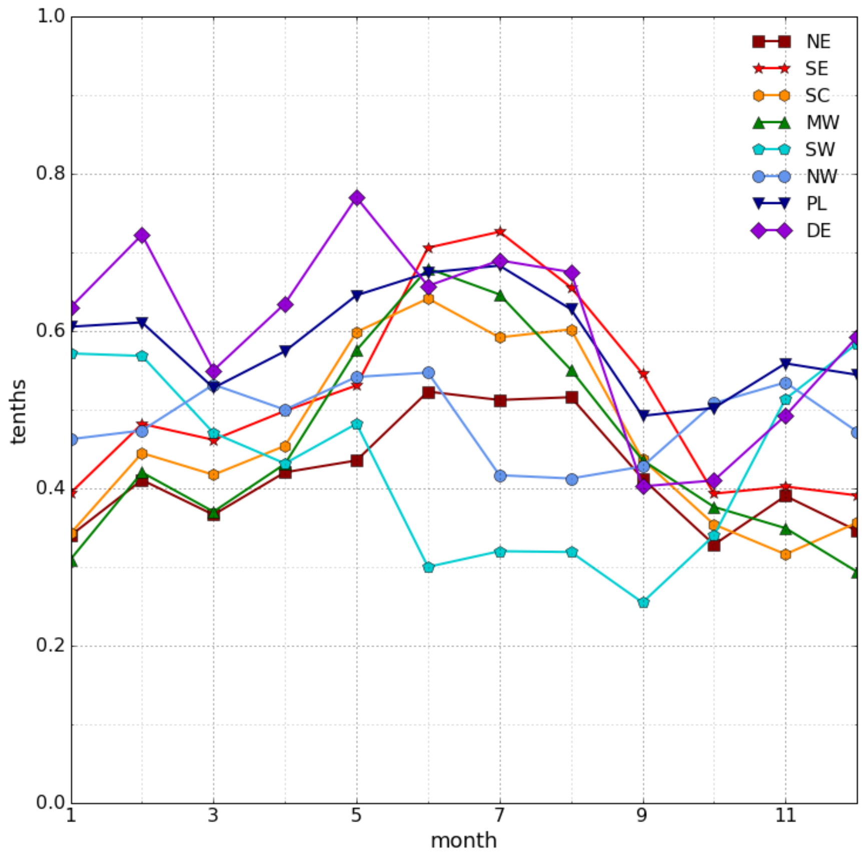

Figure 2.15. **Total – Opaque Sky Cover:** The annual cycle of total-opaque sky cover, which is a proxy for optically thin clouds, for each of the eight regions according to the key on the upper right.

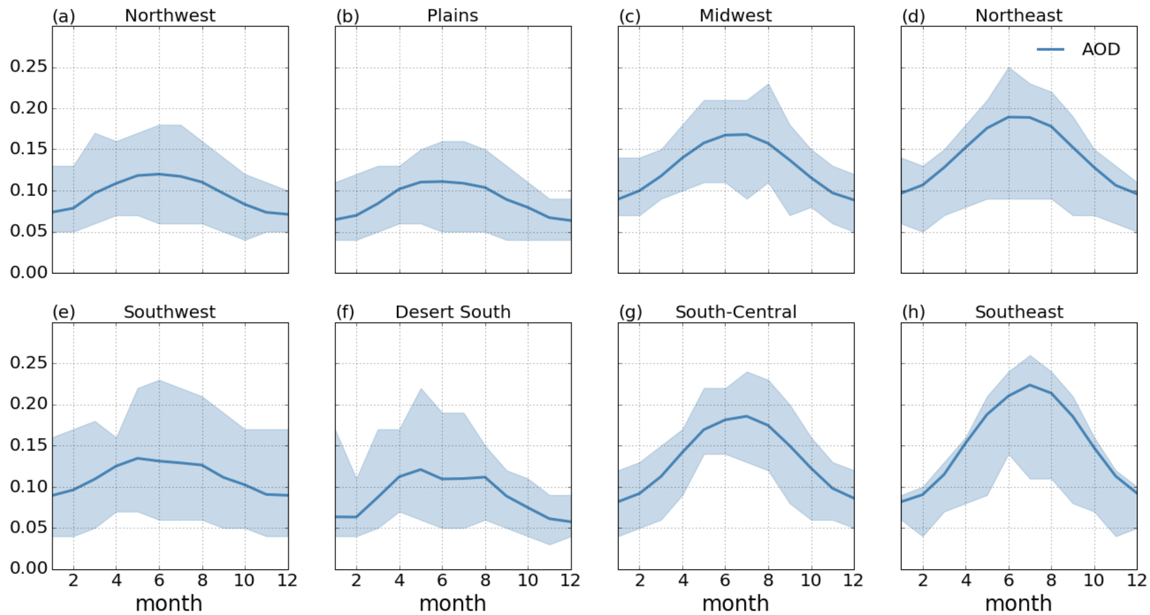

Figure 2.16. **1991-2005 Mean Aerosol Optical Depth for Each Region:** The average 15-year mean monthly (black line) and 15-year envelope of minimum to maximum values (grey shading) of aerosol optical depth in the Northwest (a), Plains (b), Midwest (c), Northeast (d), Southwest (e), Desert-Southwest (f), South-Central (g), and Southeast (h).

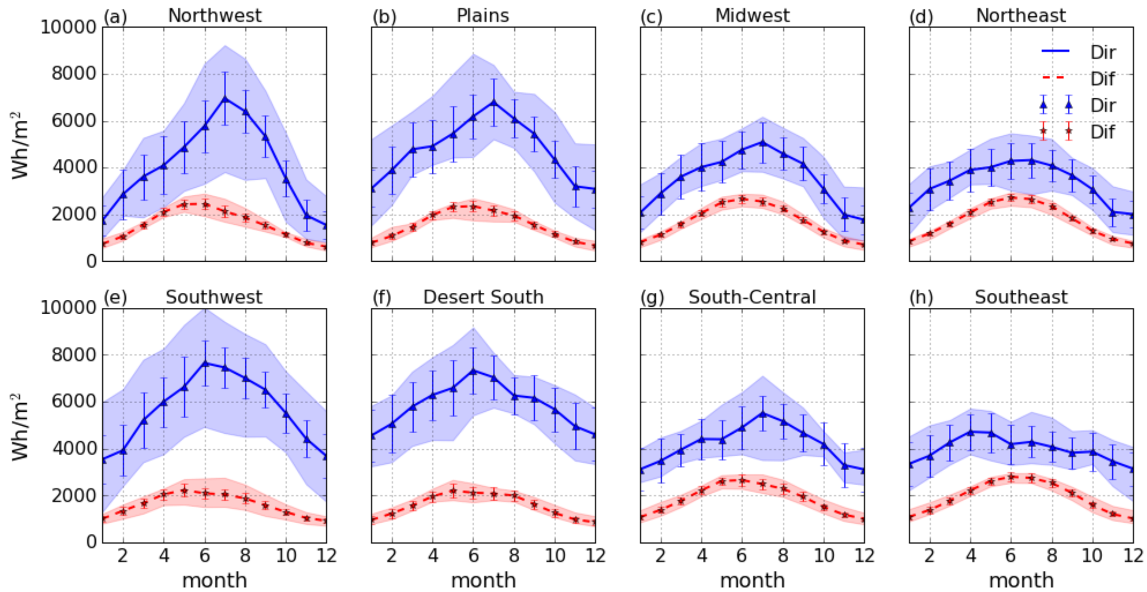

Figure 2.17. **1991-2005 Mean Direct & Diffuse Radiation for Each Region:** The average 15-year mean monthly direct (blue solid line) and diffuse (red dashed line) radiation in the Northwest (a), Plains (b), Midwest (c), Northeast (d), Southwest (e), Desert-Southwest (f), South-Central (g), and Southeast (h). The shading represents the envelope of minimum to maximum annual means within the region, while the vertical bars indicate the interannual variability in the entire dataset.

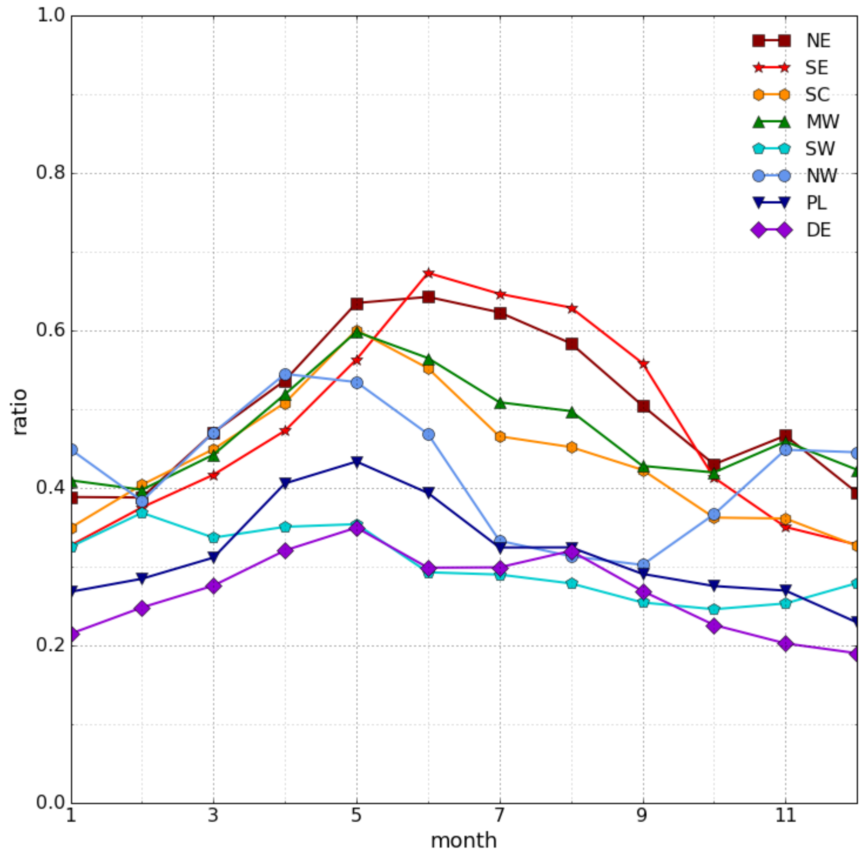

Figure 2.18. **Ratio of Diffuse to Direct Radiation for Each Region:** The annual cycle of the ratio of diffuse to direct radiation for each of the eight regions, according to the key in the upper right. A value closer to one indicates that the diffuse radiation is near to or equal to the direct radiation, while a value closer to zero indicates a large gap between the direct radiation and the diffuse radiation.

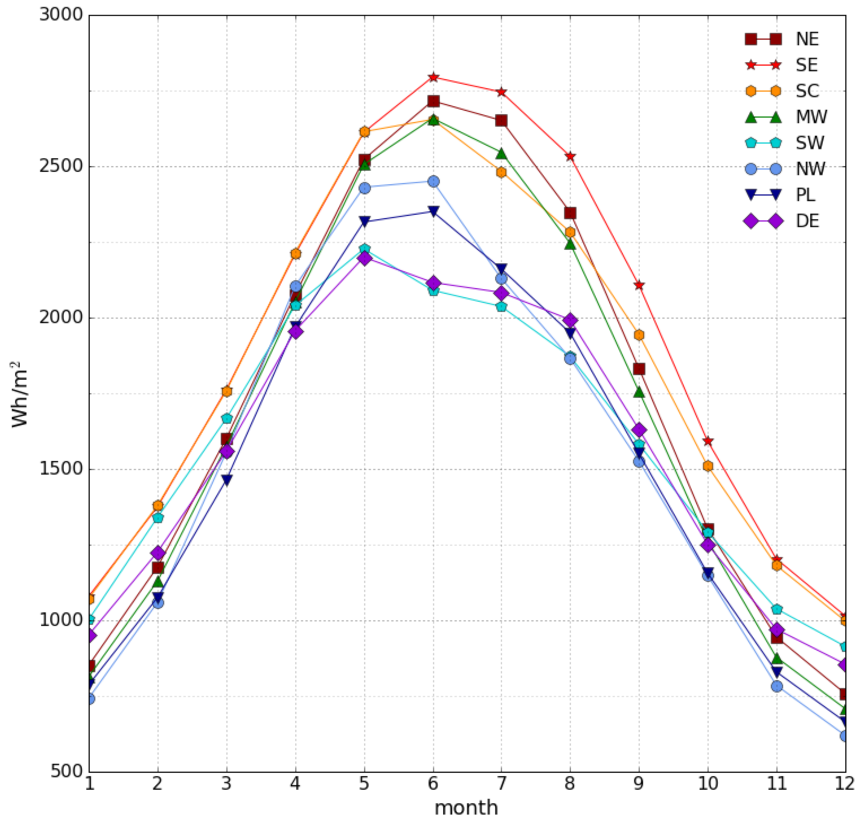

Figure 2.19. **1991-2005 Mean Diffuse Radiation for Each Region:** The annual cycle of average mean diffuse radiation for each of the eight regions, according to the key in the upper right.

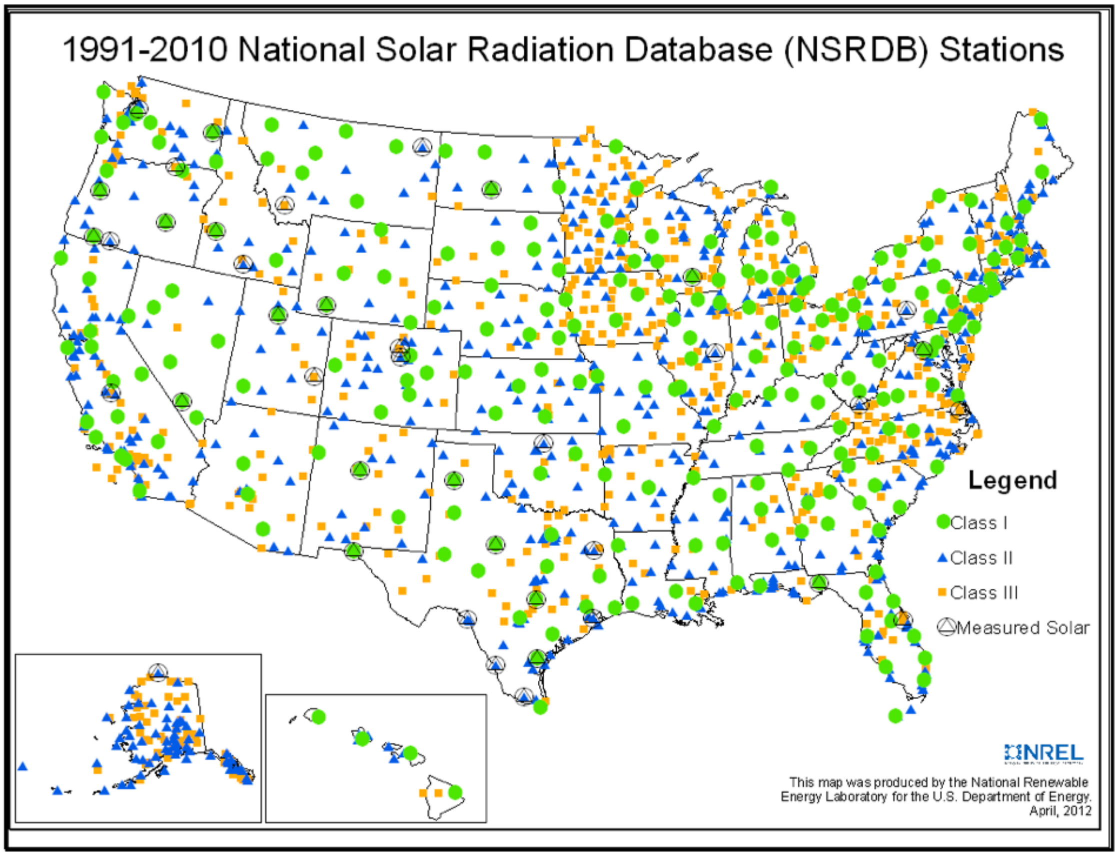

Figure 3.1 **NSRDB Station Locations:** The locations and divisions of all 1454 NSRDB stations. Class I stations (242; green circles) contain a complete period of record with the highest quality solar modeled data, Class II stations (618; blue triangles) contain a complete period of record but have some windows of quality interpolated period, and Class III stations (594; orange squares) have gaps in their period of record but all have at least three years of data. There are also 40 total sites with measured data (white circle with inlaid triangle), but none have a complete period of record. From the NSRDB 1991–2010 User's Manual.

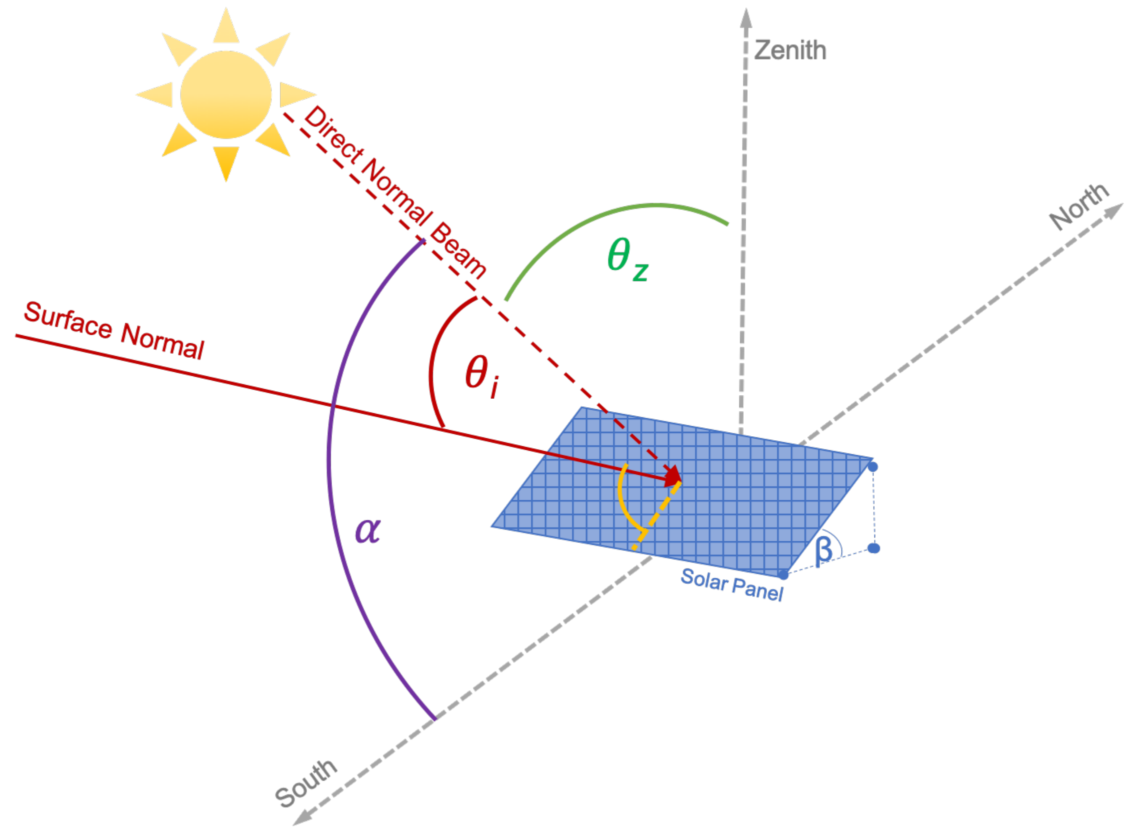

Figure 3.2 **Geometry of the Sun with respect to a Solar Panel:** The various angles associated with a solar panel with tilt, β. The solar panel is in the Northern Hemisphere as the panel is facing south. α is the solar elevation angle of the sun with respect to the horizon, θ_Z is the solar zenith angle, and θ_i is the angle of incidence, which is the angle between the direct normal beam and the surface normal with respect to the solar panel.

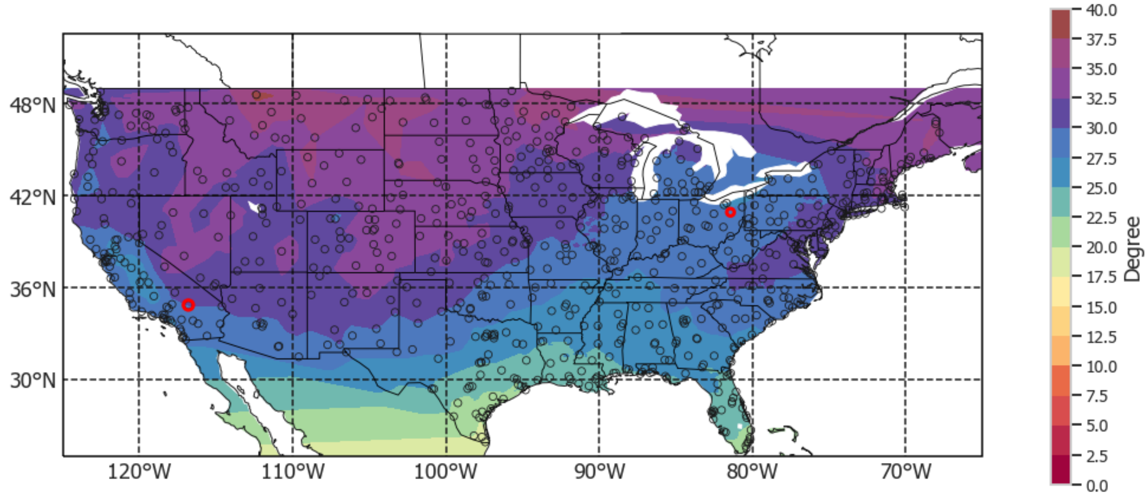

Figure 3.3 **Single Optimized Tilt Angle:** Each dot represents the calculated optimum tilt angle for each Class I and Class II station in the NSRDB, while the color fills are interpolated from the station data. Tilt angles are color-contoured every 2.5 degrees. The test locations of Barstow, CA and Akron, OH are marked by the red circles.

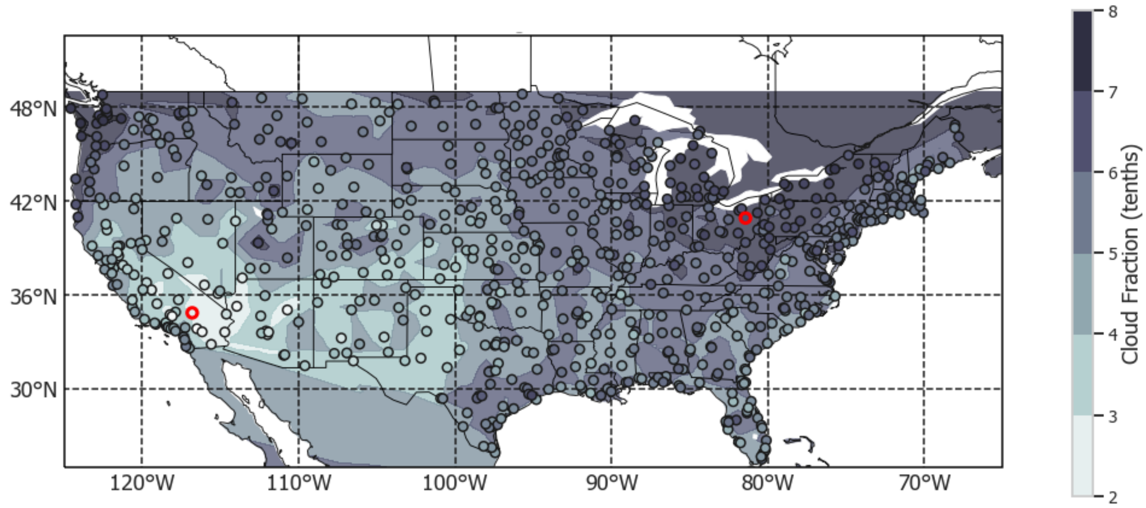

Figure 3.4 **1991-2005 Year Averaged Cloud Cover:** The annual averaged cloud cover in tenths, adapted from Kafka and Miller 2018 [34]. Plotted the same way as fig. 3.3.

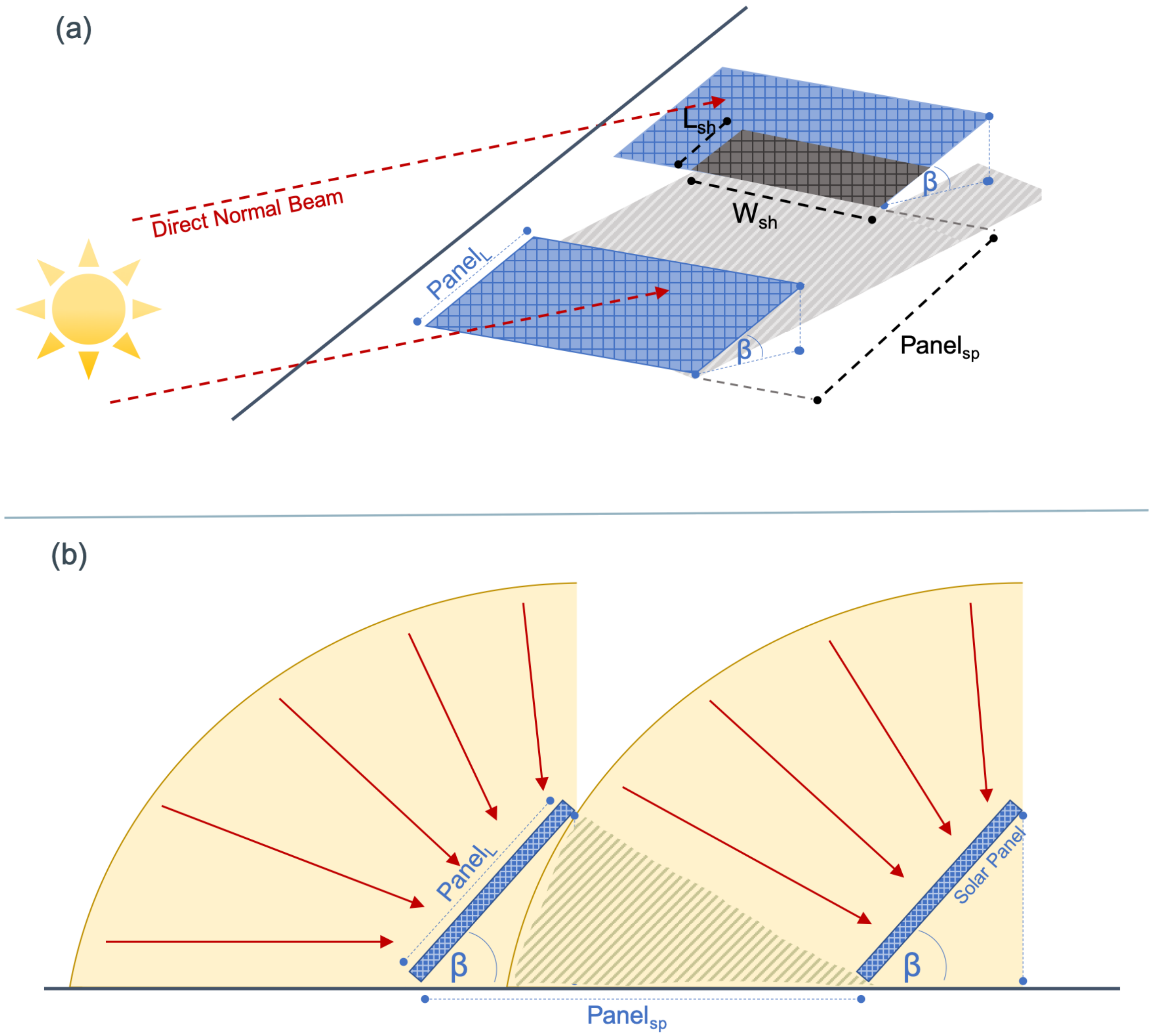

Figure 3.5 **Diagram Showing Solar Array Inter-Row Effects:** Panel (a) illustrates the lengths and angles associated with inter-row shadowing effects when a shadow from a solar panel with tilt, β, is long enough to be projected onto the solar panel behind. Panel (b) illustrates the concept of inter-row masking of the diffuse field. The first row of the solar array has an uninterrupted view of the diffuse field in front of it, while part of the diffuse field as seen from the second row is masked from the row in front. $Panel_L$ is the length of the solar panel and $Panel_{sp}$ is the row spacing from figure 3.6.

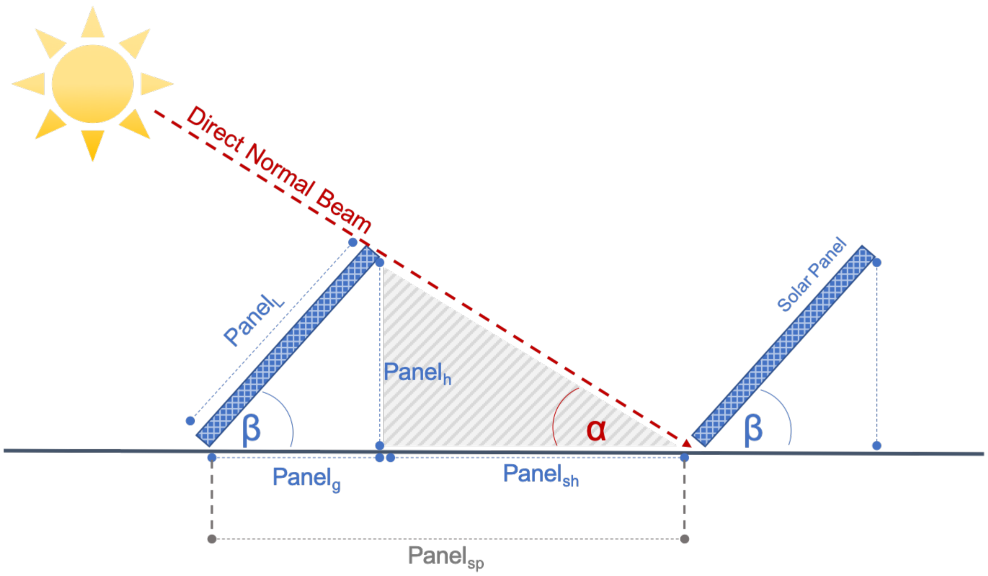

Figure 3.6 **Geometry of Solar Panel Shadowing:** The various angles associated with the shadow cast behind a solar panel with tilt, β, when the sun is at a solar elevation angle α. $Panel_L$ is the length of the solar panel, $Panel_g$ is the projection of the solar panel along the ground, $Panel_h$ is the height from the ground to the top of the tilted solar panel, $Panel_{sh}$ is the ground length of the shadow cast behind the solar panel, and $Panel_{sp}$ is the sum of $Panel_g$ and $Panel_{sh}$, or the panel spacing length.

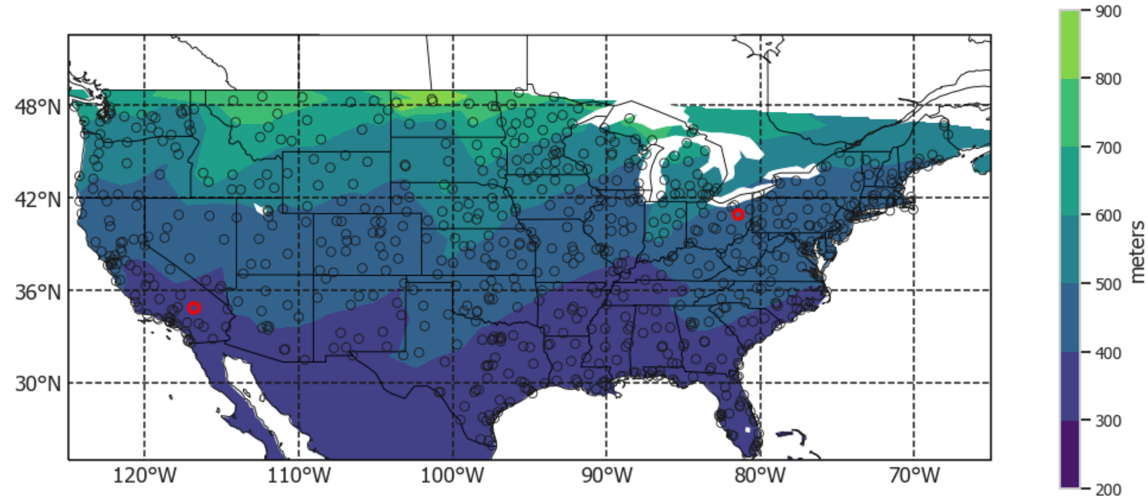

Figure 3.7 **Theoretical Footprint of a 100-Row Solar Panel Array using the Optimum Tilt Angle:** The length of ground space in meters needed to house a 100-row solar panel array where all panels are tilted at the single optimum tilt angle, as shown in figure 3.3. The spacing between rows was determined by the shadow length behind a tilted solar panel at 10:00 AM local time December 21, the winter solstice. Plotted the same way as figure 3.3.

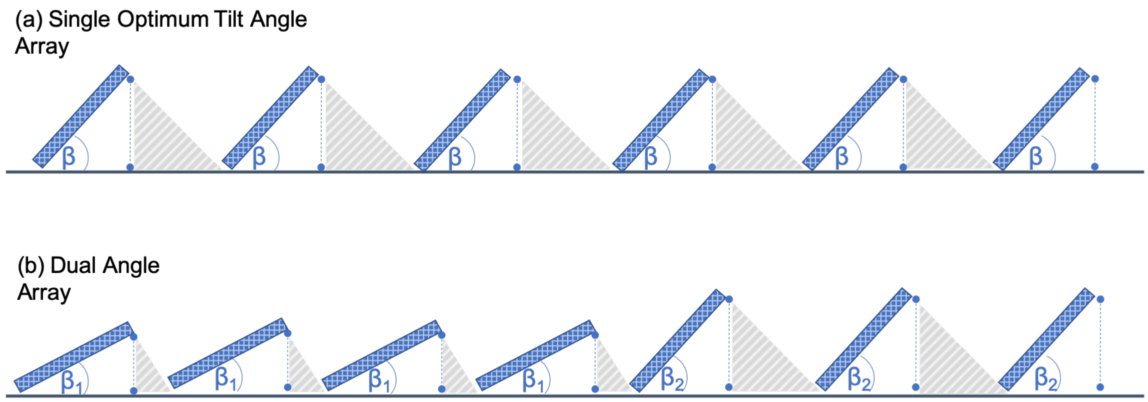

Figure 3.8 **Diagram Showing Single Angle Array Versus Dual Angle Array:** An idealized cartoon showing the number of rows that would fit in a standard single angle array (a) versus the number of rows that would fit by adapting a dual angle system. In this case, more rows of panels tilted at a lower angle could fit in the same space compared to panels tilted at the original angle as the shadow length behind the lower panel is much shorter. Drawing is not to scale but is designed to visualize a dual angle array. The solar panels are represented by the blue rectangles and the resulted shadow is depicted by the light gray triangles, assuming the light source is located to the left.

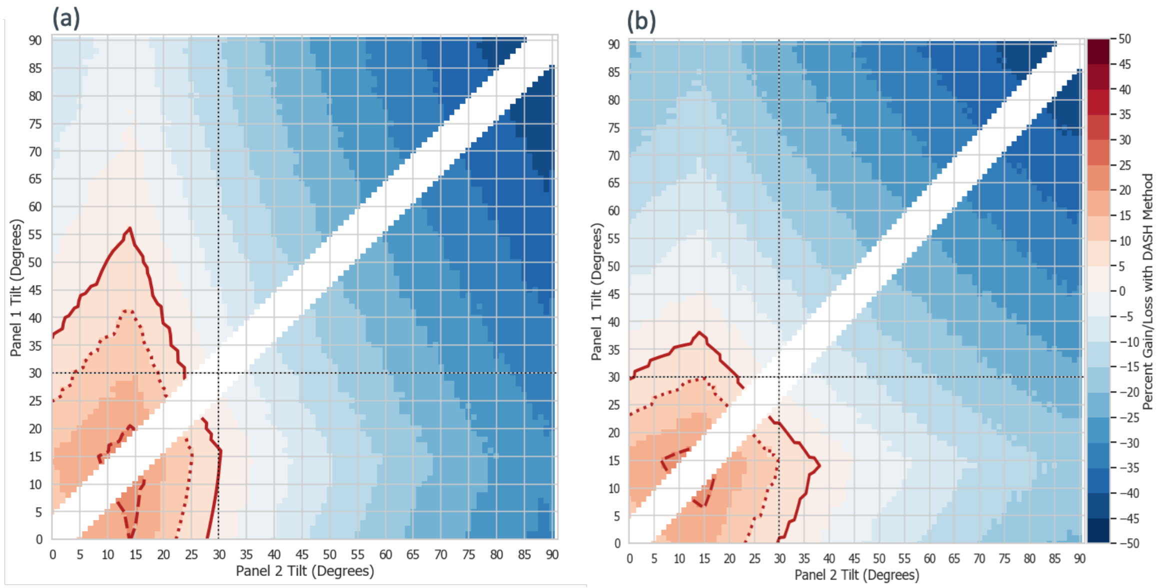

Figure 3.9 **Percent Gain or Loss of F_{TOT} for Every Dual Angle Combination for Barstow, CA:** The resultant percent gain/loss in array-wide incident solar energy ($F_{TOT,array}$) using every possible combination of β_1 and β_2 for Barstow, CA, when using (a) a 30/70 split between β_1 and β_2 and (b) a 50/50 split between β_1 and β_2. The white diagonal band indicates combinations of angles that are less than or equal to a 5° difference (where DASH isn't calculated). Gains in $F_{TOT,array}$ are shown in shades of red, while losses of $F_{TOT,array}$ are shown in shades of blue. Selected gains of 5, 10, and 20% are shown with the red lines, while the optimum tilt angle is highlighted with the set of dashed black lines.

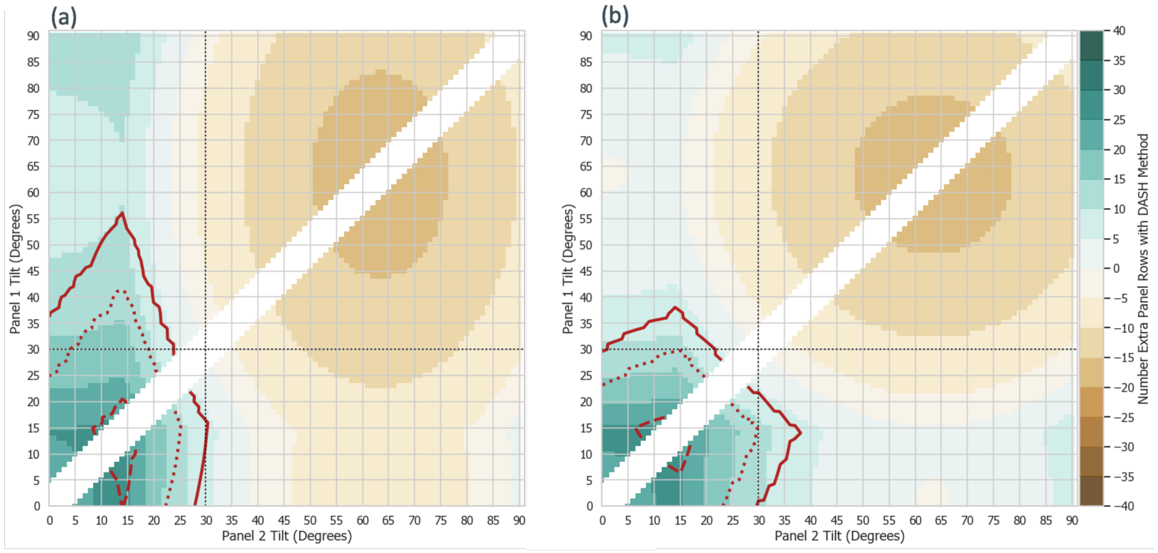

Figure 3.10 **Number of Extra Rows for Every Dual Angle Combination That Fit into the Footprint of a 100-Row Single Angle Solar Array in Barstow, CA:** The number of extra solar panel rows that can fit into the footprint of a 100 row solar array using the single optimum tilt angle for Barstow, CA, when using (a) a 30/70 split between β_1 and β_2 and (b) a 50/50 split between β_1 and β_2. The white diagonal band indicates combinations of angles that are less than or equal to a 5° difference (where DASH is not calculated). The same selected gains (solid red lines) shown in figure 9 are also shown here, while the optimum tilt angle is highlighted with the set of dashed black lines.

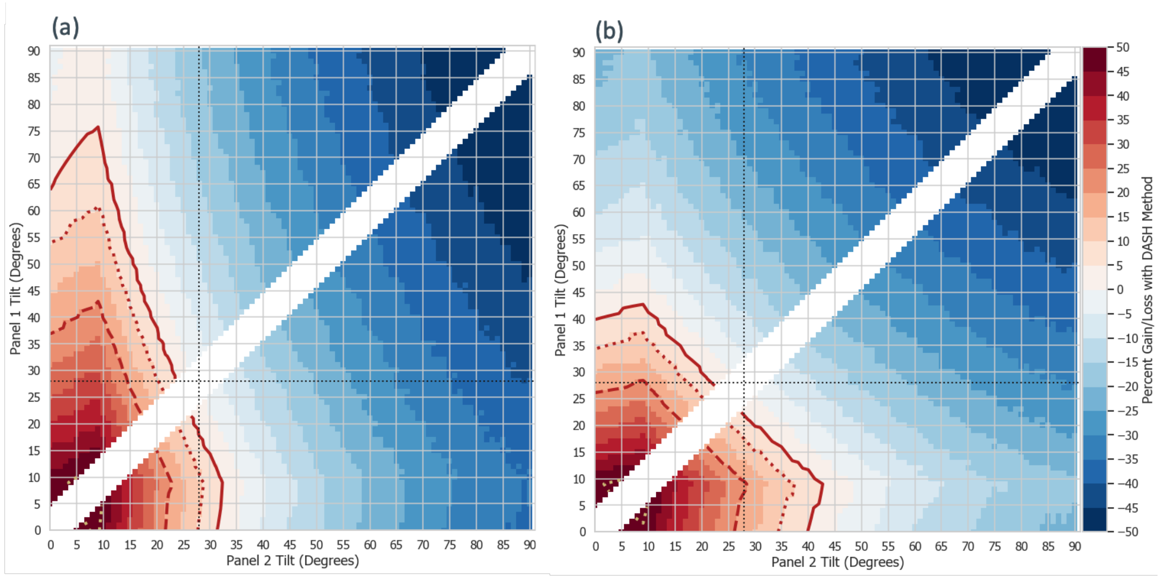

Figure 3.11 **Percent Gain or Loss of F_{TOT} for Every Dual Angle Combination for Akron, OH:** The resultant percent gain or loss in harvested solar energy ($F_{TOT,array}$) using every possible combination of β_1 and β_2 for Akron, OH, when using (a) a 30/70 split between β_1 and β_2 and (b) a 50/50 split between β_1 and β_2. Plotted as in Figure 3.9, but the 50% gain contour is also shown (in yellow).

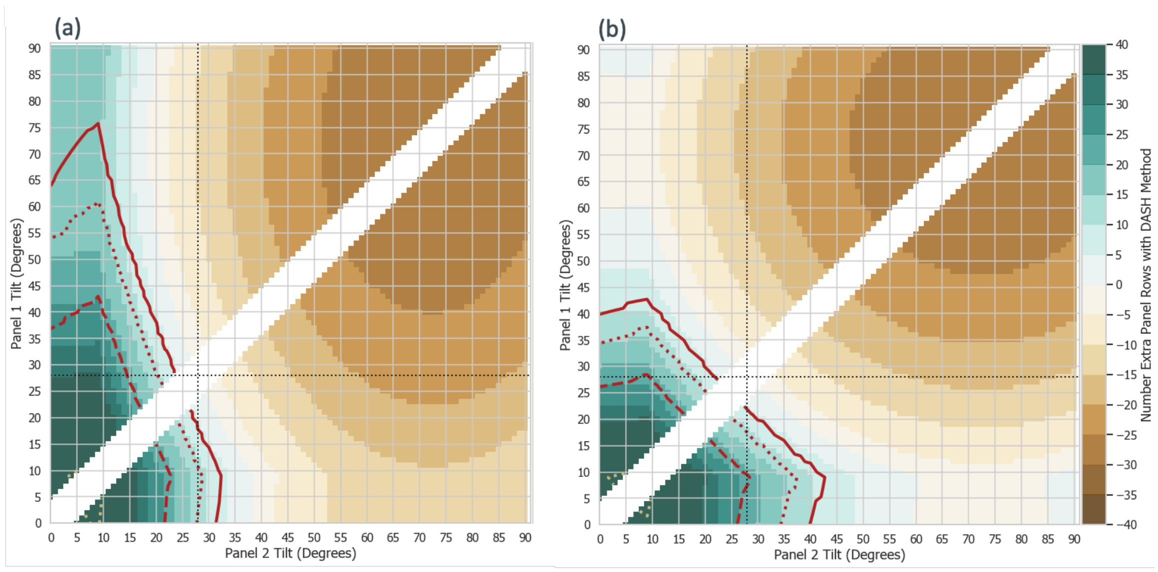

Figure 3.12 **Number of Extra Rows for Every Dual Angle Combination That Fit into the Footprint of a 100-Row Single Angle Solar Array in Akron, OH:** The number of extra solar panel rows that can fit into the footprint of a 100 row solar array using the single optimum tilt angle for Akron, OH, when using (a) a 30/70 split between β_1 and β_2 and (b) a 50/50 split between β_1 and β_2. Plotted as in Figure 3.10.

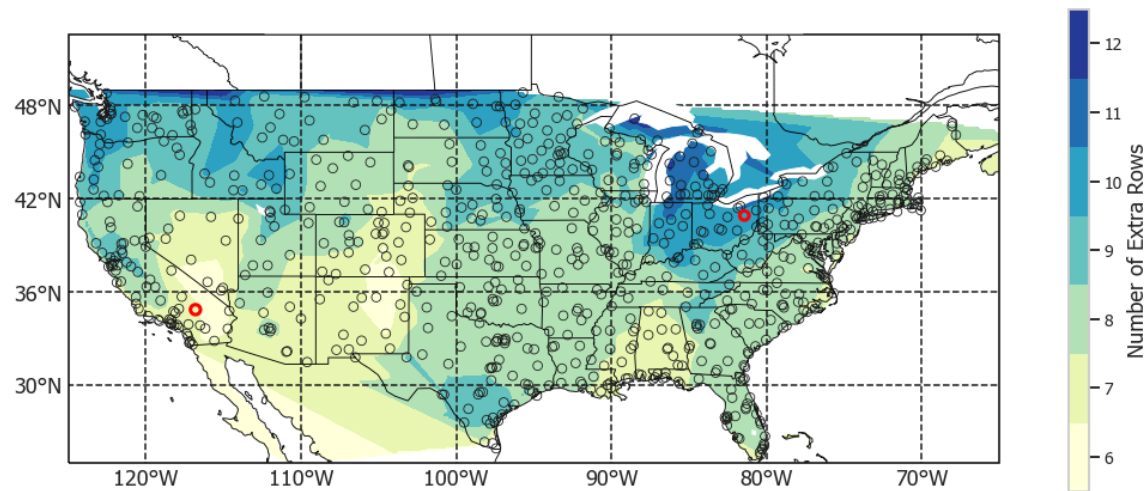

Figure 3.13 **Number of Extra Panel Rows by Tilting All Panels 5° Lower than β_{opt}:** Colors indicate the number of extra panels (exceeding 100) that can fit into the same footprint of a 100-row β_{opt} array when all panel tilts are lowered by 5°.

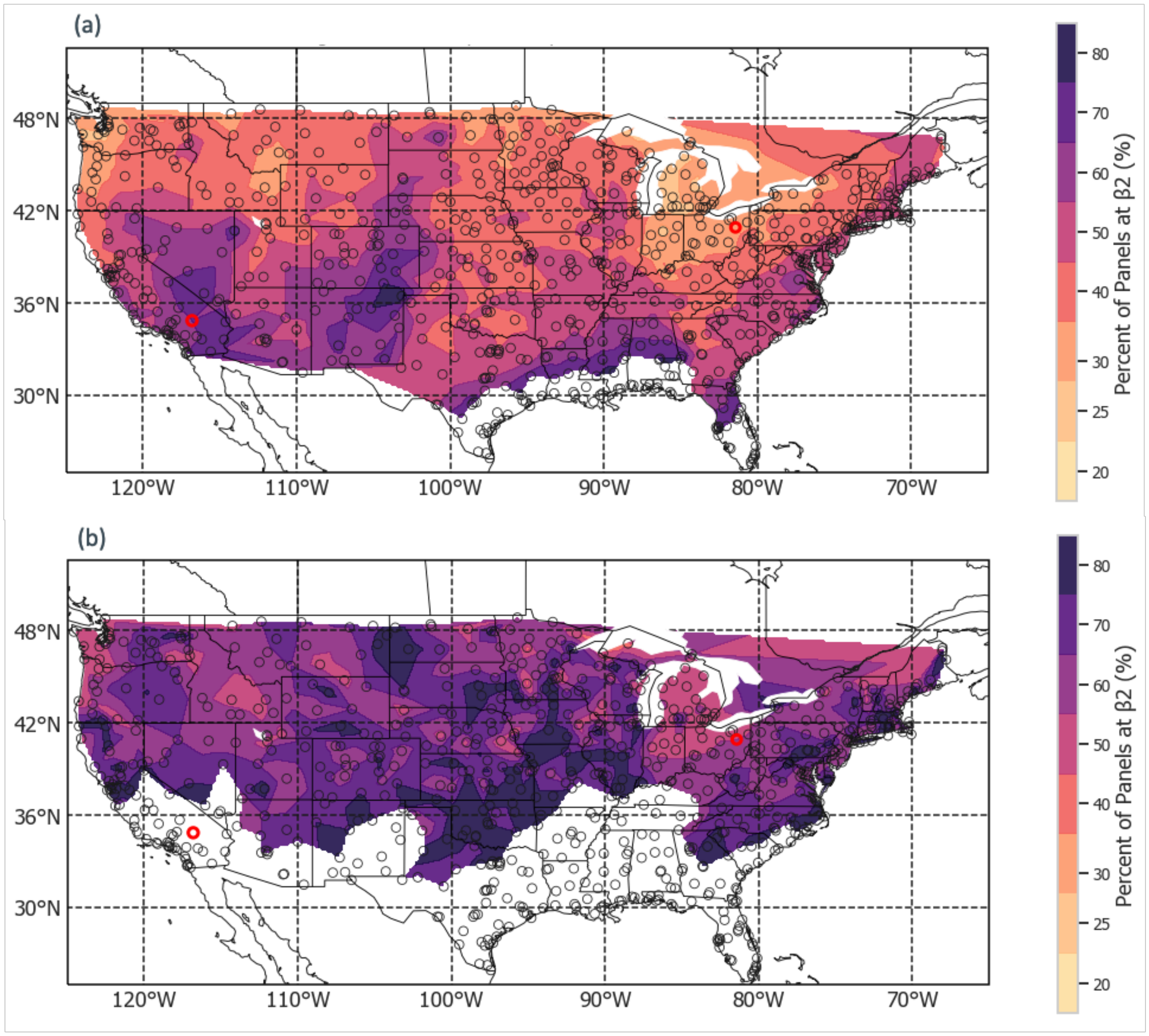

Figure 3.14 **Dash Method**: **Percent of Panel Rows Changed to $\boldsymbol{\beta_2}$ for a 10%/20% Gain in Energy:** Colors indicate the percent of panel rows that needed to be adjusted to β_2 to see (a) a 10% increase and (b) a 20% increase in array-wide incident solar energy and using the fewest possible extra panel rows across the same footprint of a 100-row β_{opt} array.

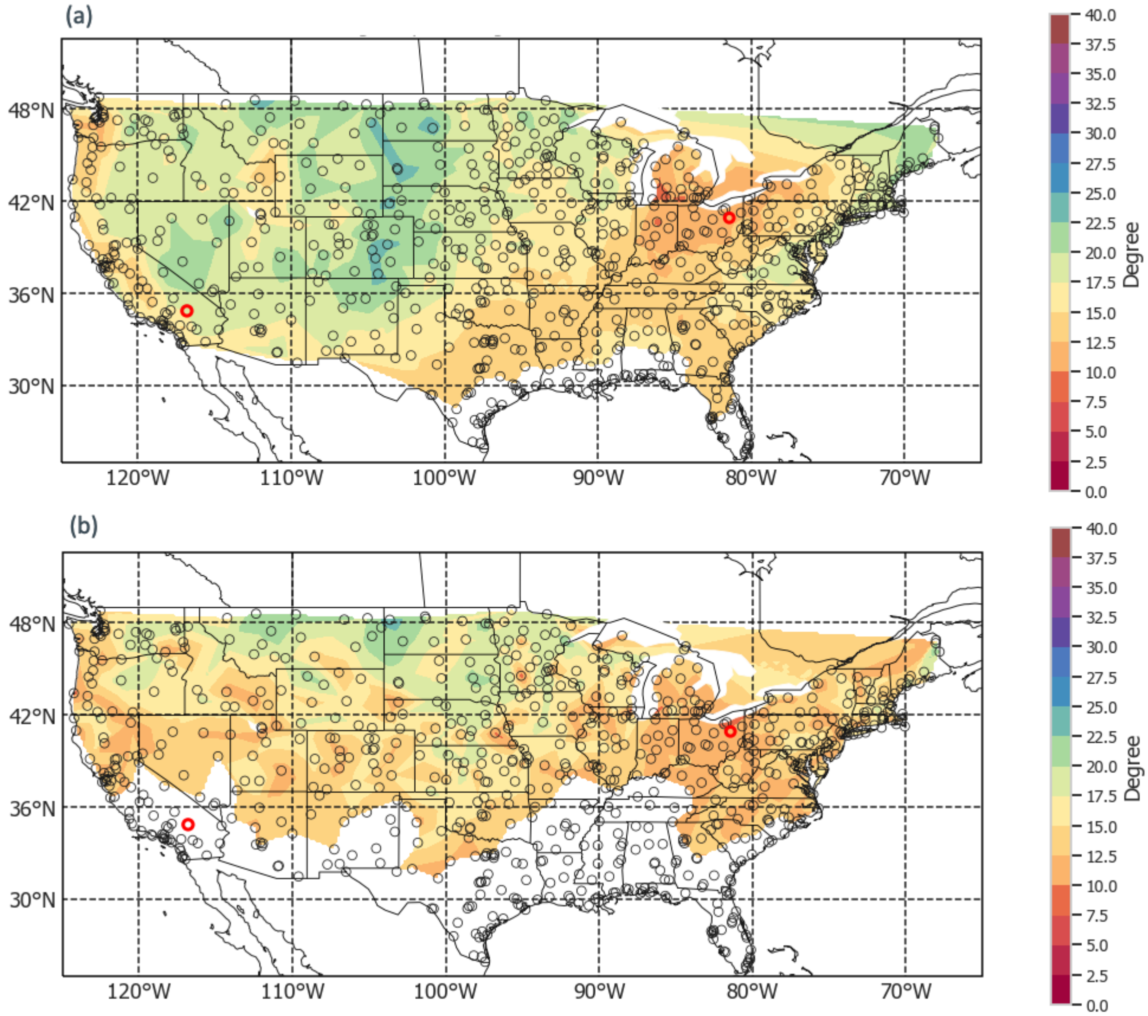

Figure 3.15 **DASH Method**: $\boldsymbol{\beta_2}$ **Angle for a 10%/20% Gain in Energy:** Colors indicate the tilt angle, β_2, necessary to see (a) a 10% increase and (b) a 20% increase in array-wide incident solar energy using the fewest possible extra panel rows across the same footprint of a 100-row β_{opt} array.

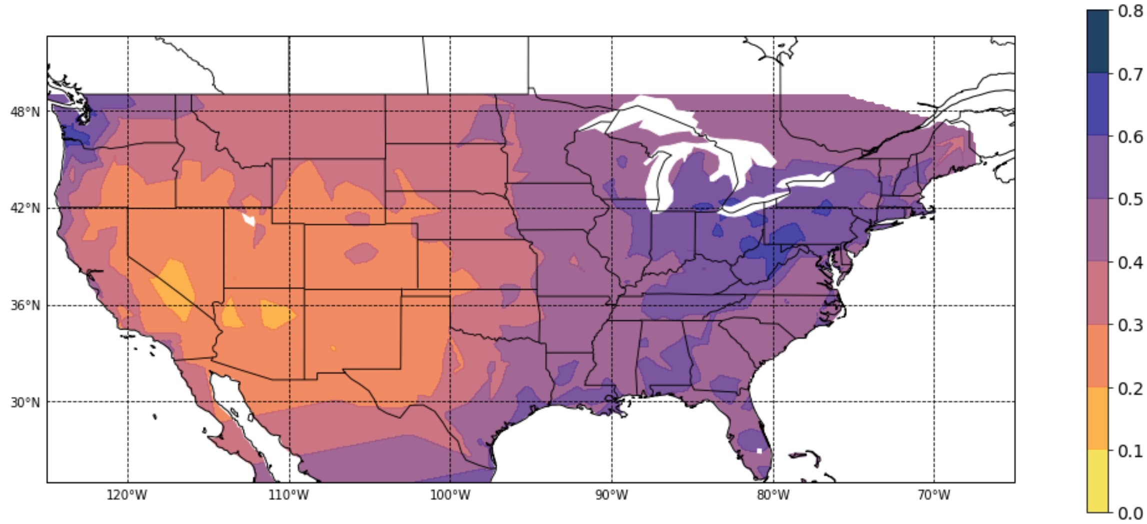

Figure 3.16 **1991–2005 Average Ratio of Diffuse to Direct Radiation:** The average interpolated ratio of diffuse radiation to direct radiation; adapted from Kafka and Miller 2018 [3.34].

Figure 4.1. **Geometry of the Rutgers Solar Carport Canopy:** Photograph showing a side-view of one of the rows of the Livingston Campus Solar Carport Canopy. The photograph has been annotated to show the tilt angle (15°), from horizontal, of one side of the canopy. The other side of the canopy is flat.

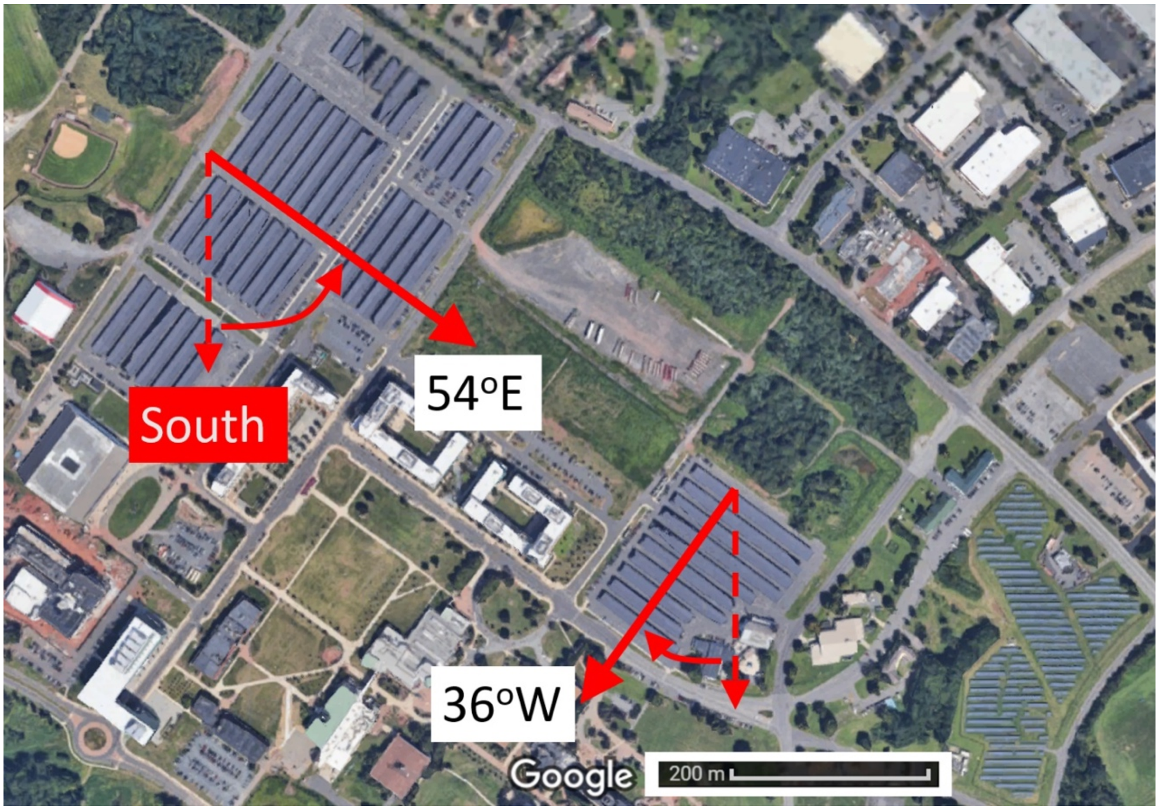

Figure 4.2. **Aerial Map of Livingston Solar Carport Canopies:** Aerial diagram, taken from Google Maps, showing the relative locations of the two different solar carport canopies on Livingston Campus at Rutgers University: The Yellow Lot (upper left) and Lot 105 (lower middle). The photograph has been annotated to point out the azimuth angle of each of the canopies: the Yellow Lot is aimed at 126° (54° less than 180°), or generally ESE and Lot 105 is aimed at 216° (36° more than 180°),, or generally SSW. As a reference, an azimuth angle of 180° would indicate a due southward orientation. A third Rutgers solar array is visible in the lower right corner.

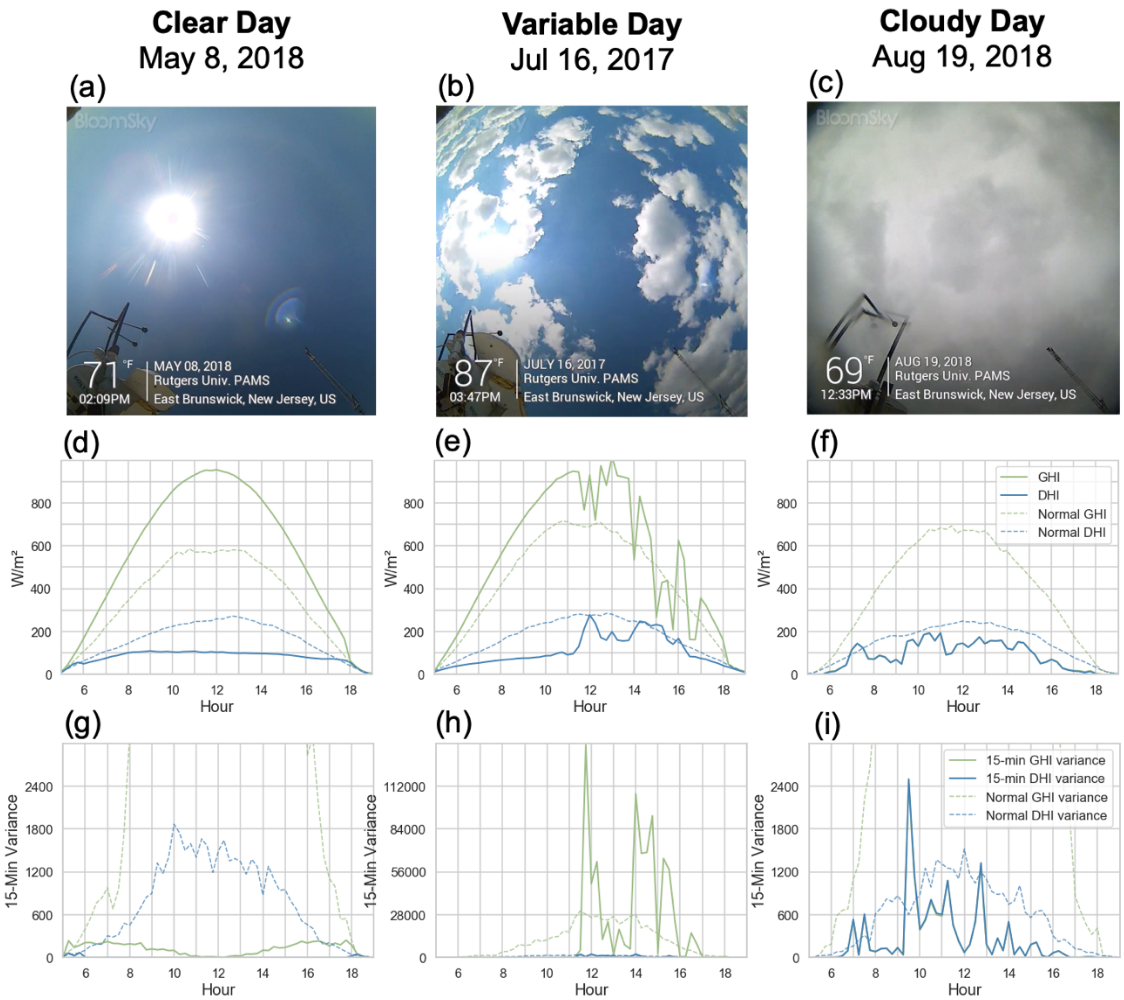

Figure 4.3. **PAM Site Radiation Data of a Clear, Variable, and Cloudy Day:** Ideal examples of a clear day, variable day, and cloudy day. A screenshot showing sky conditions mid-day from the BloomSky instrument at the PAM site are shown in the top row, the observed and monthly mean profiles of 15-minute GHI and DHI are shown in the middle row and the observed and monthly mean profiles of 15-minute GHI and DHI variance are shown in the bottom row GHI is plotted in green, DHI is plotted in blue, observed profiles are plotted with solid lines, and monthly mean profiles are plotted with dashed lines. Please note the difference in scale between panel (h) compared to panels (g) and (i).

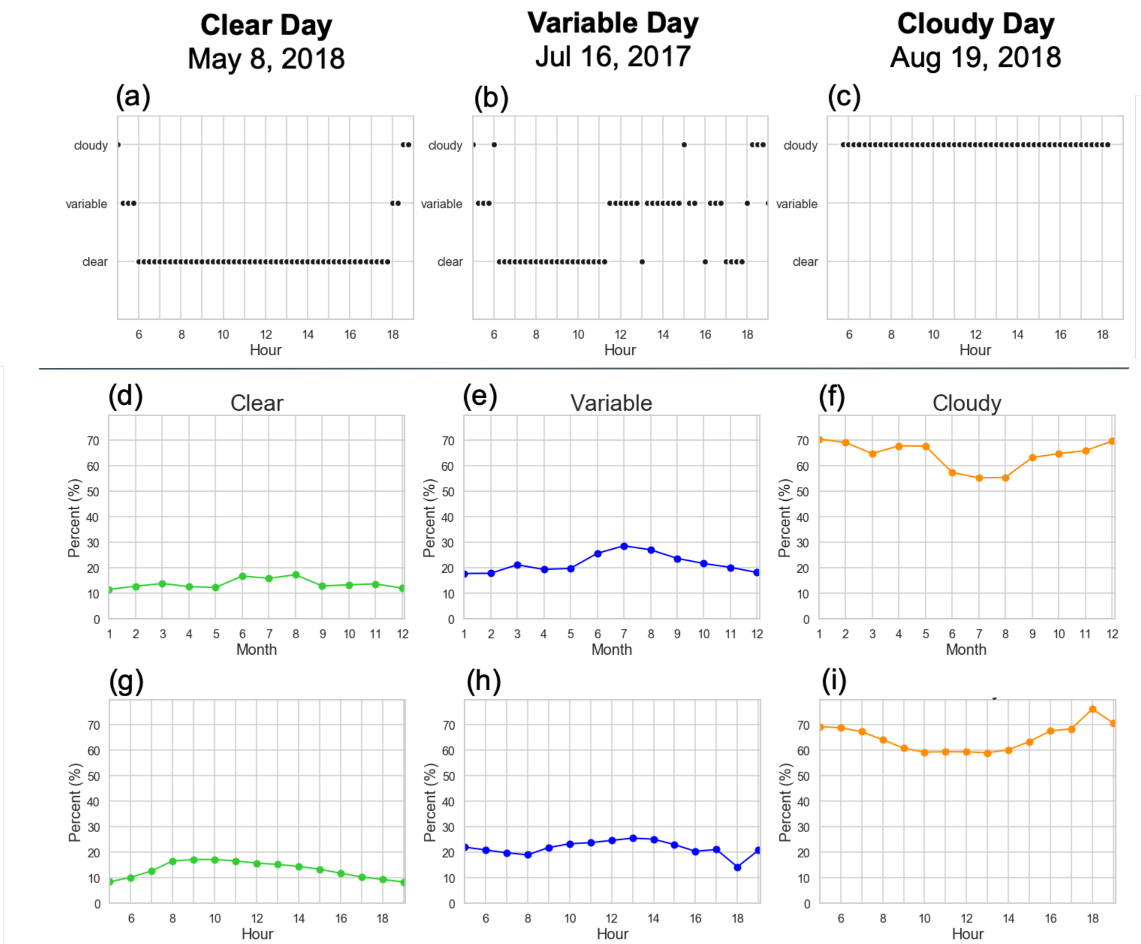

Figure 4.4. **Sky Cover Algorithm Output for a Clear, Variable, and Cloudy Day:** For each ideal example of a clear, variable, and cloudy day in Figure 4.3, the 15-minute output from the sky cover algorithm described in section 4.3.1 is plotted (top row), while the middle row displays the percent of 15-minute observations that were classified in each sky cover bin each month and the bottom row displays the percent of 15-minute observations that were classified in each sky cover bin per hour of the day.

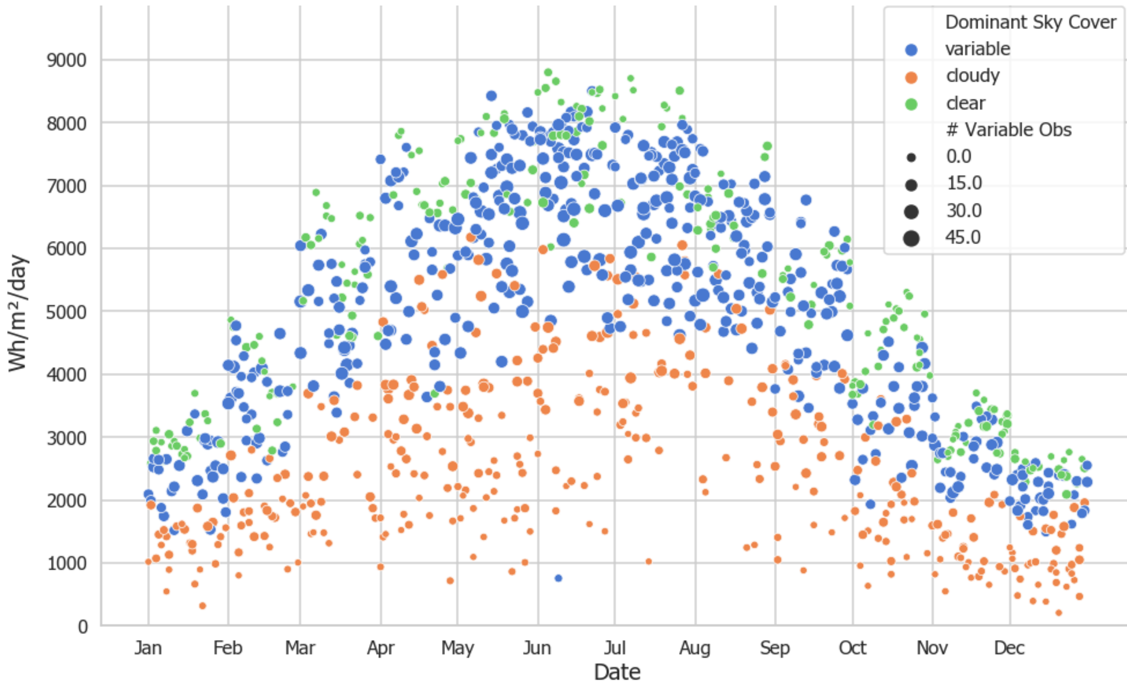

Figure 4.5. **Daily Integrated GHI at the PAM Site binned into Dominant Sky Cover:** Daily integrated totals of GHI constructed from observations at the PAM Site during the entire period of record in section 4.2.2. Each daily sum is reported in units of Wh/m^2/day and is binned according to the daily dominant sky cover algorithm described in section 4.3.1. Variable days are represented by blue dots, cloudy days are represented by orange dots, and clear days are represented by green dots. The size of the dot reflects the number of 15-minute observations in a day that were classified as variable.

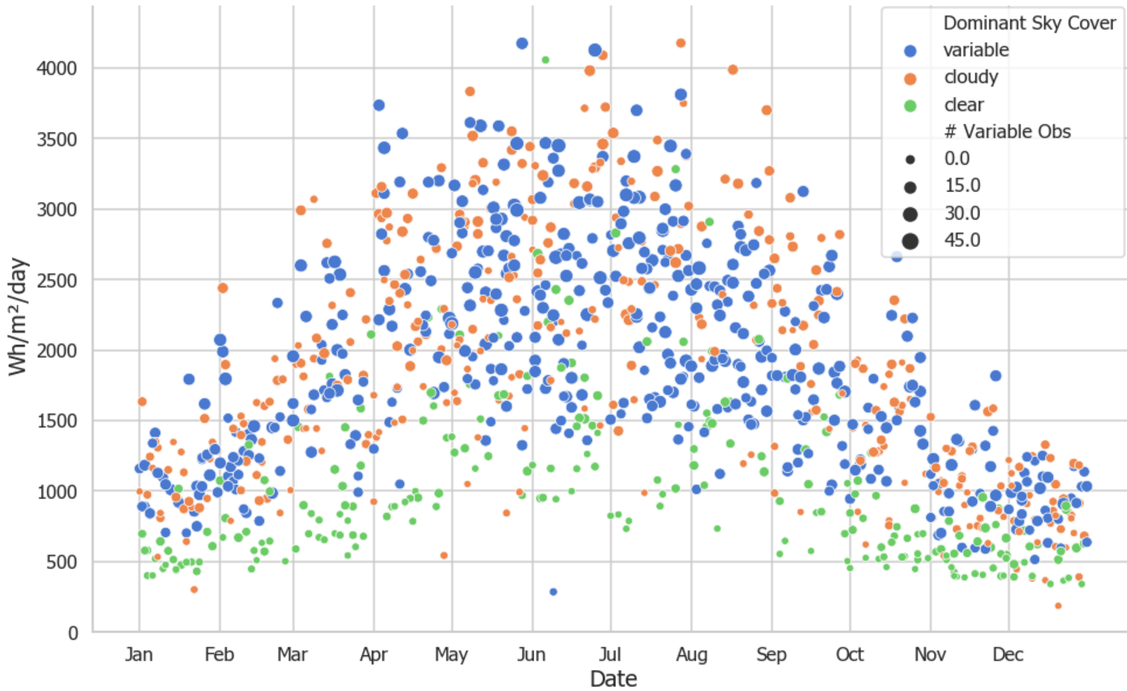

Figure 4.6. **Daily Integrated DHI at the PAM Site binned into Dominant Sky Cover:** Daily integrated totals of DHI constructed from observations at the PAM Site during the entire period of record in section 4.2.2. Each daily sum is reported in units of Wh/m^2/day and is binned according to the daily dominant sky cover algorithm described in section 4.3.1. Plotted the same way as figure 4.5.

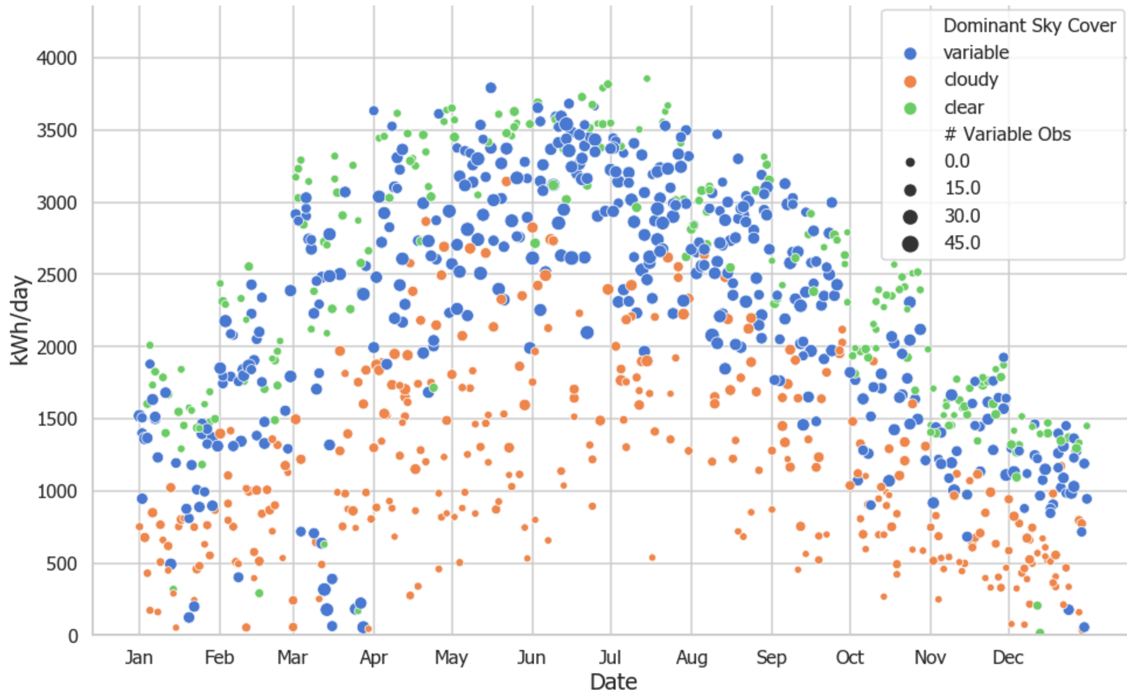

Figure 4.7. **Daily Integrated Inverter Averaged Solar Canopy Data binned into Dominant Sky Cover:** Daily integrated totals showing the average output from a single inverter across both solar canopies during the entire period of record in section 4.2.1. Each daily sum, in units of kWh/day, is calculated using the 15-minute output across a single inverter and is binned according to the daily dominant sky cover algorithm described in section 4.3.1. The total canopy output can be extrapolated by multiplying by the number total inverters (14). Plotted the same way as figure 4.5.

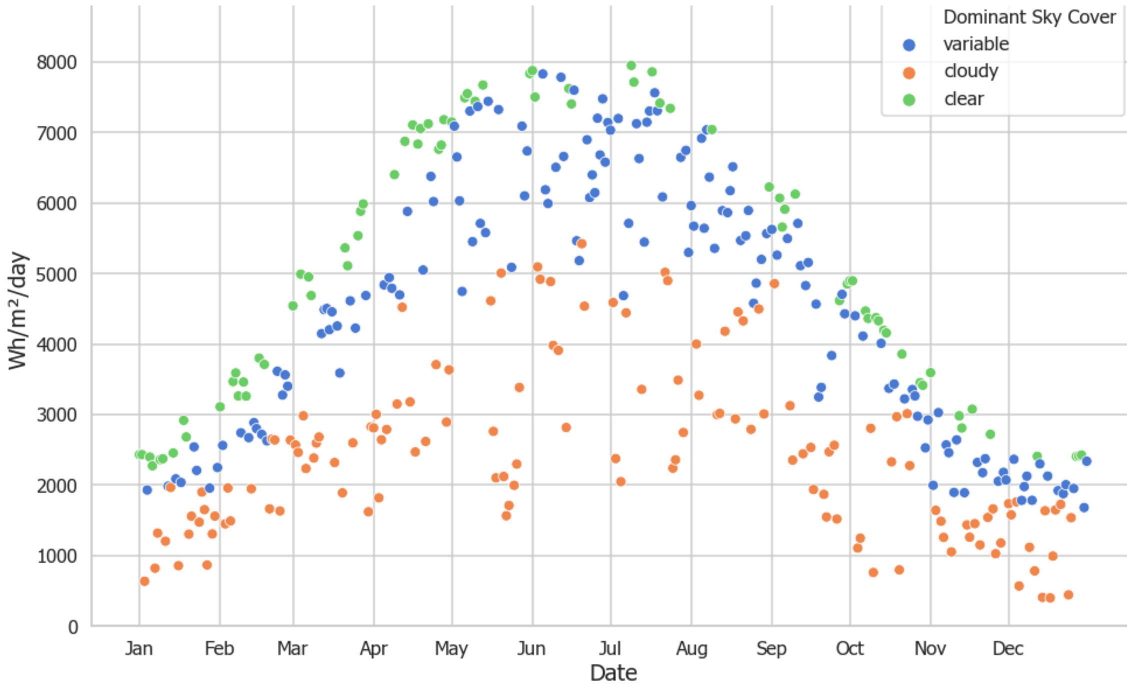

Figure 4.8. **Daily Integrated TMY Solar Data from PVWATTS binned into Dominant Sky Cover:** Daily integrated totals of GHI using typical meteorological year (TMY) data output from PVWATTS. Each daily sum is reported in units of Wh/m^2/day and is binned according to the daily dominant sky cover algorithm. Plotted the same way as figure 4.5.

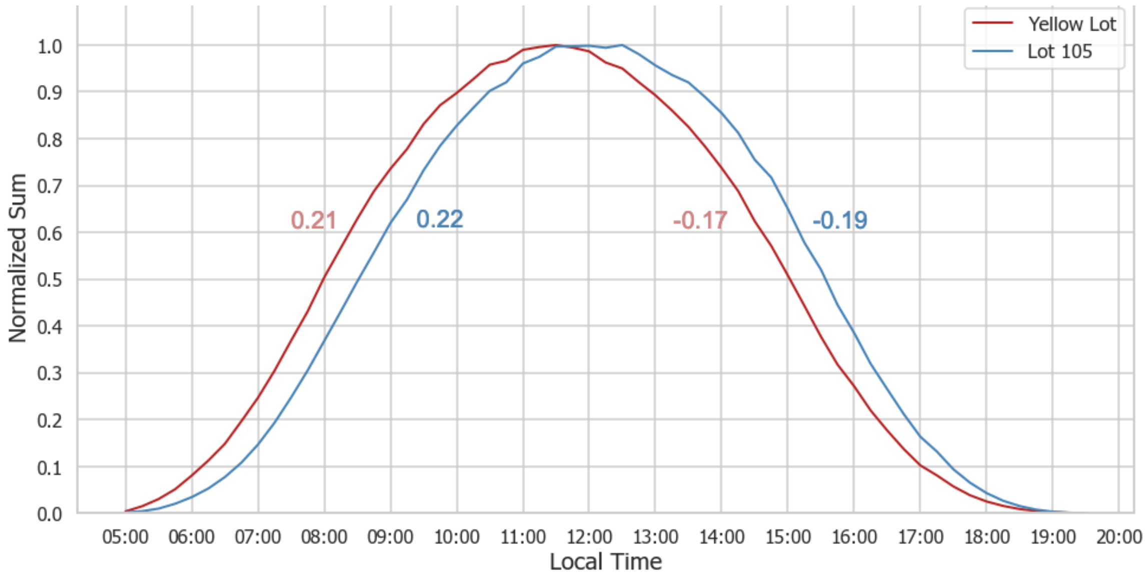

Figure 4.9. **Normalized Daily Solar Canopy Output on Clear Days:** A subset of the solar canopy inverter data on clear days was created by using the dominant cloud cover algorithm described in section 4.3.1 and was then separated by Lot 105 and The Yellow Lot. Hourly values for each parking lot were summed and the peak of the total was normalized to 1. The slope of each profile between 7:00 AM and 10:00 AM and also between 2:00 PM and 5:00 PM are also displayed.

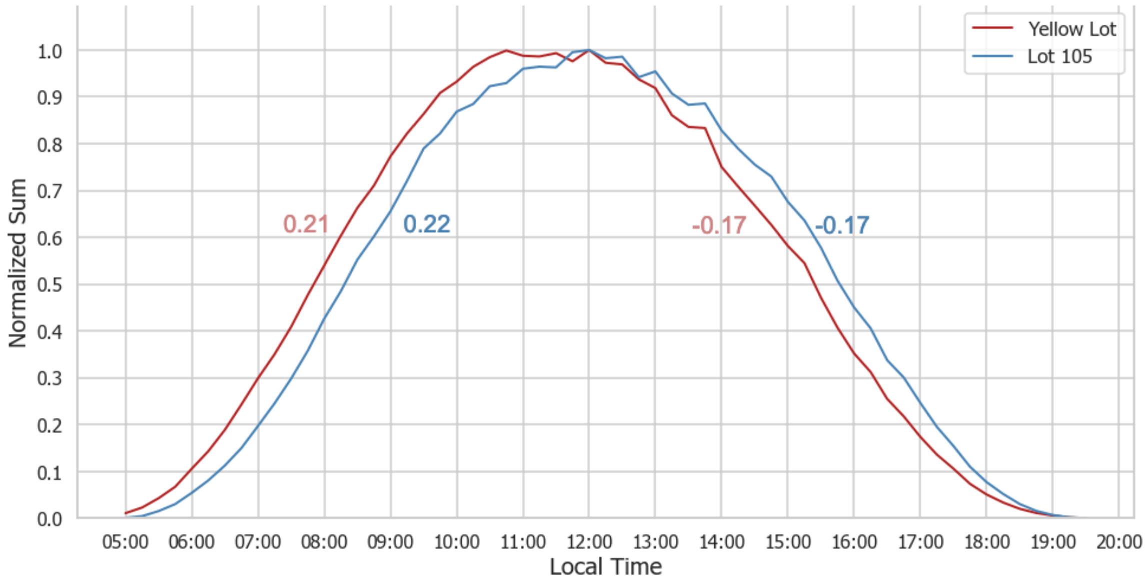

Figure 4.10. **Normalized Daily Solar Canopy Output on Variable Days:** Plotted the same way as figure 4.9 but showing output for variable days.

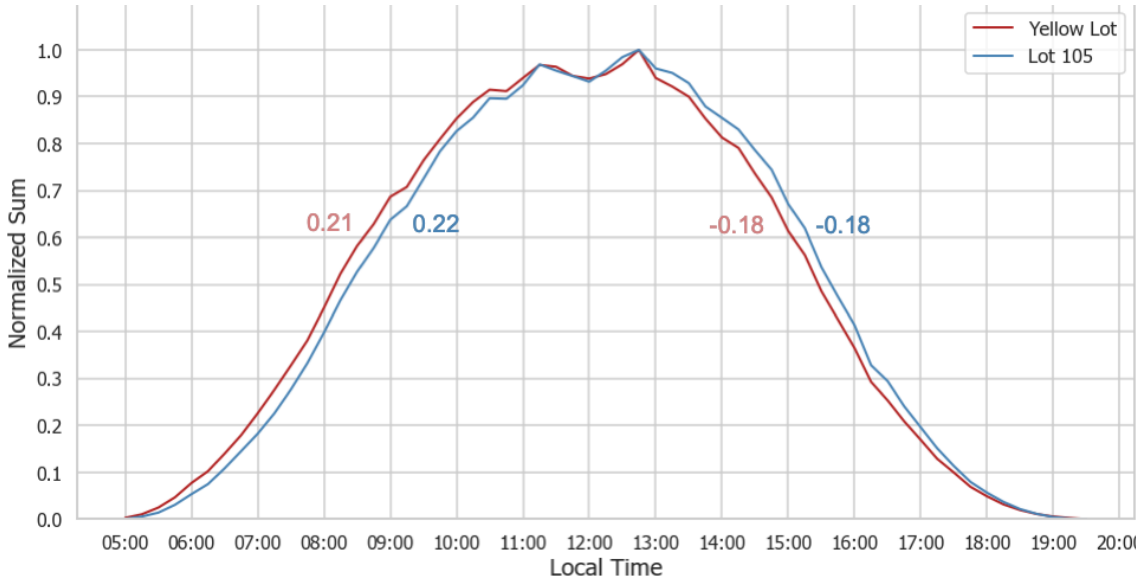

Figure 4.11. **Normalized Daily Solar Canopy Output on Cloudy Days:** Plotted the same way as figure 4.9 but showing output for Cloudy days.

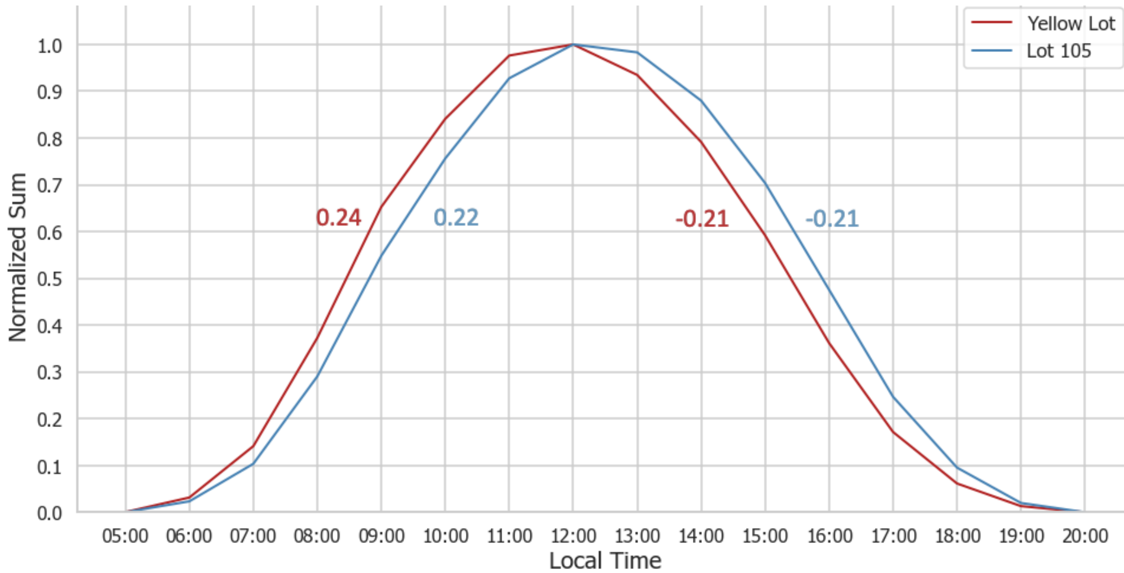

Figure 4.12. **Hourly Irradiance Input Projected for the Yellow Lot and Lot 105 for Clear Days.** Annual hourly averaged irradiance combining flat and tilted sections of the Yellow Lot and Lot 105 based on TMY3 hourly data for DNI and DHI. The slope was also calculated by taking the steepest part of each curve and including the 4 adjacent times.

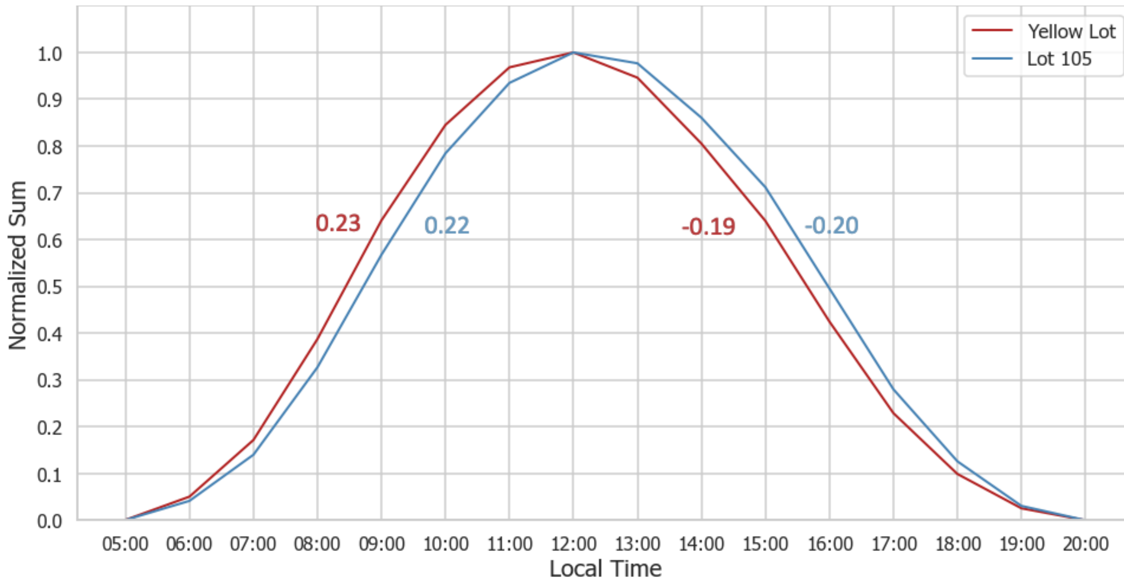

Figure 4.13. **Hourly Irradiance Input Projected for the Yellow Lot and Lot 105 for Variable Days.** Annual hourly averaged irradiance combining flat and tilted sections of the Yellow Lot and Lot 105 based on TMY3 hourly data for DNI and DHI. Slopes are shown as calculated in figure 4.12.

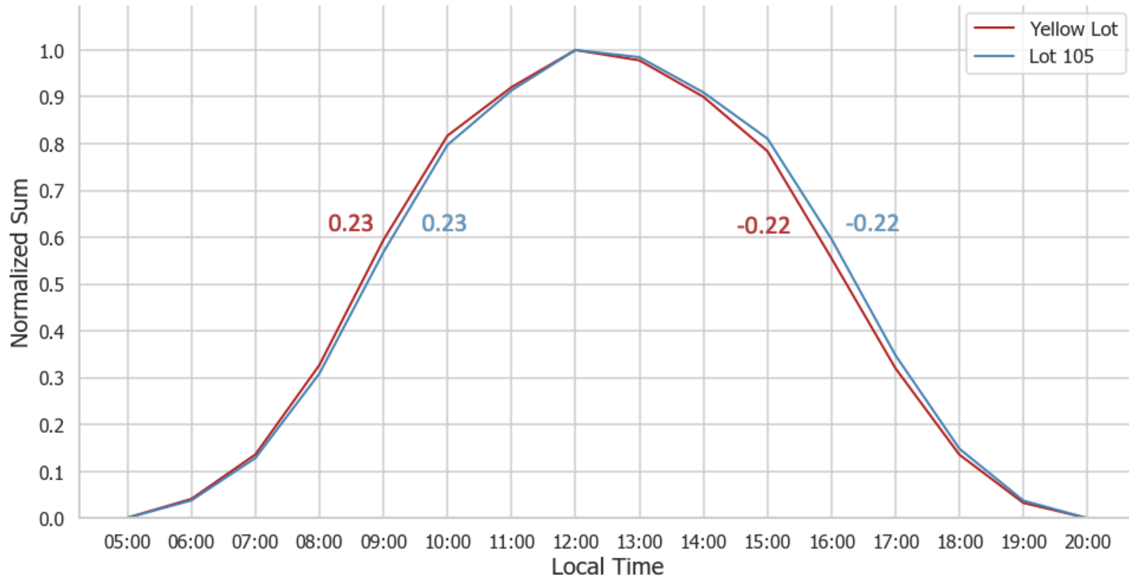

Figure 4.14. **Hourly Irradiance Input Projected for the Yellow Lot and Lot 105 for Cloudy Days.** Annual hourly averaged irradiance combining flat and tilted sections of the Yellow Lot and Lot 105 based on TMY3 hourly data for DNI and DHI. Slopes are shown as calculated in figure 4.12.

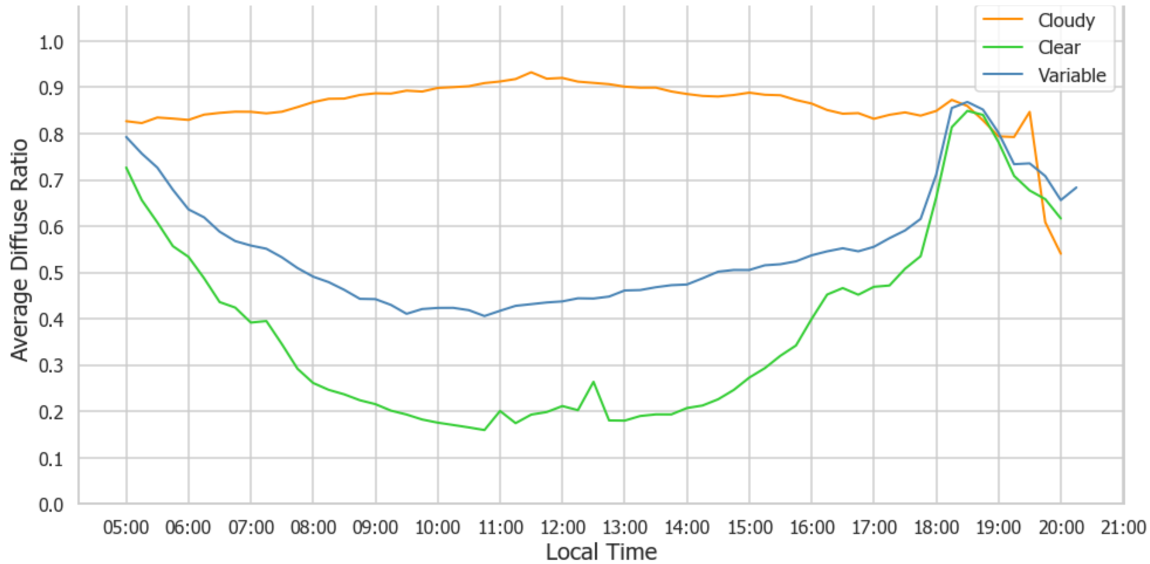

Figure 4.15. **Hourly Diffuse Radiation Ratio for Cloudy, Clear, and Variable Days.** Hourly averaged ratios of DHI to GHI from the PAM site observational data was binned into cloudy, clear, and variable days according to the sky cover algorithm described in section 4.3.1. The average was taken across the entire dataset for each hour. Cloudy data is shown in orange, variable data is shown in blue, and clear data is shown in green.

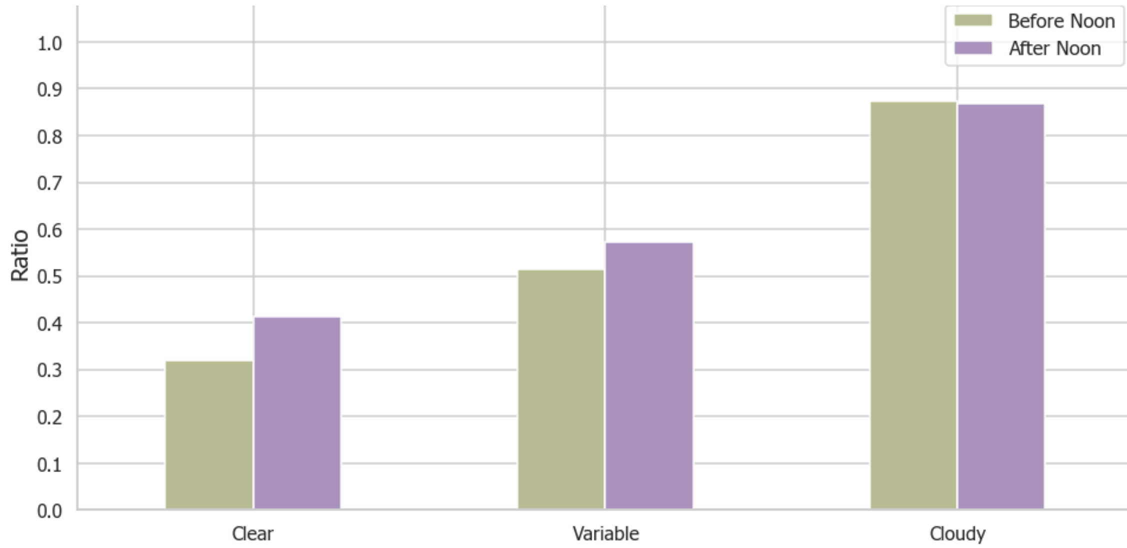

Figure 4.16. **The Average Diffuse Radiation Ratio Before and After Noon for Cloudy, Clear, and Variable Days.** Hourly averaged ratios of DHI to GHI from the PAM site observational data was binned into cloudy, clear, and variable days according to the sky cover algorithm described in section 4.3.1. The average from sunrise to 12:00 noon is shown by the green bars, while the average from 12:00 noon to sunset is shown by the purple bars. These bars represent the average component of diffuse radiation during the first half of the day and the second half of the day for each of the three sky condition bins.

REFERENCES

Chapter 1

[1.1] Trancik, J. E. Renewable energy: Back the renewables boom. *Nature*, **2014**, 507, 300-302.

[1.2] International Energy Association, Renewable Capacity Growth Worldwide Stalled in 2018 after Two Decades of Strong Expansion, <https://www.iea.org/newsroom/news/2019/may/renewable-capacity-growth-worldwide-stalled-in-2018-after-two-decades-of-strong-e.html>, accessed 7/1/2019.

[1.3] Solar Energy Industries Association, Solar Industry Research Data, <https://www.seia.org/solar-industry-research-data>, accessed 8/24/19.

[1.4] Solar Energy Industries Association, Solar Market Insight Report 2019 Q2, <https://www.seia.org/research-resources/solar-market-insight-report-2019-q2>, accessed 9/17/19.

[1.5] Solar Energy Industries Association, U.S. Solar Market Insight September 17, 2019, <https://www.seia.org/us-solar-market-insight>, accessed 9/17/19.

[1.6] Trancik, J. E., and Cross-Call, D. Energy technologies evaluated against climate targets using a cost and carbon trade-off curve. *Environ. Sci. Technol.*, **2013**, 47, 6673-6680.

[1.7] Fu, R., Feldman, D., and Margolis, R. U.S. Solar Photovoltaic System Cost Benchmark: Q1 2018. Golden, CO: National Renewable Energy Laboratory

[1.8] Kavlak, G., McNerney, J., Trancik, J. E. Evaluating the causes of cost reduction in photovoltaic modules. *Energy Policy,* **2018**, 123, 700-710.

[1.9] Comello, S. and Reichelstein, S. The U.S. investment tax credit for solar energy: Alternatives to the anticipated 2017 step-down. *Renewable and Sustainable Energy Reviews*, **2015**, 55, 591-602.

[1.10] Comello, S., Reichelstein, S., and Sahoo, A. The road ahead for solar PV power. *Renewable and Sustainable Energy Reviews*, **2018**, 92, 744-756.

[1.11] Solar Energy Industries Association, Performance-Based Incentives, < https://www.seia.org/initiatives/performance-based-incentives>, accessed 9/17/19.

[1.12] U.S. Department of Energy's Energy Efficiency and Renewable Energy, The History of Solar, <https://www1.eere.energy.gov/solar/pdfs/solar_timeline.pdf>, accessed 6/25/19.

[1.13] Clean Technica, New Solar Cell Efficiency Record Set At 46%, <https://cleantechnica.com/2014/12/03/new-solar-cell-efficiency-record-set-46/>, accessed 9/17/2019.

[1.14] U.S. Department of Energy: Office of Energy Efficiency & Renewable Energy, Crystalline Silicon Photovoltaics Research, <https://www.energy.gov/eere/solar/crystalline-silicon-photovoltaics-research>, accessed 6/20/19.

[1.15] Al-Tameemi, M.A. and Chukin, V.V. Global water cycle and solar activity. *J. Atmos Sol Terr Phys*, **2016**, 142, 55-59.

[1.16] Kumar, L., Skidmore, A. K., and Knowles, E. Modelling topographic variation in solar radiation in a GIS environment. *Int. J. of Geographical Information Science*. **1997**, 11(5), 475-497.

[1.17] Duguay, C. R. Radiation modelling in mountainous terrain: review and status. *Mountain Research and Development*, **1993**, 13, 339-357.

[1.18] Black, J. N., Bonython, C. W., and Prescott, J. A. Solar radiation and the duration of sunshine. *Quarterly J. of the Royal Meteorological Society*, **1954**, 80(344), 231-235.

[1.19] The Intergovernmental Panel on Climate Change, Reports, <https://www.ipcc.ch/reports/>.

[1.20] Braun, J. E., and Mitchell, J. C. Solar geometry for fixed and tracking surfaces. *Solar Energy*, **1983**, 31(5), 439-444.

[1.21] Liu, B. Y. H., and Jordan, R. C. The interrelationship and characteristic distribution of direct, diffuse, and total solar irradiation. *Solar Energy*, **1960**, 4(3), 1-19.

[1.22] Lam, J. C. and Li, D. H. W. Correlation between global solar radiation and its direct and diffuse components. *Building and Environment*, **1996**, 31(6), 527-535.

[1.23] Ehnberg, J. S. G., and Bollen, M. H. J. Simulation of global solar radiation based on cloud observations. *Solar Energy*, **2005**, 78(2), 157-162.

[1.24] Nielsen, L., Prahm, L., Berkowicz, R., and Conradsen, K. Net incoming radiation estimated from hourly global radiation and/or cloud observations. *J. Climatology*, **1981**, 1, 255-272.

[1.25] Albizzati, E., Rossetti, G., and Alfano, O. Measurements and predictions of solar radiation incident on horizontal surfaces at Santa Fe, Argentina (31.39'S, 60.43'W). *Renewable Energy*, **1997**, 4, 469-478.

[1.26] Lazaroiu, G. C., Longo, M., Roscia, M., and Pagano, M. Comparative analysis of fixed and sun tracking low power PV systems considering energy consumption. *Energy Conversion and Management*, **2015**, 92, 143-148.

[1.27] Eke, R. and Senturk, A. Performance comparison of a double-axis sun tracking versus fixed PV system. *Solar Energy*, **2012**, 86(9), 2665-2672.

[1.28] Koussa, M., Cheknane, A., Hadji, S., Haddadi, M., and Noureddine, S. Measured and modeled improvement in solar energy yield from flat plate photovoltaic systems utilizing difference tracking systems and under a range of environmental conditions. *Applied Energy*, **2011**, 88, 1756-1771.

[1.29] Al-Mohamad, A. Efficiency improvements of photo-voltaic panels using a sun-tracking system. *Applied Energy*, **2004**, 79(3), 345-354.

[1.30] Abdallah, S. and Nijmeh, S. Two axes sun tracking system with PLC control. *Energy Conversion and Management*, **2004**, 45, 1931-1939.

[1.31] Torres, D.J.; Crichigno, J. Influence of reflectivity and cloud cover on the optimal tilt angle of solar panels. *Resources* **2015**, 4, doi: 10.3390/resources4040736

[1.32] Matallah, T., Alimi, S. E., Nassrallah, S. B. Performance modeling and investigation of fixed, single, and dual-axis tracking photovoltaic panel in Monastir city, Tunisia. *Renewable and Sustainable Energy Reviews*, **2011**, 15(8), 4053-4066

[1.33] Union of Concerned Scientists; Science for a healthy planet and safer world, solar power plants: large-scale PV, <https://www.ucsusa.org/clean-energy/renewable-energy/solar-power-plants-large-scale-pv>, accessed 9/17/19.

[1.34] U.S. Department of Energy, Agua Caliente, <https://www.energy.gov/lpo/agua-caliente>, accessed 9/17/19.

[1.35] Turney, D., and Fthenakis, V. Environmental impacts from the installation and operation of large-scale solar power plants. *Renewable and Sustainable Energy Reviews*, **2011**, 15(6), 3261-3270.

[1.36] Ong, S., Campbell, C., Denhold, P., Margolis, R., and Heath, G. Land use requirement of solar power plants in the United States. Golden, CO: National Renewable Energy Laboratory, **2013**.

[1.37] Davis, M. A., Heathcote, J. The price and quantity of residential land in the United States. *J. of Monetary Economics*, **2007**, 54(8), 2595-2620.

[1.38] Davis, M. A., and Palumbo, M. G. The price of residential land in large US cities. *J. of Urban Economics*, **2008**, 63(1), 352-384.

[1.39] U.S. Energy Information Administration; Today in energy, U.S. renewable electricity generation has doubled since 2008, <https://www.eia.gov/todayinenergy/detail.php?id=38752>, accessed 9/18/19.

[1.40] U.S. Energy Information Administration; Today in energy, Most utility-scale fixed-tilt solar photovoltaic systems are tilted 20 dgrees-30 degrees,<https://www.eia.gov/todayinenergy/detail.php?id=37372>, accessed 9/18/19.

[1.41] Arnett, J. C., Schaffer, L. A., Rumberg, J. P., and Tolbert, R. E. L. Design, installation, and performance of the ARCO Solar one-megawatt power plant. *Photovoltaic Solar Energy Conference; Proceedings of the Fifth International Conference,* Athens, Greece, 1984.

[1.42] Wenger, H. J., Schaefer, J., Rosenthal, A., Hammond, B., and Schleuter, L. Decline of the Carrisa Plains PV power plant: the impact of concentrating sunlight on flat plates. *Photovoltaic Specialists Conferences*, Las Vegas, Nevada, 1991.

[1.43] Solar Energy Industries Association, Top 10 Solar States, <https://www.seia.org/research-resources/top-10-solar-states-0> , accessed 9/19/19.

[1.44] United States Department of Agriculture, Land Values 2018 Summary, <https://www.nass.usda.gov/Publications/Todays_Reports/reports/land0818.pdf>, accessed 9/19/19.

[1.45] NREL, National solar radiation database, 1991-2010 update. <http://rredc.nrel.gov/solar/old_data/nsrdb/1991-2010/>, [accessed 09.15.17].

Chapter 2

[2.1] International Energy Agency, World Energy Outlook 2017, <http://www.iea.org/weo2017/>, accessed 5/31/2018.

[2.2] Green, M. A.; Emery, K.; King, D. L.; Igari, S.;Warta, W. SHORT COMMUNICATION: Solar cell efficiency tables (version 25). *Prog. Photovolt: Res. Appl*., **2005**, 13: 49-54. doi:10.1002/pip.598

[2.3] National Renewable Energy Laboratory, Photovoltaic Research, <https://www.nrel.gov/pv/>, accessed 5/31/2018.

[2.4] Solar Energy Industries Association, Solar Industry Research Data, <https://www.seia.org/solar-industry-research-data>, accesed 3/15/2018.

[2.5] Torres, D.J.; Crichigno, J. Influence of reflectivity and cloud cover on the optimal tilt angle of solar panels. *Resources* **2015**, 4, doi: 10.3390/resources4040736

[2.6] Lave, M.; Kleissl, J. Optimum fixed orientations and benefits of tracking for capturing solar radiation in the continental United States. *J. Renew. Energy* **2011**, 36, 1145–1152

[2.7] Kelly NA, Gibson TL. Improved photovoltaic energy output for cloudy conditions with a solar tracking system'. *Solar Energy* **2009**; 83:2092-102.

[2.8] Lewis, G. Optimum tilt of solar collector. *Sol. Wind Energy* **1987**, 4, 407–410.

[2.9] Duffie, J.A.; Beckman, W.A. Solar engineering of thermal processes; Wiley: New York, NY, USA, **1980**.

[2.10] Calabrò, E. An algorithm to determine the optimum tilt angle of a solar panel from global horizontal solar radiation. *J. Renew. Energy* **2013**, 1, doi:10.1155/2013/307547.

[2.11] Idowu, O.S.; Olarenwaju, O.M.; Ifedayo, O.I. Determination of optimum tilt angles for collectors in low-latitude tropical regions. *Int. J. Energy Environ. Eng.* **2013**, 4, doi:10.1186/2251-6832-4-29.

[2.12] Darhmaoui, H.; Lahjouji, D. Latitude based model for tilt angle optimization for collectors in the mediterranean region. *Energy Procedia* **2013**, 42, 426–435

[2.13] Wilcox, S.; Gueymard, C.A. Spatial and temporal variability of the solar resource in the United States. In Proceedings of the ASES Solar 2010, Phoeniz, AZ, USA, 17–22 May **2010**.

[2.14] Suri, M., et al. Uncertainties in photovoltaic electricity yield prediction from fluctuation of solar radiation, Proceedings of the 22nd EuPVSEC Conf., Milano, Italy, **2007.**

[2.15] Evrendilek, F., Ertekin, C. Statistical modeling of spatio-temporal variability in monthly-average daily solar radiation over Turkey. *Sensors*, **2007**, 7, 2763–2778

[2.16] Aguado, E. Local-scale variability of daily solar radiation—San Diego County, California. *J. Clim. Appl. Meteorol.,* **1991**, 25, 672–678

[2.17] Gallegos, H.G., Lopardo, R. Spatial variability of the global solar radiation obtained by the solarimetric network in the Argentine Pampa Humeda. *Solar Energy*, **1988**, 40, 397–404

[2.18] Skaggs, R.H., et al. The influence of persistence and variability on the required solar radiation record length. *Solar Energy*, **1982**, 28, 281–287

[2.19] NREL, National solar radiation database, 1991-2010 update. <http://rredc.nrel.gov/solar/old_data/nsrdb/1991-2010/> , [accessed 09.15.17].

[2.20] Maxwell, E.L. "METSTAT" – The solar radiation model used in the production of the national solar radiation database (NSRDB). *Solar Energy*, **1998**, 62, 263-279.

[2.21] Perez, R., P. Ineichen, K. Moore, M. Kmiecik, C. Chain, R. George and F. Vignola. A new operational satellite-to-irradiance model. *Solar Energy*, **2002**, 73, 307-317.

[2.22] Hahn, C.; Rossow, W.B; Warren S.G. ISCCP cloud properties associated with standard cloud types identified in individual surface observations. *J. Climate*, **2013,** 14, 11–28, <https://doi.org/10.1175/1520-0442(2001)014<0011:ICPAWS>2.0.CO;2>

[2.23] Turner, D.D.; Vogelmann, A. M..; Miller, M.A.; and coauthors, Thin liquid water clouds: their importance and our challenge, *Bull. Amer. Met Soc*, **2007**, 88, 177–190

[2.24] Schreiner, A. J.; Unger, D. A.; Menzel, W. P.; Ellrod, G. P.; Strabala, K. I.; Pellet, J. L. A comparison of ground and satellite observations of cloud cover, *Bull. Amer. Met Soc,* **1993**, 74, 1851-1861.

[2.25] Wylie, D. P.; Menzel, W. P. Two years of cloud statistics using VAS, *J. Climate,* **1988**, 2, 380-392.

[2.26] Matuszko, D. Influence of the extent and genera of cloud cover on solar radiation intensity. *Int. J. Climatology,* **2011**, 32, 2403-2414

[2.27] Benghanem, M. Optimization of tilt angle for solar panel: Case study for Madinah, Saudi Arabia. *Applied Energy*, **2011**, 88(4), 1427-1433

Chapter 3

[3.1] Trancik, J. E. Renewable energy: Back the renewables boom. *Nature*, **2014**, 507, 300-302.

[3.2] The International Energy Agency, Renewable capacity growth worldwide stalled in 2018 after two decades of strong expansion, <http://iea.org>, accessed 6/4/2019.

[3.3] Solar Energy Industries Association, Solar Industry Research Data, <https://www.seia.org/solar-industry-research-data>, accessed 8/24/19.

[3.4] Kavlak, G., McNerney, J., Trancik, J. E. Evaluating the causes of cost reduction in photovoltaic modules. *Energy Policy,* **2018**, 123, 700-710.

[3.5] National Renewable Energy Laboratory, Photovoltaic Research, <https://www.nrel.gov/pv/>, accessed 5/31/2018.

[3.6] Trancik, J. E., Cross-Call, D. Energy technologies evaluated against climate targets using a cost and carbon trade-off curve. *Environ. Sci. Technol.*, **2013**, 47, 6673-6680.

[3.7] Davis, M. A., Heathcote, J. The price and quantity of residential land in the United States. *J. of Monetary Economics*, **2007**, 54(8), 2595-2620.

[3.8] Ong, S., Campbell, C., Denhold, P., Margolis, R., and Heath, G. Land use requirement of solar power plants in the United States. Golden, CO: National Renewable Energy Laboratory, **2013**.

[3.9] Union of Concerned Scientists; Science for a healthy planet and safer world, solar power plants: large-scale PV, <https://www.ucsusa.org/clean-energy/renewable-energy/solar-power-plants-large-scale-pv>, accessed 9/17/19.

[3.10] Mousazadeh, H., Keyhani, A., Javadi, A., Mobli, H., Abrinia, K. Sharifi, A. A review of principle and sun-tracking methods for maximizing solar systems output. *Renewable and Sustainable Energy Reviews*, **2009**, 13(8), 1800-1818.

[3.11] Kacira, M., Simsek, M., Babur, Y., Demirkol, S. Determining optimum tilt angles and orientations of photovoltaic panels in Sanliurfa, Turkey. *Renewable Energy*, **2004**, 29(8), 1264-1275.

[3.12] Maatallah, T., Alimi, S. E., Nassrallah, S. B. Performance modeling and investigation of fixed, single, and dual-axis tracking photovoltaic panel in Monastir city, Tunisia. *Renewable and Sustainable Energy Reviews*, **2011**, 15(8), 4053-4066.

[3.13] Abu-Khader, M., Badran, O. O., Abdallah, S. Evaluating multi-axes sun-tracking system at different modes of operation in Jordan. *Renewable and Sustainable Energy Reviews*, **2008**, 12(3), 864-873.

[3.14] Lubitz, W. D. Effect of manual tilt adjustments on incident irradiance on fixed and tracking solar panels. *Applied Energy*, **2011**, 88(5), 1710-1719.

[3.15] Yadav, A. K., Chandel, S.S. Tilt angle optimization to maximize incident solar radiation: A review. *Renewable and Sustainable Energy Reviews*, **2013**, 23, 503-513.

[3.16] Bakirci, K. General models for optimum tilt angles of solar panels: Turkey case study. *Renewable and Sustainable Energy*, **2012**, 16(8), 6149-6159.

[3.17] Ahmad, M. J, Tiwari, G. N. Optimization of Tilt Angle for Solar Collector to Receive Maximum Radiation. *The Open Renewable Energy Journal*, **2009**, 2, 19-24.

[3.18] Khatib, T., Mohamed, A., Sopian, K. On the monthly optimum tilt angle of solar panels for five sites in Malaysia. *2012 IEEE International Power Engineering and Optimization Conference Melaka, Malaysia,* **2012**, 7-10.

[3.19] Lave, M., Kleissl, J. Optimum fixed orientations and benefits of tracking for capturing solar radiation in the continental United States. *Renewable Energy*, **2011**, 36(3), 1145-1152.

[3.20] Siraki, A. G., Pillay, P. Study of optimum tilt angles for solar panels in different latitudes for urban applications. *Solar Energy*, **2012**, 86(6), 1920-1928.

[3.21] Despotovic, M., Nedic, V. Comparison of optimum tilt angles of solar collectors determined at yearly, seasonal, and monthly levels. *Energy Conversion and Management*, **2015**, 97, 121-131.

[3.22] Asl-Soleimani, E., Farhangi, S., Zabihi, M. S. The effect of tilt angle, air pollution on performance of photovoltaic systems in Tehran. *Renewable Energy*, **2001**, 23(3-4), 459-468.

[3.23] Elhab, B. R., Sopian, K., Mat, S., Lim, C., Sulmaiman, M. Y., Rusian, M. H., Saadatian, O. Optimizing tilt angles and orientation of solar panels for Kuala Lumpar, Malaysia. *Scientific Research and Essays*, **2012**, 7(43), 3758-3767.

[3.24] Kaddoura, T. O., Ramli, M. A. M., Al-Turki, Y.A. On the estimation of the optimum tilt angle on PV panel in Saudi Arabia. *Renewable and Sustainable Energy Reviews*, **2016**, 65, 626-634.

[3.25] Rowlands, I. H., Kemery, B. P., Beausoleil-Morrison I. Optimal solar-PV tilt angle and azimuth: An Ontario (Canada) case-study. *Energy Policy*, **2011**, 39(3), 1397-1409.

[3.26] Tang, R., Wu, T. Optimal tilt-angles for solar collectors used in China. *Applied Energy*, **2004**, 79(3), 239-248.

[3.27] Lewis, G. Optimum Tilt of Solar Collector. *Sol. Wind Energy* **1987**, 4, 407–410.

[3.28] Calabrò, E. An algorithm to determine the optimum tilt angle of a solar panel from global horizontal solar radiation. *J. Renew. Energy* **2013**, 1, doi:10.1155/2013/307547.

[3.29] Idowu, O.S.; Olarenwaju, O.M.; Ifedayo, O.I. Determination of optimum tilt angles for collectors in low-latitude tropical regions. *Int. J. Energy Environ. Eng.* **2013**, 4, doi:10.1186/2251-6832-4-29.

[3.30] Darhmaoui, H.; Lahjouji, D. Latitude based model for tilt angle optimization for collectors in the mediterranean region. *Energy Procedia* **2013**, 42, 426–435.

[3.31] Benghanem, M. Optimization of tilt angle for solar panel: Case study for Madinah, Saudi Arabia. *Applied Energy*, **2011**, 88(4), 1427-1433.

[3.32] NREL, National solar radiation database, 1991-2010 update. <http://rredc.nrel.gov/solar/old_data/nsrdb/1991-2010/>, [accessed 09.15.17].

[3.33] Kafka, J. L., Miller, M. A. A climatology of solar irradiance and its controls across the United States: implications for solar panel orientation. *Renewable Energy,* 2018, **135**, 897-907.

[3.34] Jakhrani, A. Q., Samo, S. R., Rigit, A. R. H., and Kamboh, S. A. Selection of models for calculation of incident radiation on tilted surface. *World Applied Science Joural*, **2013**, 22(9). 1334-1343.

[3.35] Passias, D. and Källbäck, B. Shading effects in rows of solar cell panels. *Solar Cells*, **1984**, 11, 281-291.

[3.36] Hay, J. E. Calculating solar radiation for inclined surfaces: Practical approaches. *Renewable Energy*, **1993**, 3(4/5), 373-380.

[3.37] Hottel, H. C. and Woertz, B.B. Evaluation of flat-plate solar heat collector. *Trans. ASME*, **1942**, 91.

[3.38] Liu, B. Y. H., and Jordan, R. C. The long-term average performance of flat-plate solar-energy collectors. *Solar Energy*, **1963**, 7(2), 53-74.

[3.39] Klucher, T. M. Evaluation of models to predict insolation on tilted surfaces. *Solar Energy*, **1979**, 23(2), 111-114.

[3.40] Hay, J. E. and Davies, J. A. Calculations of the solar radiation incident on an inclined surface. *Proc. Of First Canadian Solar Radiation Data Workshop, Ministry of Supply and Services,* **1980**.

[3.41] Reindl, D. T. Beckmann, W. A., and Duffie, J. A. Diffuse radiation correlations. *Solar Energy*, **1990**, 45(1), 1-7.

[3.42] Kassianov, E., Long, C. N., Ovtchinnikov, M. Cloud sky cover versus cloud fraction: whole-sky simulations and observations. *J. Applied Meteorology and Climatology,* **2004,** 44, 86-98.

[3.43] Pfister, G., McKenzie, R. L., Liley, J. B., Thomas, A., Forgan, B. W., Long, C. N. Cloud coverage based on all-sky imaging and its impact on surface solar irradiance. *J. Applied Meteorology and Climatology,* **2003**, 42, 1421-1434

[3.44] Muneer, T. Solar radiation and daylight models for the energy efficient design of buildings. *Architectural Press*, Oxford, **1997.**

[3.45] Kocifaj, M. Angular distribution of scattered radiation under broken cloud arrays: An approximation of successive orders of scattering. *Solar Energy*, 2012, **86**, 3575-3586.

[3.46] Kocifaj, M. Unified model of radiance patterns under arbitrary sky conditions. *Solar Energy*, **2015**, 115, 40-51.

[3.47] Kocifaj, M. and Kómar, L. Modeling diffuse irradiance under arbitrary and homogenous skies: Comparison and validation. *Applied Energy*, 2016, **166**, 117-127.

[3.48] International Finance Corporation World Band Group. A project developer's guide to utility-scale solar photovoltaic power plants, **2015.**

[3.49] Goswami, D. Y. Effect of row-to-row shading on the output of flat plate south facing solar arrays. *Jet Propulsion Laboratory,* **1986**.

Chapter 4

[4.1] Trancik, J. E. Renewable energy: Back the renewables boom. *Nature*, **2014**, 507, 300-302.

[4.2] Fu, R., Feldman, D., and Margolis, R. U.S. Solar Photovoltaic System Cost Benchmark: Q1 2018. Golden, CO: National Renewable Energy Laboratory.

[4.3] Kavlak, G., McNerney, J., Trancik, J. E. Evaluating the causes of cost reduction in photovoltaic modules. *Energy Policy,* **2018**, 123, 700-710.

[4.4] Solar Energy Industries Association, Solar Industry Research Data, <https://www.seia.org/solar-industry-research-data>, accessed 8/24/19.

[4.5] International Energy Association, Renewable capacity growth worldwide stalled in 2018 after two decades of strong expansion, <https://www.iea.org/newsroom/news/2019/may/renewable-capacity-growth-worldwide-stalled-in-2018-after-two-decades-of-strong-e.html>, accessed 7/1/2019.

[4.6] Coomes, O. T., MacDonald, G. K., and le Polain de Waroux, Y. Geospatial land price data: A public good for global change science and policy. *BioScience*, **2018**, 68(7), 481-484.

[4.7] Golden, J. S., Carlson. J, Kaloush, K. E., and Phelan, P. A comparative study of the thermal and radiative impacts of photovoltaic canopies on pavement surface temperatures. *Solar Energy*, **2007**, 81(7), 872-883.

[4.8] Mukhija, V. and Shoup, D. Quantity versus quality in off-street parking requirements. *J. of the American Planning Association*, **2006**, 72, 296-308.

[4.9] Davis, A. Y., Pijanowski, B. C., Robinson, K, and Engel, B. The environmental and economic costs of sprawling parking lots in the United States. *Land Use Policy*, **2010**, 27(2). 255-261.

[4.10] MFS Engineers & Surveyors, Rutgers University Solar Carport Canopy System, < https://mfsengineers.com/projects/rutgers-university-solar-carport>, accessed 9/23/19.

[4.11] Rutgers Board of Governors Approves 32-Acre Solar Canopy Project, Rutgers Today, April 5, 2011 <https://news.rutgers.edu/news-release/rutgers-board-governors-approves-32-acre-solar-canopy-project/20110405#.XY59AUZKg2w.

[4.12] Kornitas, M., "Energy Conservation, Renewable Energy, The Future of Rutgers", Rutgers Facilities, Strategic planning public web information 2014: <https://ipo.rutgers.edu/sites/default/files/Modified_copy_of_Strategic_planning_for_Energy_Conservation_2014.pdf>.

[4.13] NREL, National Solar Radiation Database, 1991-2005 Update: Typical Meteorological Year 3, <https://rredc.nrel.gov/solar/old_data/nsrdb/1991-2005/tmy3/>.

[4.14] Reda, I, and Andreas, A. Solar Position Algorithm for Solar Radiation Applications. **2008,** Golden, CO: National Renewable Energy Laboratory.

[4.15] NREL, PVWatts Calculator, <https://pvwatts.nrel.gov/>.

[4.16] Kassianov, E., Long, C. N., Ovtchinnikov, M. Cloud sky cover versus cloud fraction: whole-sky simulations and observations. *J. Applied Meteorology and Climatology,* **2004,** 44, 86-98.

[4.17] Pfister, G., McKenzie, R. L., Liley, J. B., Thomas, A., Forgan, B. W., Long, C. N. Cloud coverage based on all-sky imaging and its impact on surface solar irradiance. *J. Applied Meteorology and Climatology,* **2003**, 42, 1421-1434

[4.18] Dai, A. Global precipitation and thunderstorm frequencies, part II: Diurnal variations. *J. Climate*, **2001**, 14, 1112-1128.

[4.19] Wallace, J. M. Diurnal variations in precipitation and thunderstorm frequency over the conterminous United States. *Mon. Weather Rev.*, **1975**, 103, 406-419.

[4.20] Dai, A., Giorgi, F., and Trenberth, K. E. Observed and model-simulated diurnal cycles of precipitation over the contiguous United States. *J. Geophysical Research*, **1999**, 104, 6377-6402.

[4.21] Jelle, B. P. The challenge of removing snow downfall on photovoltaic solar cell roofs in order to maximize solar energy efficiency – Research oppurtunities for the futre. *Energy and Buildings*, **2013**, 67, 334-351.

[4.22] Ross, M. M. D., and Usher, E. P. Photovoltaic array icing and snow accumulation: a study of a passive melting technology. *Proceedings of the 21st Annual Conference of the Solar Energy Society of Canada, Toronto, Ontario, Canada, 31 October-2 November*, **1995**, 21-26.

[4.23] Klein, S. A., and Hartmann, D. L. The seasonal cycle of low stratiform clouds. *J. Climate*, **1993**, 6, 1587-1606.

[4.24] Lau, N.-C., and Crane, M. W. Comparing satellite and surface observations of cloud patterns in synoptic-scale circulation systems. *Mon. Weather Rev.*, **1997**, 125, 3172-3189.

[4.25] Naud, C. M., Del Genio, A. D., Bauer, M., and Kovari, W. Cloud vertical distribution across warm and cold fronts in CloudSat-CALIPSO data and a general circulation model. *J. Climate*, **2010**, 23, 3397-3415.

[4.26] Yingli Solar Module Specifications <http://www.yinglisolar.com>

Chapter 5

[5.1] Klucher, T. M. Evaluation of models to predict insolation on tilted surfaces. *Solar Energy*, **1979**, 23(2), 111-114.

[5.2] Kocifaj, M. Angular distribution of scattered radiation under broken cloud arrays: An approximation of successive orders of scattering. *Solar Energy*, 2012, **86**, 3575-3586.

[5.3] Kocifaj, M. Unified model of radiance patterns under arbitrary sky conditions. *Solar Energy*, **2015**, 115, 40-51.

[5.4] NREL, National solar radiation database, 1991-2010 update. <http://rredc.nrel.gov/solar/old_data/nsrdb/1991-2010/>, [accessed 09.15.17].